2003

Electrochemistry and spectroscopy of energy conversion and polynuclear aromatic materials.

Maryam. Nazri
University of Windsor

NOTE TO USERS

ELECTROCHEMISTRY AND SPECTROSCOPY OF ENERGY CONVERSION AND POLYNUCLEAR AROMATIC MATERIALS

BY
MARYAM NAZRI

A Dissertation
Submitted to the Faculty of Graduate Studies and Research through the
Department of Chemistry and Biochemistry
in Partial Fulfillment of the Requirements for the
Degree of Doctor of Philosophy at
The University of Windsor

Windsor, Ontario, Canada
2003

Your file Votre référence
ISBN: 0-612-84596-6
Our file Notre référence
ISBN: 0-612-84596-6

ABSTRACT

The field of materials chemistry is becoming increasingly important in many technological disciplines, including batteries, fuel cells, hydrogen storage materials, and application of poly-nuclear aromatic compounds in solar cells, color copiers, sensors, and catalysis. This multidisciplinary research work focuses on the development, understanding, and characterization of novel materials for advanced lithium batteries and a unique series of polyaromatic compounds for application in solar cells and color copiers.

A general overview of materials and techniques used in this work is presented, including the electrochemistry, spectroscopy, thermal analysis, and x-ray diffraction. A unique electrochemical procedure based on carbon paste microelectrode was applied to study the electrochemistry of novel poly-nuclear aromatic compounds. X-ray diffraction and vibrational spectroscopy are also used to gain further information about their molecular organization in solid-state.

Conductivity of a novel electrolyte based on a multi-blend of organic carbonate solvents, has been studied over a wide range of temperatures (-40 to 70 °C). An optimized electrolyte for an advanced lithium battery based on ternary solvent blend of linear and cyclic organic carbonates has been developed.

The nature of ion-association and ion-solvent interactions in complex electrolytes are studied using infrared spectroscopy. We have found a strong preferred solvation of lithium ion in electrolyte containing multi-blend solvent molecules.

The advanced lithium battery uses intercalation compounds with layered structure such as $LiCoO_2$ cathode, and lithiated graphite, (LiC_6), anode. In this work, we have studied the reactivity of Li-C anode materials in contact with organic carbonate-based electrolyte, and have investigated the nature of the decomposition products formed on the electrode surface. A significant reactivity between the LiC_6 and organic electrolytes is observed, and is a major safety concern. A unique, yet simple procedure was developed for spectroscopy and X-ray diffraction of air sensitive materials.

The electrochemical properties of poly-aromatic molecules are studied using a novel carbon-paste micro-electrode technique. The electrochemical studies indicate that the charge transport in this class of compounds is diffusion controlled, and the radical anions that are formed during reduction of polyaromatics are stable enough to be observed during the oxidation to the neutral state.

IR spectra of polyaromatic molecules, in the far- and mid-IR have been obtained. Thermal analysis has shown that the PTCDA, and its derivatives used in this work, are thermally stable up to 400 °C, and they are suitable for application in solar cells and color copiers.

This work is dedicated to my family for their continuous and unconditional support.

ACKNOWLEDGEMENT

I would like to thank Professor Ricardo Aroca, supervisor, for his dedication, continuous advice, and his patience through the course of this research work. I also thank the electrochemistry group for much technical help and valuable discussions. I am deeply grateful to many members of the Physics and Physical Chemistry Department at General Motors Research and Development Center for their valuable discussion, and many helpful comments on selected portions of this work.

TABLE OF CONTENTS

LIST OF TABLES

LIST OF FIGURES

LIST OF ABBREVIATIONS

AN: Acceptor number (acceptivity), degree of electron pair acceptivity

ATR: Attenuated total reflection

BAS: Bioanalytical systems

CE: Counter electrode (Auxiliary electrode)

CPE: Carbon past electrode

CuPc: Copper phthalocyanine

CV: Cyclic voltammetry

DEC: Diethyl carbonate

DMC: Dimethyl carbonate

DME: Dimethoxyethane

DN = Donor number (donicity), degree of electron pair donicity

DSC: Differential scanning calorimetry

DTGS: Far-IR detector

E: Potential

EC: Ethylene carbonate

E_F: Energy Fermi level

EMC: Ethyl methyl carbonate

EPA: Electron pair acceptor

EPD: Electron pair donor

EPDM: Ethylene propylene diene monomer

FT-IR: Fourier transform infrared

GC: Gas Chromatograph

H_2Pc: Phthalocyanine

HOMO: Highest occupied molecular orbital

Hz: Hertz (unit of frequency)

KBr: Potassium bromide

Li_2Pc: Dilithum phthalocyanine

LUMO: Lowest unoccupied molecular orbital

mAh: Milliampere hour (energy)

MCT: Mercury cadmium telluride

MS: Mass spectrometer

mPaS: Meter Pascal second

NTCDA: Nathtalenetetracarboxylicanhydride

PC: Propylene carbonate

PDT: Photodynamic therapy

PTCDA: Perylenetetracrboxilicdianhydride

RE: Reference electrode

RLC: Digibridge (Resistance, inductance, capacitance measurement unit)

SCE: Saturated calomel electrode

SEI: Solid electrolyte interface

SR2: Bis-(3-fluorobenzylimido)perylene

SR4: Bis-(2,6 difluorobenzylimido) perylene

SR6: Bis-(3,4 dichlorobenzylimido) perylene

SR7: Bis-(3,5 dichlorobenzylimido)perylene

TGA: Thermogravimetry analysis

Thio-PTCD: Thio(n-Propylimido)perylene

V: Voltage

WE: Working electrode

XRD: X-ray diffraction

PART I

Electrochemical, Spectroscopy, and Reactivity of Non-aqueous Electrolyte for Advanced Lithium Batteries

Chapter 1

INTRODUCTION

A General Overview of the Materials

I.1.1. General Overview of Materials

I.1.1.1. Electrolytes

There are many processes and devices that require electrolytes with high ionic conductivity and high electrochemical stability. Examples include electrochemical power sources (i. e. batteries, capacitors, fuel cells), electrochromic display devices, sensors, electrochemical synthesis, and processes for elimination of toxic wastes by the electrochemical oxidation / reduction of toxic substances. Understanding of electrolyte properties is equally important in the medical field, particularly for ion transport across the excitable biomembrane channels. Nonaqueous electrolytes also have technological importance in synthesis of useful organic molecules through electrochemical methods.

The ion-solvent interaction induces molecular polarization that alters the bond-covalency and shifts the redox potential: this is known as the solvent effect. The polarization due to ion-solvent interaction shifts the electron density of solvent molecules, (a donor), toward the solute, (an acceptor). The ion solvent interactions significantly affect the mobility of the ions in electrolyte media. This effect is particularly important in polymeric electrolytes, where the ions bring the polymeric chains together and serve as a cross-linking agents [1].

The ionic mobility in liquid electrolytes correlates well with the conductivity according to the general conductivity expression [2],

$$\sigma = \Sigma\, n_i q_i \mu_i \qquad (I.1.1)$$

where σ is the conductivity, n_i is the number of mobile ions, q_i is the charge of mobile ion, and μ_i is the mobility of the species. The number of mobile ions is related to the amount of salt dissolved in the electrolytes. In a very dilute electrolyte case, most of the ions remain as free ions. However, in concentrated and practical electrolytes, besides the free ions, other species such as ion-pairs, ion multiples, and ion aggregates may exist. The mobility of the ions is significantly related to the size and charge of the ions as well as the polarizability of the ion and the dielectric constant of electrolyte media. The size and charge of the ions also determines the coordination geometry and coordination number of the ions. Solvent polarizability is an important factor in the conductivity of the electrolytes. Solvent molecules with polar groups such as hydroxyl, ether, ester, and carbonate groups may dissolve significant amount of salts.

In general, two major classes of electrolytes are well recognized, the liquid electrolytes and the solid electrolytes. The liquid electrolytes include both aqueous and nonaqueous liquid systems. The solid electrolyte includes the ceramic electrolytes, the polymeric, and the gel electrolytes. However, the gel electrolyte is a hybrid system with trapped liquid solvent in a polymeric host, and in most cases, the ionic conduction mainly occurs through the liquid phase.

One of the important requirements of a good electrolyte for electrochemical applications is the stability of the system over a wide voltage range (0-5 V). Electrochemical stability of the nonaqueous electrolytes is an important factor in the

selection of electrolytes for batteries. Electrolytes must be stable in contact with the reducing anode and the oxidizing cathode materials. Electrolytes also must be stable during charge and discharge cycles of the battery, where the cell potential exceeds the inter-electrode potential. An unstable electrolyte decomposes during charge or discharge and usually produces gaseous species, which may complicate the performance of the device. In large size batteries, the gaseous species generated during electrolyte decomposition may cause an explosion and leakage of the liquid electrolyte. Therefore, the stability of the electrolyte needs to be examined before application in electrochemical devices. In this work, the electrochemical stability of various organic carbonate based electrolytes have been examined in a wide voltage range, (0 - 5 volt versus Li).

The Lithium-ion rechargeable batteries have attracted a great deal of worldwide attention, particularly for application in computers, communication, and portable electronic devices. Lithium-ion batteries are relatively safer than the old lithium batteries with a metallic lithium anode, and have a higher charge-discharge cycle life. The lithium-ion cells provide a high voltage, (3.7 V), that is almost 3-times the voltage of nickel-cadmium and nickel-metal hydride (1.2 V) cells. A recent breakthrough in the field of electrochemical devices has been the development of the so called "rocking chair" or "lithium-ion" battery. The reason for these names are the shuttle mechanism of lithium ions between anode and cathode during charge – discharge cycles. The lithium is intercalated between the layer structures of the anode (i.e.graphitic) materials during charging. During discharge, the lithium is removed from the graphite galleries and transported across the electrolyte and resides in the crystal structure of the cathode

materials (transition metal oxides). The anode is commonly made up of carbonaceous or graphitic materials, which are well known for their facile lithium intercalation-deintercalation properties. In an ideal anode, one lithium atom is inserted for every six carbon atoms to form, LiC_6.

Candidates for the makeup of the cathode are usually the 2-D transition metal oxides or chalcogenides including, $LiMO_2$ (M=Co, Ni, Mn) with a layered structure (*R3m* Space Group), or the 3-D spinel type compounds such as $LiMn_2O_4$ (*Fd3m* Space Group), which show good lithium insertion-deinsertion properties. These oxide cathodes have relatively high discharge potential (3-4.5 V vs. Li), which make them attractive electrode materials for high voltage batteries. In most high voltage cathodes, the oxidation states of the transition metal changes between M^{III} to M^{IV} states. The average cell voltage for common lithium-ion cells, ($C//LiCoO_2$), is about 3.7 volts. In recent years, oxide anodes also have been proposed, particularly the $LiTi_5O_8$ phase. This oxide has a redox potential of about 1.5 V vs lithium. Therefore, the $LiTi_5O_8//Li_{1-x}CoO_2$ ($x>0.5$) has an average cell voltage of 2.5 V. The advantages of oxide anodes vs graphitic anodes are increased safety and better charge-discharge cycle life. There is almost no volume change when lithium is inserted or extracted from the $LiTi_5O_8$.

Electrolytes used in current advanced lithium-ion batteries are composed of a lithium salt ($LiPF_6$, $LiBF_4$, $LiCF_3SO_3$, $LiClO_4$, etc) dissolved in a multi-blend of organic solvents such as mixture of cyclic and linear organic carbonates. The cyclic carbonates such as ethylene carbonate, and propylene carbonate have high dielectric constants and

dissolve significant amounts of salt. The linear organic carbonates such as dimethyl carbonate, diethyl carbonate, and asymmetric linear carbonates such as methyl ethyl carbonates have a low dielectric constant, and a very low viscosity as compared with the cyclic carbonate. The linear carbonates are added to reduce the viscosity, and improve the low temperature conductivity of the mixed electrolytes. A list of organic carbonates commonly used in lithium batteries is shown in Table I.1.1. Although progress has been made in enhancing the conductivity of solid electrolytes such as polymeric and ceramic electrolytes, the liquid electrolytes are still used in most electrochemical systems. The basic requirements of a suitable electrolyte for electrochemical devices include high ionic conductivity, low melting point, high boiling point, as well as chemical and electrochemical stabilities [2].

Table I.1.1: Pure solvents and solvent blends and lithium salts used in lithium batteries

Solvents			
EC	DEC	DMC	PC
EC	DEC	DMC	PC
EC-DEC	DEC-PC	DMC-DEC	PC-DEC
EC-DMC	DEC-DMC	DMC-EC	PC-DMC
EC-PC	DEC-PC	DMC-PC	PC-EC
EC-DMC-PC	DEC-EC-PC	DMC-DEC-EC	PC-DMC-DEC
Lithium Salts			
$LiPF_6$,	$LiBF_4$,	$LiSO_3CF_3$	$LiN(SO_2CF_3)_2$,
$LiAsF_6$,	$LiClO_4$	$Li[B(OCORX)_4]$	$Li_2N(SO_2CF_3$

Cyclic carbonates: Ethylene Carbonate (EC), Propylene Carbonate (PC).
Linear carbonates: Dimethyl Carbonate (DMC), Diethylene Carbonate (DEC),
Asymmetric linear carbonates such as methyl-ethyl carbonate (MEC) also have been used

Although the use of graphitic anodes has revolutionized the field of batteries, the lithiated graphitic anodes react with most organic electrolytes and cause an irreversible capacity loss during initial charging. The reaction by-product that forms on the surface of electrode is called the solid electrolyte interface (SEI) layer. The SEI-layer increases the resistance of the cell, particularly at the anode/electrolyte interface region. Reducing the irreversible capacity loss of anode materials is an active field of research. The mechanism of electrolyte decomposition on the surface of lithiated graphite, LiC_6, and formation of gaseous species, and an SEI layer, are not well understood. In this work, the chemical composition of the SEI layer and formation of gaseous species due to electrolyte decomposition have been studied.

There is also residual oxidation of electrolyte on the surface of cathode materials, particularly during over-charge of the lithium-ion cells. This is usually the case when the voltage of the cell exceeds the stability voltage of the carbonate-based electrolytes (>4.5 volts) during over-charge [3]. The onset of electrolyte oxidation often defines the cutoff voltage on charge prior to accessing the full capacity of the cathode. In this regard, transition metal oxide cathodes of the form $LiMO_2$ (M=Co, Ni and Mn) may be delithiated to the point where cell potentials readily exceed 4 V vs. Li^+ /Li [4].

I.1.2. Poly-nuclear Aromatic Materials

Poly-nuclear aromatic molecules such as perylene derivatives are particularly attractive for their unique thermal stability, optical, and electrical properties. These molecules tend to form highly ordered structures and supramolecular assemblies. X-ray

diffraction analysis of perylene derivatives reveals a highly ordered structure of polyaromatic rings [5].

The polyaromatic molecular assemblies have unique selectivity for light absorption and they are suitable sensitizers for photodynamic therapy of cancer cells. The Al and Zn derivatives of phthalocyanines are routinely used for their photodynamic therapy behavior due to their low toxicity. These molecules absorb light at wavelength longer the 600 nm and do not interfere with absorption of light by blood. In addition, they adsorb selectively on the surface of tumor cells [6].

Tuning a materials optical absorption to the selective radiation wavelengths is a frontier research in developing materials for cancer therapy, harvesting solar energy by solar cells, and sharp color copiers. The polyaromatic compounds are used for optical limiting applications, because of their excited-state absorption properties. In order to increase the application of polyaromatic derivatives in clinical and optical fields, they are made soluble by appropriate peripheral substitutions [7].

Many fundamental studies on the crystal structure [8-10] and electronic structure [11,12] of polyaromatic compounds have bean reported. Polyaromatic molecules such as, perylene derivatives tends to form highly ordered thin films with interesting optical characteristics. They are potentially interesting for optical technology because of their high thermal stability and semiconductor properties [13]. In this work, the

electrochemical properties of various polyaromatic compounds have been studied. Their structure in solid state has been studied by IR spectroscopy and X-ray diffraction.

Chapter 2

EXPERIMENTAL TECHNIQUES

I.2.1. Electrochemical Techniques

I.2.1.1. Cyclic Voltammetry

The three electrodes system used for electrochemical studies consisted of a carbon paste microelectrode as the working electrode, platinum wire as the auxiliary electrode, and the saturated calomel electrode as the reference electrode. A pear shape electrochemical cell with a 50 ml electrolyte volume capacity was used, as shown in Figure I.2.1. The BAS 100B/W electrochemical workstation, which is a microprocessor-based electrochemical analyzer, was used for data collection. The headstart software from PARR Instrument was used for cyclic voltammetry measurements.

I.2.1.2. Electrode Preparation

The cell configuration with three electrodes is shown in Figure I.2.1. The working electrode is a microelectrode, (from Bioanalytical Systems). The working electrode was polished with 0.1μ alumina powder and washed with distilled water and dried under 10^{-3} torr vacuum. Samples, PTCDA, Thio-PTCD, and their derivatives (ca. 80w%) were mixed with conductive carbon black (15w%), and 5w% EPDM (ethylene propylene diene monomer) binder that was dissolved in xylene solvent (3 w% EPDM in xylene). The mixture was then ground to form an ink type slurry. A small drop of this ink slurry was placed on the tip of the microelectrode and dried (under vacuum, 10^{-3} torr) for four hours and used as the working electrode. The electrolyte was a 1M $LiClO_4$ in acetonitrile solution for the electrochemical studies of polyaromatic compounds.

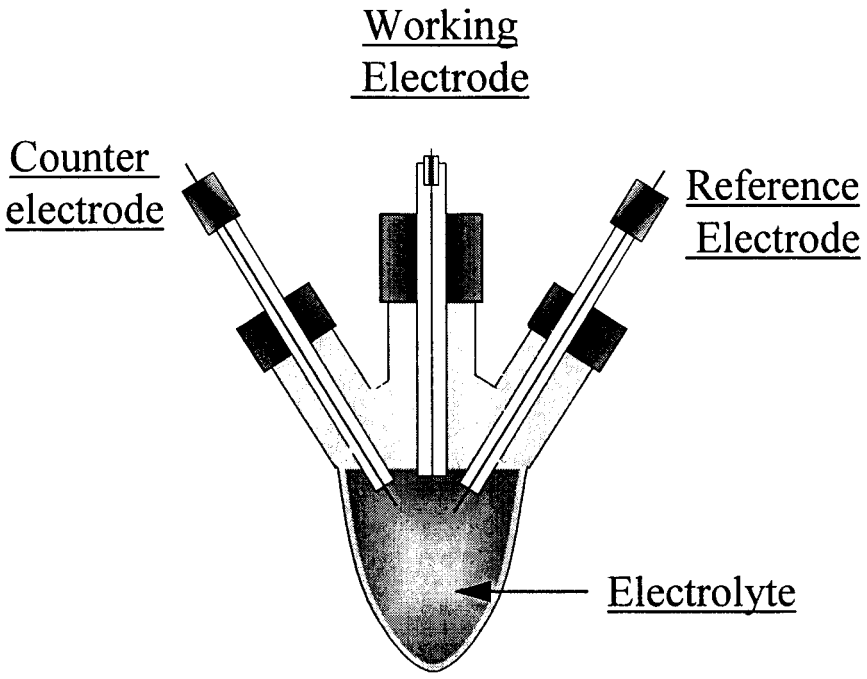

Figure I.2.1: Schematic of the three electrode electrochemical cell.

The cyclic voltammetry of the samples were performed between -2000 and 2000 mV vs. SCE. The potential scan rates were chosen to increase from 2 mV/sec up to 200 mV/sec. Cyclic voltammetry of ferrocene was used to calibrate the electrochemical redox potential. The cyclic voltammogram of ferrocene in acetonitrile + 1M $LiClO_4$ at 100 mV/sec scan rate is shown is Figure I.2.2. Despite the capacitive effect of the carbon paste electrode, the ratio of oxidation and reduction peaks are close to unity, $I_{Pa}/I_{Pc}=1$, indicating a reversible oxidation-reduction process.

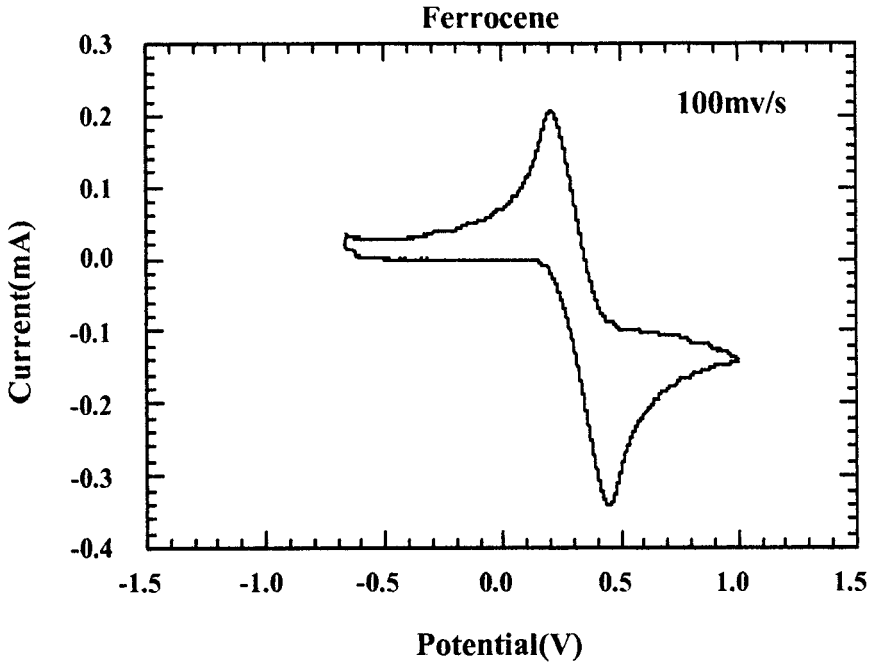

Figure I.2.2: Cyclic voltammetry of ferrocene in Acetonitrile + 1M $LiClO_4$.

I.2.1.3 Conductivity Measurements

Conductivity measurements were performed using dip cells (model A-01 with cell constant 0.1 from Rosemount Analytical Inc). These cells use two platinized parallel plates fixed in a cylindrical glass cavity. The electrode is dipped in the electrolyte and remains there for at least 5 minutes before the measurements are started. The reproducibility of the results after a 5 minutes hold time was almost 100%. The cell was connected to a Genrad model GR1689 / 1689M precision RLC Digibridge.

The Genrad Digibridge is a microprocessor-controlled programmable RLC measuring instrument with long-term stability and better than 0.02% accuracy. This

instrument can measure resistance, capacitance, and inductance as a function of frequency from 1mHz up to 100 KHz. The Digibrige can be used in manual mode or can be programmed with a PC computer. In this case it was interfaced with a PC computer. Conductometers are usually operated at 1000Hz, and the Digibridge operates at this frequecy if another frequency is not specified. Figure I.2.4 shows the schematic of a conductivity measurement set-up. The temperature of the conductivity cell was controlled using a circulating bath. The cell temperature was controlled within a 0.1 degree centigrade accuracy. For each measurement the conductivity cell was equilibrated for 10 minutes. During conductivity and viscosity measurements, it is important to maintain the temperature of the electrolyte constant. We have used a constant temperature-circulating bath with an accuracy of $\pm 0.1^{\circ}C$. The conductivity was measured from –30 to 70 °C. This temperature range is a good range for testing the conductivity of practical electrolytes for battery application.

The conductivity (σ) of a liquid electrolyte can be approximated by [1],

$$\sigma=(\nu/6)(N/V)e^2/K_BT=(N/V)e^2D/K_BT \qquad (I.2.1)$$

where N is the number of mobile ions of charge e contained in volume V, ν is the jump frequency, and D is the diffusion coefficient of the mobile ion [1]. The Stokes-Einstein relation can be used to relate D to viscosity η[1]:

$$D=K_BT/6\pi\eta r_j \qquad (I.2.2)$$

Where r_j is the Stokes radius of molecule j. From relations 1 and 2 it can be shown that the conductivity of the solution is inversely proportional to the viscosity of the solution. This inverse relationship is known as the Walden rule. The equivalent conductivity (λ) of a solution is described by [1],

$$\lambda=1000\sigma/c \qquad \text{(I.2.3)}$$

where σ is the conductivity ($\Omega^{-1}cm^{-1}$) and c is the equivalent concentration ($equiv/dm^{-3}$).

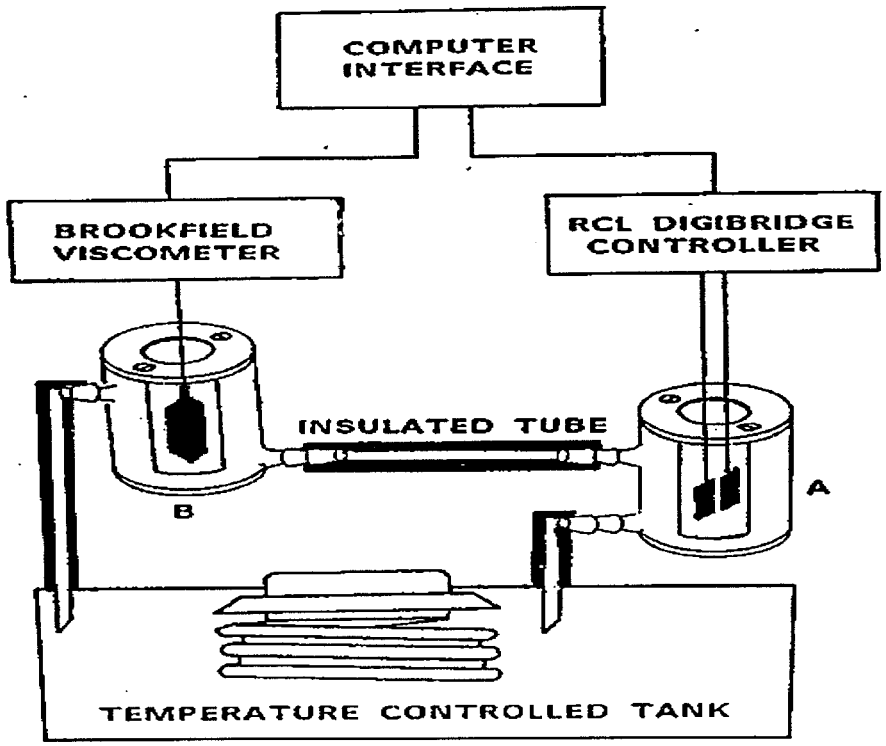

Figure I.2.3: Schematic of conductivity – viscosity-measuring system. Temperature of conductometer (A) and viscometer (B) was controlled by the circulating bath to ±1°.

I.2.1.4. Viscosity Measurements

The viscosity of electrolytes were measured using a Brookfiled viscometer Model M / 85-150E. The Brookfield viscometer is accurate to 1% of their stated values. The measured value on a Brookfield viscometer is translated to centipoises according to:

(Dial reading) x (speed factor) = viscosity in centipoises (mPa.S).

The instrument measures the viscosity of fluids at given shear rates (viscosity is a measure of a fluid's resistance to flow). This instrument measures the torque required to rotate an immersed element (the spindle) in a fluid. The viscosity is proportional to the spindle speed of rotation and is related to the spindle size and geometry.

The drag will increase with spindle size and rotation speed. Accurate temperature measurement during viscosity determination is very important. Because we were using the viscosity data as a complementary source for our conductivity measurements, it was essential to measure both the conductivity and the viscosity of the electrolyte at exactly the same temperature. Therefore a double pass-circulating bath was constructed in which the coolant fluid at a constant temperature circulates around both the conductivity cell and the viscometer chamber.

The tubing between the viscometer and the conductivity cell were kept to a minimum length. The circulating bath was a 50/50 by volume mixture of distilled water and commercial automobile antifreeze. The antifreeze-circulating bath was used to measure sub-ambient temperature conductivity and viscosity of solutions. Ethylene glycol diacetate was also used as coolant. The ethylene glycol diacetate (99%) from

Aldrich freezes at –41°c and boils at 186°c. The main component of automobile antifreeze is also a glycol derivative with low melting point. A rotating cylindrical spindle was used for viscosity measurements.

I.2.2. Infrared Spectroscopy

I.2.2.1. Transmittance and Attenuated Total Internal Reflection Measurements

Infrared spectroscopy is a powerful technique for investigation of solute-solvent interactions. The analysis of infrared spectra provides information about the energy of the ion-solvent interaction, ion association, complex formation, solvation number, and selective solvation when mixed solvents are used [14-19]. Most spectroscopic investigations in the past have been conducted on aqueous system in order to understand the nature of solvated cations and measure the solvation number (number of solvent molecules in the first shell surrounding the ion).

The advantages of Fourier transform spectroscopy for materials characterization are well known [20]. The optical path of the Fourier transform infrared spectrometer (Bruker model 113) used in this work is shown in Figure I.2.4. Basically, the acquired spectrum is an interferogram, and the Fourier transform operation converts the interferogram into a frequency domain IR spectrum. The Bruker IR spectrometer operates with three main software programs: 1) a multitask ATS program that supervises the ADAKOS and controls the functions of the optic bench, data collection, data manipulation, and plotting formats, 2) ADAKET, that controls access to the diskette and 3) ADAKOS, which controls the disk and supervises the other disk based programs. IR

radiation of a globar source is focused onto a KBr beam splitter for mid-IR spectroscopy. The spectrometer is equipped with a liquid nitrogen cooled MCT (Mercury Cadmium Telluride) broadband detector with an excellent response in the 400-4000 cm^{-1} range and with DTGS detector in the far-IR. The stability of the system for the entire range of this study was better than 99%. A typical 100% line spectrum (the ratio of two subsequent runs) is shown in Figure I.2.5 .

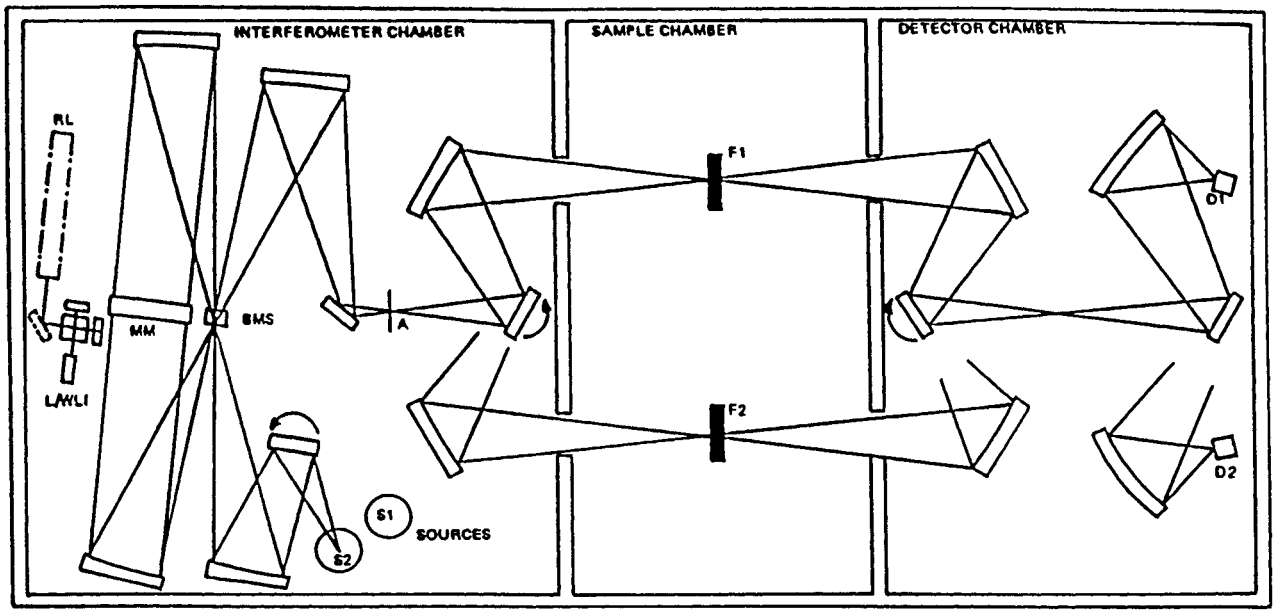

Figure I.2.4: Schematic of Fourier transform IR spectrometer optic bench [21].

ATR cells are shown in sample and reference channels.

S2 Globar Source
S1 Mercury is lamp
A Aperture
F1 Sample Focus
F2 Reference fours
BMS Beamsplitter
MM Moving Scan mirror
L/WLI Laser/white light interferometer
D1 Mid.-IR Detector
D2 Far-IR Detector

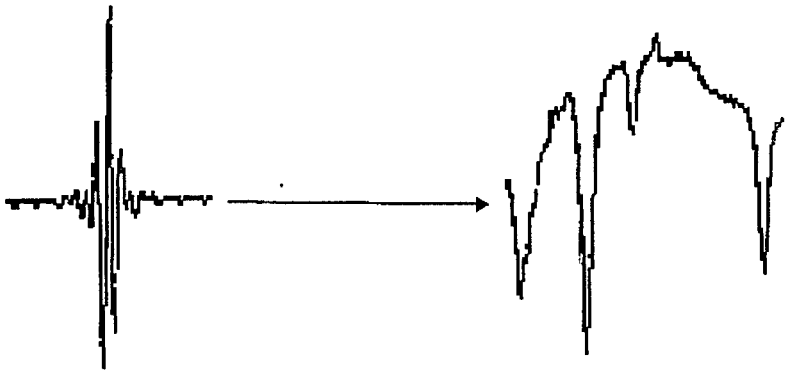

Fugure I.2.5: A typical Fourier transform conversion of an IR interferogram to a transmittance spectrum [21].

The ATR (attenuated total reflection) spectra were recorded using a liquid cylindrical cell from Spectratech, Inc.. The cell contains an IR transparent ZnSe ATR rod, 83 mm long and 6.35 mm in diameter ZnSe. Both ends of the rod are cut in 45° cone shapes. The cone shape ends provide a perpendicular entry for the incident beam, 45° for the internal reflection, and again a perpendicular beam exit from the rod. A special mirror assembly focuses the incident beam onto the entrance of the ATR rod. Another, similar mirror assembly collects the beam after exiting the rod and focuses the exiting beam toward the IR detector as shown in Figure I.1.6. The ATR rod is located in the center of a cylindrical cavity that contains the electrolyte. The ATR rod in this case is made of ZnSe, which provides over 25% transparency for the IR beam.

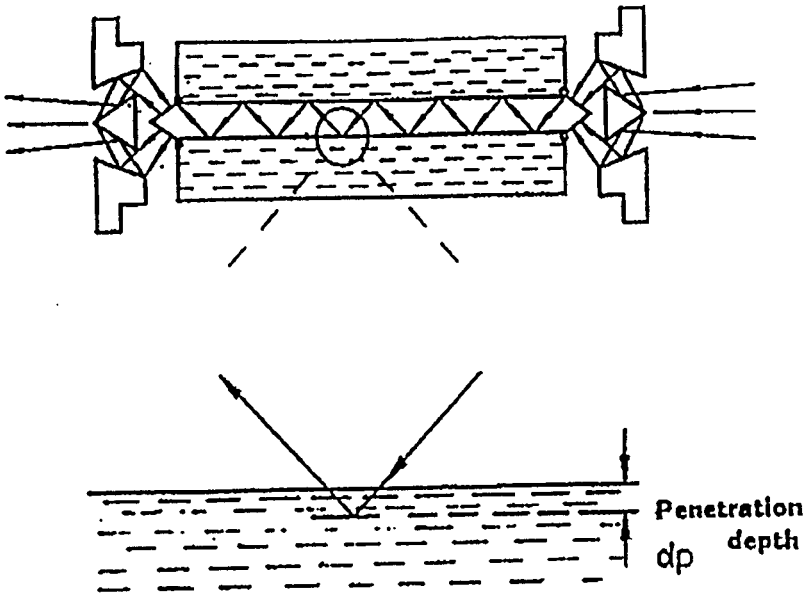

Figure I.2.6: Schematic of cylindrical ATR cell. ATR element is a ZnSe rod. Two special mirrors are used to focus the IR beam on the rod and collect the exit beam and direct it to the IR detector [22].

The principle of ATR spectroscopy at the interface of an IR transparent element and the solution sample is shown in Figure I.2.7. The incident and reflected beam construct an evanescent wave at the interface of the ATR element and the electrolyte. The evanescent part of the beam penetrates into the electrolyte zone in a small fraction of a wavelength, and allows to study the vibrational spectra of the electrolyte near the surface of the ATR element. The cylindrical cell used in this work provides very accurate and reproducible spectra for liquid samples.

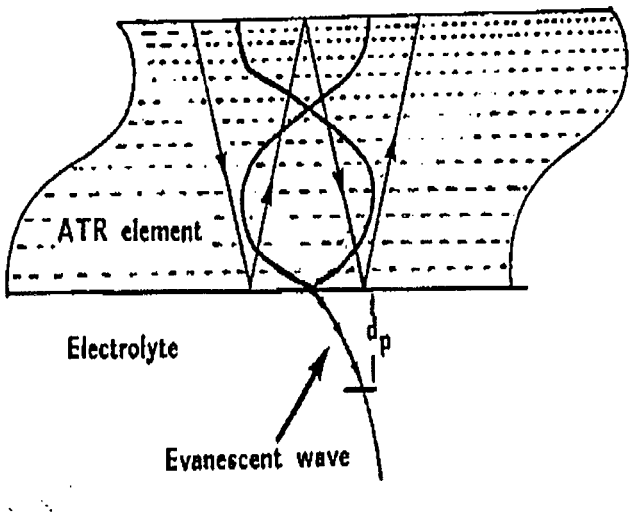

Figure I.2.7: Principle of ATR spectroscopy. The incident and reflected beam at the interface form a standing wave, the evanescent part of the wave penetrate into the electrolyte zone by a fraction of wavelength d_p [23].

Attenuated total reflection (ATR) infrared spectroscopy has been also used for the characterization of material surfaces. The sampling depth probed by the beam is very important for characterization of surface films [24]. Inshino and Ishida [25] have used Ge ATR plates with thin metal over layers for investigation of organic films.

I.2.3. Electrolyte Preparation

Propylene carbonate (PC), ethylene carbonate (EC), diethyl carbonate (DEC) and dimethyl carbonate (DMC) of high purity from Fluka, were used as solvents. $LiPF_6$ used in this study as lithium salt was from Hashimoto, Japan. The electrolyte preparation was performed inside of a Vacuum Atmosphere dry box (model M0-40-2H / DRI), equipped with a Nitrain nitrogen removal unit, and catalyst recirculation units. The dry box was

filled with 99.999% Argon. The atmosphere of the box was continuously circulated over Cu shaving catalyst and over titanium sponge at 700°C, to remove residual oxygen, moisture, and nitrogen, respectively. The Vacuum Atmosphere dry box model MO-40-2H / DRI, with a Nitrian (nitrogen remover) and catalyst recirculating units (oxygen and moister remover) is shown in Figure I.2.8. Oxygen and moisture sensors were also used to continuously monitor the purity of the box atmosphere. A 40 W tungsten light bulb was cracked and installed in the box to double check the purity of the box atmosphere. Usually, each lamp last over two-three weeks before burning out. The open filament of the lamp is very sensitive to reactive gases, and if there is a leak in the box the lamp will burns out in less than 1 minute. For each entry to the dry box, the antechamber was purged with argon gas at least three times before opening to the main box.

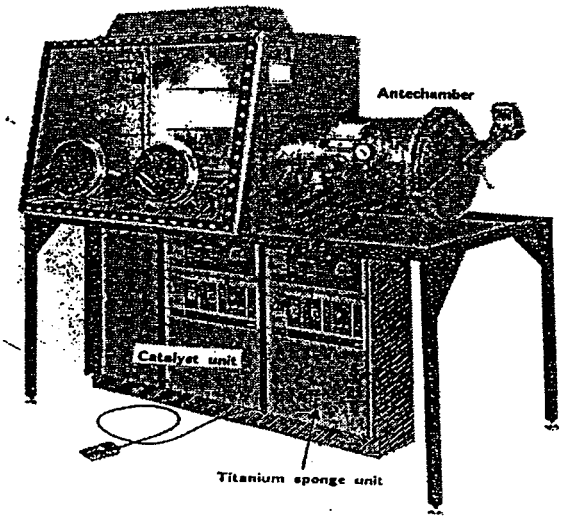

Figure I.2.8: All electrolytes were made in a dry box filled with 99.999% Argon. The atmosphere of the box was continuously circulated over Cu shaving catalyst and over titanium sponge at 700 °C to remove residual oxygen, moisture, and nitrogen [26].

I.2.4. Thermal Analysis

Thermal analysis of various polyaromatics compounds was studied by the Differential Scanning Calorimetry (DSC-7) and Thermogravimetry (TGA-7). The DSC and TGA were performed using the Model-7 PERKIN ELMER Thermal Analysis System. Aluminum, and stainless steel DSC pans were used in this work. Both DSC and TGA measurements were carried out under argon flow, and at a heating rate of 5°C/min from 30 to 400 °C. The analysis time was approximately 78min, including 2 minutes of isothermal recording at the initial and final stages. Between analyses, 2 hours were allowed for the surrounding enclosure to return to its original temperature distribution. For air sensitive samples, special stainless steel DSC pans with sealed screw top (from Perkin Elmer) were used.

I.2.5. Powder X-ray Diffraction

A Siemens 5000X-ray goniometer equipped with a Rigaku 18kw Rotating Cu anode source was used in this work. This unit allows in-situ X-ray diffractometry of the electrode materials (Fig. I.2.10). The diffraction data were collected at 0.02 degree scan usually between 10 to 90° 2(θ), at 40 kV and 30 mA. X-ray diffraction measurements were made on a pellet of material. The material was ground and pelletized at 5 tons/cm^2. Special care was made to prevent preferential ordering during the pelletizing of the sample. The top surface of the pellet was sieved to randomize the particle orientation.

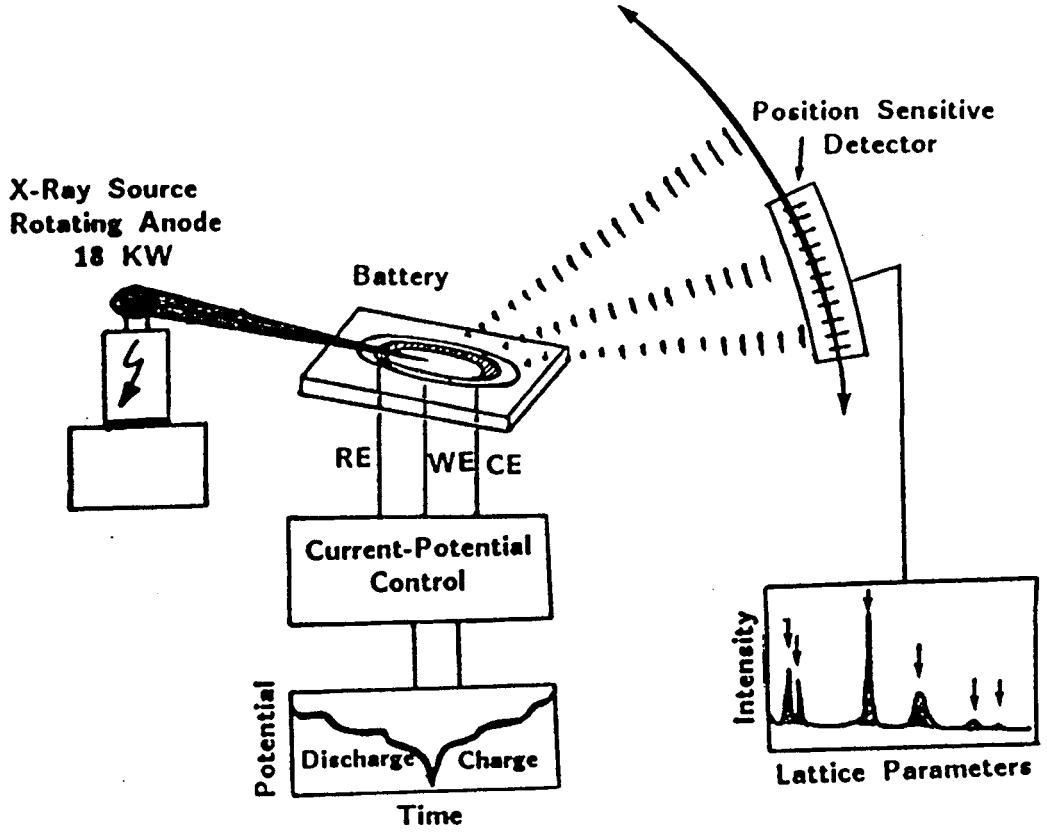

Figure I.2.9: Schematic of x-ray diffractometer

For air sensitive samples, a special sample holder shown in Figure I.2.10 is used. The sample pellet was fixed in the center of the sample holder by vacuum grease and pressed to exact X-ray focal plane distance. A wide X-ray transparent tape covering the curvature above the sample protected the sample from exposure to air. The sample was mounted inside of the dry box and sealed. The holder containing sample was inserted in the X-ray machine and its diffraction was collected.

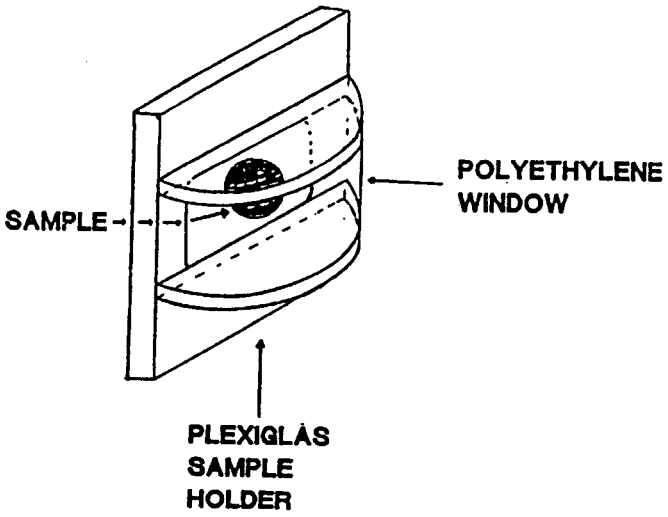

Figure I.2.10: Sample holder for air-sensitive samples, The sample in the form of powder or pressed pellet can be mounted at the focal point of the X-ray beam. The sample is protected by a wide-band scotch tape that covers the dome above the sample.

Chapter 3

ADVANCED ELECTROLYTES FOR LITHIUM BATTERIES

Ion-solvent Interactions and Conductivity Measurements

I.3.1. Electrolytes

I.3.1.1. Introduction to Solvents

The basic requirements of a suitable electrolyte for electrochemical devices are high ionic conductivity, low melting and high boiling points, chemical and electrochemical stability, and safety. Electrolyte conductivity and electrochemical stability are key parameters in selecting an electrolyte for modern electrochemical devices such as advanced batteries, fuel cells, super-capacitors, sensors, and electrochromic displays. Although progress has been made in enhancing the conductivity of solid electrolytes, particularly the polymeric electrolytes, the liquid electrolytes are still used in most electrochemical systems. The solvent properties and dynamics of ion solvent interactions, must be understood in designing new electrolytes. In the following section a short but general introduction to properties of solvents and ion-solvent dynamics is discussed.

The history of electrolyte development goes as far back as the work of Greek philosophers in search for a universal solvent, the so-called "Alkahest". In search of Alkahest, many solvents and chemical rules were discovered such as "like dissolves like" (*similia similibus solvuntur*) as shown in Table (I.3.1). Later the theory of osmotic pressure by van't Hoff (1852-1911), and the theory of electrolyte dissociation by Arrhenius (1859-1927) were discovered. Many speculations about the nature of solute-solvent interactions and the influence of solvent media on the rate of chemical reaction were proposed in the early eighteen-century. The role of solvents on chemical

equilibrium, on tautomerism (i.e. keto-enol tautomerism), and the phenomenon of solvatochromism (shift of UV/Vis absorption bands due to the changes of the index of refraction) were discovered [27,28] . Scheibe et al.[29] have correlated the solvating ability of solvents to their degree of influence on reaction rate, chemical equilibrium, and shift in absorption spectra.

Table I.3.1: Various solvents with different degree of hydrophobicity.

Compound		Well soluble in
Hydrocarbons	hydrophobic	Hydrocarbons, Ethers,
Halohydrocarbons		Halohydrocarbons
Ethers		
Amines		
Esters		Carboxylic Esters
Nitrohydrocarbons		
Nitriles		
Ketones		Alcohols, 1,4-Dioxane
Aldehydes		Acetic Acid
Phenols		
Amides		
Alcohols		Alcohols, Water
Carboxylic Acids		
Sulfonic Acids		
Salts	hydrophilic	Water

In the early 19th century, it was much argued that solvents and electrolytes should not be considered as a continuum, usually characterized by their physical properties such as dielectric constant, density, index of refraction, etc., but as a discontinum with mutually interacting molecules. It was discovered in many instances that the density of the solvent in solvation shells around small cations are greater than that of the bulk solvent, due to the strong ion-solvent interactions. The interaction forces between solvent

molecules are too big to be treated like gases but not significant enough to be considered as solids. Although the nearest neighbor distances in liquid and solids are very close, the volume of liquid is about 10% greater than the solid forms, due to the significant defects that exist in the coordination number of ions in the liquid state. In addition, the solvent molecules in the solvation shell of an ion have a short residency time, and the dynamics of solvent exchange processes vary in a wide range, depending on the size and charge of the ions and the chemical nature of the solvent. In some cases the solvation shell is stable enough that the complex can be considered as a molecular entity, e.g. $[Co(NH_3)_6]^{2+}$. On the other hand, in some cases the solvent exchange is faster than the time scale of NMR, and solvent molecules in the solvation shell cannot be distinguished from those in bulk solution. The complexity of interactions in liquid state makes the theoretical treatment of electrolyte structure a difficult task, and still most reliable data are those obtained experimentally, using NMR, Vibrational spectroscopy, and fast spectroscopy techniques.

When dealing with mixed solvents, the solubility parameter relates to the molar enthalpy of vaporization for a gas of zero pressure by [30];

$$\text{Hildebrand parameter} = \delta = [(\Delta H_v - RT)/V_m]^{1/2} \qquad \text{(I.3.1)}$$

where, V_m is the molar volume and ΔH_v is the molar enthalpy of vaporization. The δ is the measure of work necessary to separate solvent molecules to create a cavity to accommodate the solute.

I.3.1.2. Columbic forces between ions and dipolar solvents

In addition to the intermolecular forces, such as van-der Waals forces and the well-known hydrogen bonding forces responsible for the non-ideal behavior of solvents and electrolytes, there are other important forces between ions and neutral molecules with permanent dipole moments (dipolar solvents) that can alter the physical and chemical properties of solvents. The most important forces which exist between solvent molecules and solute-solvents are discussed in the following section.

I.3.1.3. Ion-Dipole Forces

Solvents with unsymmetrical charge distribution (dipolar solvents) possess a permanent dipole moment, μ. The magnitude of the dipole moment depends on the value of charges on the opposite sides of the molecule and their separation distance as defined by $\mu = q \cdot r$, where the q is the charge (assuming equal value of charge on each side of the molecule), and the r is the separation distance between the charges [31]. Most organic solvents have permanent dipole moment in a wide range from 0 to 18×10^{-30} Coulomb-meters, (Cm). In particular, cyclic and linear organic carbonates, used in this work, have a large difference in permanent dipole moment, (i.e. $\mu_{\text{propylene carbonate}} = 16.7 \times 10^{-30}$ C.m, and $\mu_{\text{diethyl carbonate}} = 3 \times 10^{-30}$ C.m). The dipole moment, relative dielectric constant, melting point, and boiling point of several common organic solvents are listed in Table I.3.2. The water molecule is also listed as a reference for comparison.

Table I.3. 2: Common dipolar organic solvents and their physical properties [32-34].

Solvent	t_{mp}/°C	t_{bp}/°C	ε	μ(10^{-30}Cm)	n^{20}
Water	0.0	100	78.30	5.9	1.3330
Formamide	2.55	210.5	111.0	11.2	1.4475
Methanol	-97.7	64.5	32.66	5.7	1.3284
Ethanol	-114.5	78.3	24.55	5.8	1.3614
Acetic acid	16.7	117.9	6.17	5.6	1.3719
Cyclohexanol	25.15	161.1	15.0	6.2	1.4648
Propylene Carbonate	-54.5	241.7	64.92	16.5	1.4215
Nitromethane	-28.55	101.2	35.94	11.9	1.3819
Acetonitrile	-43.8	81.6	35.94	11.8	1.3441
Dimethyl sulfoxide	18.5	189.0	46.45	13.5	1.4793
Aniline	-6.0	184.4	6.71	5.0	1.5863
Sulfolane	28.45	287.3	43.3	16.0	1.4816
Acetone	-94.7	56.1	20.56	9.0	1.3587
Cyanobenzene	-12.75	191.1	25.20	13.4	1.5282
Nitrobenzene	5.8	210.8	34.78	13.3	1.5562
Hexamethylphophoric Acid triamide	7.2	233	29.6	18.5	1.4588
Acetophenone	19.6	202.0	17.39	9.8	1.5342
Pyridine	-41.55	115.25	12.91	7.9	1.5102
Methyl acetate	-98.05	56.9	6.68	5.7	1.3614
Cyclohexanone	-32.1	155.65	16.10	10.3	1.4510
Quinoline	-14.85	237.1	8.95	7.3	1.6273
Tetrahydrofuran	-108.4	66.0	7.58	5.8	1.4072
Diethyl carbonate	-43.0	126.8	2.82	3.15	1.3837
Dimethyl carbonate	4	90	3.12	2.95	
Methyl-propyl carbonate	–49	130	3	4.84	
Methyl-isopropyl carbonate	–76	117	3	4.92	
Ethyl-propyl carbonate	–81	148	3	5.25	
Ethyl-isopropyl carbonate	–132	135	3		
Ethylene carbonate	36.4	238	89	4.87	
1,4-Dioxane	11.8	101.3	2.21	1.5	1.4224
Trichloroethene	-86.4	87.2	3.42	2.7	1.4773
Diethyl ether	-116.3	34.4	4.20	3.8	1.3524
Benzene	5.5	80.1	2.27	0.0	1.5011
Toluene	-95.0	110.6	2.38	1.0	1.4969
Carbon disulfide	-111.6	46.2	2.64	0.0	1.6275
Tetrachloromethane	-22.8	76.6	2.23	0.0	1.4602
n-Hexane	-95.3	68.7	1.88	0.0	1.3749

t_{mp} = melting point, t_{bp} = boiling point, ε = dielectric constant, μ = dipole moment, n^{20} = refrective index at 20 °C.

A solvent molecule with a permanent dipole when placed in the field of an ion, orients itself to minimize its mutual potential energy so that the attractive end of the solvent becomes directed toward the ion and the repulsive end orients itself away from the ion. The ion-dipole interaction energy is given by [35],

$$U_{ion\text{-}solvent} = - (ze\mu \cos \theta)/(4\pi\varepsilon_o)\, r^2 \qquad (I.3.2)$$

where the z.e is the charge of the ion, θ is the dipole angle relative the line joining the ion to the center of dipole, and ε_o is the vacuum permitivity. For a monodendate ion-solvent configuration, the solvent molecule and the ion are aligned on the same line, and $\theta = 0$. The ion-dipole forces are very important on the relative stability of the solvation shells. It also plays a major role on preferred solvation when multi-component solvents are used.

I.3.1.4. Dipole-dipole Interactions

Solvent molecules with permanent dipole moments interact with each other via directional electrostatic interactions. The dipole-dipole orientation is strongly temperature dependent, and thermal energy prevents optimum orientation of solvents toward each other. The dipole orientation is statistically favored, and at higher temperatures all other dipole orientations become more populated. The dipolar interaction is mainly responsible for the association of dipolar solvents [36,37]. The dipole-dipole interaction is given by [38],

$$U_{dipole\text{-}dipole} = - (2\mu_1^2\, \mu_2^2)/(4\pi\varepsilon_o)3K_BT\, r^6 \qquad (I.3.3)$$

where K_B is the Boltzmann constant, and T is the absolute temperature.

I.3.1.5. Dipole-Induced Dipole Interactions

A solvent with permanent dipole moment can induce a dipole moment in its neighboring solvents. The magnitude of the induced dipole moment depends on the polarizability of the solvents, α, and is defined as [39],

$$\mu_{induced} = 4\pi\varepsilon_o \alpha E \qquad \text{(I.3.4)}$$

where E is the electric field strength. The induced moment is directional and lies along the induced dipoles. The energy of dipole-induce dipole interaction between solvent molecules is given according to the following equation [39],

$$U_{dipole\text{-}induced\ dipole} = -(\alpha_1\mu_2^2 + \alpha_2\mu_1^2)/(4\pi\varepsilon_o)r^6 \qquad \text{(I.3.5)}$$

In addition to the solvent-solvent molecules induced dipole moment interaction, there is also strong induced polarization of solvent by ions in the electrolytes. The magnitude of the ion-solvent induced polarization depends on the polarizability of the solvent molecules and the degree of distortion of the molecule's electron cloud. The energy of ion-induced dipole interaction is defined as [39],

$$U_{ion\text{-}induced\ dipole} = -(z^2e^2\alpha)/(4\pi\varepsilon_o)2\,r^4 \qquad \text{(I.3.6)}$$

I.3.1.6. Instantaneous Dipole-Induced Dipole Interaction Forces

In general, the electron movement in one species (atom or molecule) induces a small dipole moment that polarizes the electron cloud in its neighboring system. This induced interaction is called the dispersion interaction and strongly depends on polarizability and ionization potential of interacting species according to the following equation [40],

$$U_{dispersion} = - (3\alpha_1\alpha_2)(I_1I_2)/(I_1+I_2)2\ r^6 \qquad (I.3.7)$$

where the I is the ionization potential. The dispersion energy between two similar molecules then will be reduced to,

$$U_{dispersion} = - (3\alpha^2I)/4\ r^6 \qquad (I.3.8)$$

The dispersion energies are very short range as expressed in $1/r^6$. This is very important for molecules with polarizable π electrons. The molecular aggregation of polyaromatics molecules discussed in chapter 6, are mainly related to the dispersion energy among polyaromatics molecules with conjugated π electrons. From the equations above, it is clear that the dispersion energy also is important for the cohesion of molecules with high polarizability values. For example, the dispersion interaction energy of two molecules with $\alpha = 3x10^{-30}$ m^3, and $I = 20x10^{-19}$ J, and $r = 3x10^{-10}$ m is calculated to be –11.3 kJ/mol or –2.7 kcal/mol (35). For a similar molecular system the dipole-dipole energy is only –5.3kJ/mol or –1.1 kcal.mol [41].

The dispersion forces depend highly to the polarizability of the solvent. The polarizability is also connected to the refractive index according to the Lorenz-Lorenz equation [42].

$$\frac{n^2-1}{n^2+2}.V_M = \frac{4\pi N\alpha}{3} = \text{Molar refrective index} \qquad \text{(I.3.9)}$$

where V_M is the molar volume. For the low frequency radiation, the static dielectric constant is related to the refractive index by the Maxwell derived equation, $n^2 = \varepsilon$.

Solvents with large index of refraction and large optical polarizability should have a large value of dispersion forces. Most aromatic and polyaromatics molecules have a large refractive index, e.g. quinoline (n = 1.6273), diphenyl ether (n = 1.5763). In general, solvents with high polarizability are good solvents for anions with high polarizability. This is important, particularly when designing a salt to have a high cation transference number and a low anion transference number under an electric field. In a liquid electrolyte, the ionic conduction is related to both the anion and the cation mobility and their transference number. The total cation and anion transference number is equal unity [43].

$$t_+ + t_- = 1 \qquad \text{(I.3.10)}$$

where the t_+ and t_- are the transference numbers, the portion of charge carried by cations or anions respectively.

I.3.1.7. Hydrogen Bonding

Hydrogen bonding is significant for molecules possessing hydroxyl or other groups that hydrogen is connected to an electronegative atom. The abnormaly high boiling points of many solvents with high degree of hydrogen bonding are well known. The hydrogen bonding can occur between two similar molecules to form homo-intermolecular hydrogen bonds or between two different solvent molecules called hetro-intermolecular hydrogen bonds. The hydrogen bonds also can be formed either intermolecularly or intramolecularly. For example in 2-nitrophenol, depending on Lewis basicity of the solvent, inter- and intra-molecular hydrogen bonds are formed. Various conformations of hydrogen bonds are possible depending on the nature of solvents and solutes.

Dipolar organic solvents, usually with a large dielectric constant and a rather high dipole moments, do not strongly participate in hydrogen bonding, when their hydrogen is not connected to a strong electronegative atom (O, N, S, etc). Their C-H bond is not strongly polarized. However, they may participate in electron pair donors (EPD), electron pair acceptor (EPA) process discussed in section I.3.1.8.

I.3.1.8. Electron Pair Donor-Electron Pair Acceptor Interactions (EPD/EPA Interactions)

Molecules with high energy, occupied orbitals, and molecules with a sufficiently low energy unoccupied orbital, form electron pair donor electron acceptor complexes. The long-wavelength absorption nature of EPD/EPA complexes is associated with the electron transfer from the donor molecule to the acceptor. This type of optical absorption is called the "charge-transfer" or CT absorption. Three classes of EPD molecules have been accepted based on the involvement of *n*-, σ, and π orbitals. For the n-group, the highest energy orbital is the lone-pair of a hetroatoms (R_2O, R_3N, R_2SO, etc.). The σ types are the involvement of the σ-type bond (R-Hal), and the π-type association is the involvement of a pair π-electron of unsaturated molecules (alkyl benzenes, polycyclic aromatics, etc.).

A similar classification also exists for electron acceptor molecules, when *n*, σ, or π orbitals are involved. Therefore nine different combination of EPD/EPA association have been distinguished. The reaction enthalpy of the EPD/EPA associations is used as their bond strength, and varies between –42 to 188 kJ/mol (-10 to 45 kcal/mole) [44]. The enthalpy of formation of a n-EPD/ σ-EPA, such as Et_2O-BF_3, is –50kJ/mole, -11.9 kcal/mole, and for a π-EPD/π-EPA such as benzene/1,3,5-trinitobenzene is –8 kJ/mole or –1.9 kcal/mole.

The n-donor solvents strongly solvate cations in electrolytes. They are good solvents for salts and they are known as coordinating solvents [45]. The n-donor solvents are good media for inorganic reactions. Examples of n-donor solvents are pyridine, dimethyl sulfoxide, triamide, N,N-dimethylformamide, acetone, methanol, and water.

Gutmann and coworkers [46,47] have developed a semi-quantitative scale for the degree of nucleophilic properties of EPD-solvents, called the Donor Number (DN) or donicity. The donicity is defined as the negative ΔH value for 1:1 adduct formation between the antimony pentachloride ($SbCl_5$) and the electron pair donor solvent (EPD), in a dilute solution of non-coordinating 1,2 dichloroethane solvent, according to the following equation.

$$EPD: + SbCl_5 \xrightarrow[\text{At room temperature}]{Cl\text{-}CH_2\text{-}CH_2\text{-}Cl} EPD^{+}\text{-}\ ^{-}SbCl_5$$

$$\text{The solvent Donor Number} = DN = \text{Donicity} = -\Delta H_{EPD\text{-}SbCl5/(kcal/mole)}$$

The donor number is a very useful concept and correlates well with the electrochemical half-wave redox potentials, kinetic rates, and the NMR chemical shift signals for various EDP solvents [46-52]. The Donor Number of some common organic solvents are listed in Table I.3.3.

Table I.3.3: Donor number of common organic EPD solvents determined by calorimetry in dilute 1,2 dichloroethane solution at room temperature [46-52].

Solvents	DN/(Kcal.mol^{-1})
1,2-Dichloroethane (reference solvent)	0.0
Nutromethane	2.7
Nitobenzene	8.1
Acetic anhydride	10.5
Sulfolane	14.8
1,4 Dioxane	14.8
Propylene carbonate	15.1
Diethyl carbonate	16.0
Ethylene carbonate	16.4
Methyl acetate	16.5
Acetone	17.0
Ethyl acetate	17.1
2-Butanone	17.4
Diethy ether	19.2
Tetrahydrofuran	20.0
Trimethyl phosphate	23.0
N,N-Dimethylformamide	26.6
Dimethl sulfoxide	29.8
N,N-Diethylformamide	31.0
Triethylamine	31.7
Pyridine	33.1
Hexamethylphosphoric triamide	38.8

A quantitative electron accepting ability (accepting number, AN) for electron pair acceptor solvents has also been developed to determine their electrophilic properties. This concept is developed by Gutmann and coworkers based on ^{31}P-NMR chemical shift of triethyphosphane oxide in presence of an EPA-solvents at room temperature [53-55].

$$(Et_3P{=}O \leftrightarrow Et_3P^{+}\text{-}\bar{O}) + EPA_{solvent} \leftrightarrows Et_3P^{\delta+}{=}{}^{\delta-}O - A$$

$$AN = \frac{\delta_{corr}(A) - \delta_{corr}(n-C_6H_{14})}{\delta_{corr}(Et_3PO - SbCl_5) - \delta(n-C_6H_{14})}.100 = \Delta\delta_{corr}.2.348/ppm \quad (I.3.11)$$

Table I.3.4: Acceptor number (acceptivities) of common EPA organic solvents, [53-55], determined form ^{31}P-NMR chemical shift value spectroscopically at room temperature.

Solvents	AN
n-Hexane (reference solvent)	0.0
Triethylamine	1.4
Diethyl ether	3.9
Tetrahydrofuran	8.0
Benzene	8.2
Tetrachloromethane	8.6
Ethyl acetate	9.3
Diethylamine	9.4
Tri-n-butyl phosphate	9.9
Diethylene glycol dimethyl ether	9.9
Hexamethylphosphoric acid triamide	10.6
Methyl acetate	10.7
1,4- Dioxane	10.8
Acetone	12.5
Pyridine	14.2
Nitrobenzene	14.8
Cyanobenzene	15.5
N,N-Dimethylformamide	16.0
Trimethyl phosphate	16.3
1,2-Dichloroethane	16.7
Propylene carbonate	18.3
N,N-Dimethylthioformamide	18.8
Tetrahydrothiophen-1,1-dioxide, sulfolane	19.2
Dimethyl sulfoxide	19.3
Dichloromethane	20.4
Nitromethane	20.5
Chloroform	23.1
2-Methyl-2-propanol, t-Butanol	27.1
N-Methylformamide	32.1
2-Propanol	33.6
1-Butanol	36.8
1-Pronanol	37.3
Ethanol	37.9
Formamide	39.8
Methanol	41.5
Acetic acid	52.9
2,2,2-Trifluoroethanol	53.3
Water	54.8
Formic acid	83.6
$Et_3PO.SbCl_5$, in 1,2-dichloroethane as reference compound	100.0
Trifluoroacetic acid	105.3

AN is the acceptor number or acceptivity and they are obtained from the relative ^{31}P-NMR chemical shift values related to the 1:1-adduct $Et_3P{=}O - SbCl_5$ dissolved in 1,2-dichloroethane. The chemical shift for n-hexane has been used as reference, $AN_{n\text{-}hexane} = 0$. The AN value of a number of common organic solvents are listed in Table I.3.4. The acceptor numbers are dimensionless number relative to those of $SbCl_5$.

I.3.1.9. Solvation

The interaction between ions and solvent molecules is important in electrolytic media. The shell formed around the ions by solvent molecule is termed solvation. In an aqueous electrolyte this known as hydration. The energy of solvation is the change in Gibbs energy when an ion is transferred from vacuum into a solvent. The value of solvation energy, $\Delta G_{solvation}$, is the solvation ability of the solvent. In order to dissolve a salt in a solvent, the interaction energies between solvent molecules, including the all-electrostatic, polarization, and dispersion energies, as well as the lattice energy of the salt, must be overcome.

The electrostatic field that solvent molecule experience in close proximity of the ion in a solvation shell is in the order of $10^6 - 10^7$ V/cm. This enormous field increases the density of the solvent in a solvation shell as compared to that of the bulk solution. The effect of solvation in different media on chemical reaction rates is well known, and in most cases the solvent media need to be mentioned in defining the reaction kinetics. Criss and Salomon have provided a comprehensive compilation of Gibbs free energies of solvation [56].

I.3.1.10. Solvation Number

The solvation number is the number of solvent molecules in the primary shell attached to the ion in a way that their translational and rotational motions exhibit changes from the bulk solution. In some cases, the solvent molecules in the second sphere around the ion, also considered as solvation number. However, in most cases, the number of solvent molecules in the primary shell is known as the solvation number. The residency time of a solvent molecule in the solvation shells are still short, so that in most cases they can be monitored in the time scale of NMR spectroscopy. The ^{17}O-NMR spectroscopy of Al^{3+} and alkali ions in aqueous solution has indicated a slower than 10^4/sec solvent exchange for Al^{3+} and faster than 10^4/sec exchange for the Alkali ion hydration [57,58]. NMR spectroscopy has proved to be a very useful tool for studying the dynamic of solvent molecule in solvation shells of various ions.

The solvation number is usually measured by electrolytic transport methods. The solvation number is higher for the harder ions (small size), as compared to the softer ions (large size), with similar charge [59,60]. The data from electrolytic transport measurement and from conductance measurements indicate that solvation numbers increases according to: $Li^+ > Na^+ > K^+ > Rb^+ > Cs^+$; the alkaline earth ions are more solvated than the alkali ions: $Mg^{++} > Ca^{++} > Sr^{++} > Ba^{++}$. The anions solvation number have also shown similar trends, as: $F^- > Cl^- > Br^- > I^-$ [61].

I.3.1.11. Selective or Preferred Solvation

In mixed solvents containing salt, e.g. binary or ternary solvent electrolytes, the interaction of solvent-solvent molecules and ion-solvent interactions are complicated. It is often observed that the ratio of solvent molecules in the solvation shell is different from that of the bulk solution. The ions in the electrolyte tend to solvate themselves more with the solvent molecules that produce more negative Gibbs energy of solvation, $\Delta G_{solvation}$. This preferred solvation produces an inhomogenity in the solvation shell and in the bulk of mixed solvent electrolyte. When the cation and the anion are preferentially solvated with the same solvent it is called homoselective solvation, and when the cation is solvated preferentially by one solvent and the anion by other solvent molecules, it is called hetroselective solvation [62,63].

Several methods have been developed to study selective solvation in multicomponent electrolytes. The IR and NMR spectroscopy have been used most by spectroscopists and the conductance method and Hittorf transference measurements by electrochemists [62].

I.3.2. The Basic Requirements of Electrolyte for Lithium Batteries

A suitable electrolyte for lithium battery must have the following characteristics:

1. High ionic conductivity to minimize the cell resistance and resistive heating of the device.

2. High chemical stability to prevent decomposition of electrolyte on the surface of a highly reducing anode materials, e.g. metallic lithium or lithiated graphite, (LiC_6), and highly oxidizing cathode materials such a delithiated $Li_{1-x}MO_2$ electrodes, where M = Co, Ni, Mn, or mixed transition metals.

3. Electrochemical stability to tolerate the high voltage difference between the anode and the cathode (>4V). Not many organic solvent can tolerate such wide voltage range without being reduced or oxidized.

4. Low melting point to provide sufficient conductivity at sub-ambient temperature and prevent solidification and phase separation.

5. High boiling point to provide safety and prevent explosions resulting from high pressure build-up in the cell.

6. Non toxicity to be accepted environmentally for ease of handling, mass production, and waste treatment.

7. Low cost to be affordable and compete with existing power sources that uses aqueous electrolytes.

Although progress has been made in enhancing the conductivity of solid electrolytes, particularly the polymeric systems, the liquid electrolytes are still used in most electrochemical devices, particularly when high-power applications are in demand.

The above characteristics have been considered in selecting electrolytes in this work. Among various solvents presented in Table I.3.2, the organic carbonates, particularly the cyclic carbonates are the most suitable solvents for application in a battery electrolyte. However, the viscosity of the cyclic carbonates is slightly high and needs to be modified to improve their low temperature performances. Addition of a linear carbonate with high fluidity enhances the ionic conductivity of multi-solvent blend electrolytes. Conductivity of several organic carbonates at various salt concentrations at different temperatures has been measured. The salt concentration was chosen from 0.4M to 1M of lithium salt, $LiPF_6$. Below 0.4M salt concentration a marked decrease in conductivity of the electrolyte was observed and considered not to be practical. Above the 1M concentration, there is significant salt precipitation at low temperatures, (T<-20° C), that is detrimental to most electrochemical devices. The temperature range was selected from –40 to 50°C. This is a practical temperature range that most electrochemical devices may operate. It has been shown that there is no electrolyte with a single solvent that can provide all the requirements of a practical electrolyte. Therefore

multi component electrolytes containing multi-blend solvents are used. Several binary and ternary organic carbonate solvents are used to enhance the performance of the electrolytes, particularly their low temperature conductivity. The viscosity of the mixed solvent was modified and higher fluidity was observed when linear carbonates where mixed with high viscosity cyclic carbonates. In fluid dynamics, the mixing rules for the viscosity and dielectric constant have been defined [64].

$$\text{Log } \eta_{\text{mixture}} = x_1 \log\eta_1 + x_2 \log\eta_2 + x_3 \log\eta_3 + \ldots \qquad \text{(I.3.12)}$$

where x_i is the mole fraction of solvent I and η_i is the viscosity of the component i.

$$\varepsilon_m = y_1\,\varepsilon_1 + y_2\,\varepsilon_2 + y_3\,\varepsilon_3 + \ldots \qquad \text{(I.3.13)}$$

where the $y_i = x_i V_i / V_m$ = volume fraction of component I, and the V_i is the molar volume fraction of component i, and the V_m is the molar volume of mixture (cm^3/mole),

$$V_m = x_i V_i + x_2 V_2 + \ldots \qquad \text{(I.3.14)}$$

Electrolytes are composed of a lithium salt ($LiClO_4$, $LiPF_6$, $LiCF_3SO_3$, etc) dissolved in high purity cyclic and linear organic carbonates. There are also examples of binary and ternary solvent blends which have been used in an attempt to improve the low-temperature conductivities. The composition of nonaqueous electrolyte solutions for secondary lithium batteries plays an important role in battery cycle life, cell performance, operating temperature range, and storage life (shelf life). There are several reviews

concerning the conductivity and properties of nonaqueous electrolyte solutions [65-69]. However most organic electrolytes decompose anodically or cathodically when cycled between 0-4V against a lithium electrode. There have been extensive investigations to find a stable organic electrolyte above 4V. The organic carbonates have shown stability even up to 5 V vs Li reference electrode. In fact, this remarkable stability of organic carbonate-based electrolytes provide the opportunity to use high voltage cathodes materials (layered $LiCoO_2$ and 3-D spinel $LiMn_2O_4$ cathodes). The average voltage of a single cell in Li-ion battery (LiC_6//$LiCoO_2$) is 3.75V and it operating voltage range is between 3 volt to 4.5 volts. This class of advanced lithium battery uses carbonate-based electrolytes.

The anodic decomposition of organic electrolytes also has been a major concern, as there is no organic electrolyte that can tolerate the reducing power of metallic lithium or lithium doped graphite that most of its capacity in 0.01 to 0.3 volt vs a lithium reference. In fact the reason that current anodes work so well is mainly because of the formation of a protective layer on the surface of anode. This protective layer is formed by decomposition of organic solvent and commonly called "solid electrolyte interface", SEI layer. The nature of SEI depends on the organic solvents used in the battery. The SEI is electronically insulating, but has significant lithium ion conductivity and allows the lithium ions to reach the anode. The SEI layers that are formed in carbonate-based electrolytes are remarkable in their protection of the anode. The chemical nature of the SEI layers formed on lithiated carbonaceous anodes will be discussed in Chapter 4.

The salt used in the used in lithium batteries also must be stable in a wide voltage range (0-4.5 volts). $LiPF_6$ is the most studied salt in lithium battery use, and is exclusively used in almost all advanced high voltage lithium cells. $LiPF_6$ is stable up to 151 °C. One of the major issues with $LiPF_6$ is to remove the residual HF that is adsorbed on the salt during the synthesis process. The HF can be removed without decomposition of salt around 60-70 °C under vacuum. The thermogravimetric analysis of $LiPF_6$ has shown removal of HF around 65 °C and decomposition of the salt to LiF and PF_5 around 150°C. $LiPF_6$ is extremely moisture sensitive and reacts with residual water in the electrolyte and forms HF that is detrimental to the performance of the cell, particularly on the cathode side. The released HF also reacts with the anode to form LiF, which is a poorly ionic conductor and increases the impedance of the electrode/electrolyte interface. There is an extensive search to develop a novel lithium salt for lithium batteries [70-78].

I.3.3. Experimental

High purity cyclic carbonates such as propylene carbonate, (PC), ethylene carbonate, (EC), and linear carbonates; such as dimethylcarbonate (DMC), diethyl carbonate (DEC), and asymmetric linear carbonate, methyl ethyl carbonate (MEC) solvents were purchased from Fluka. In order to reduce the residual moisture, the solvents were stored over molecular sieves for at least 48 hours. Electrolytes were prepared in a dry box filled with 99.999% Argon. The atmosphere of the box was continuously circulated over Cu shaving catalyst to remove residual moisture and over titanium sponge at 700°C to remove residual oxygen, and nitrogen. The dry box was a vacuum atmosphere model MO-40-2H/DRI, equipped with Nitrian and catalyst

recirculating unit. A 40 W tungsten light bulb was cracked and installed in the box to monitor the purity of the box atmosphere. Usually each lamp last over two months before burning out. Conductivity measurements were performed using dip cells (model A-01 with cell constant 0.1) from Rosemount Analytical Inc. This cell uses two platinized parallel plates fixed in a cylindrical glass cavity. The electrode is dipped in the electrolyte and remained there for at least 5 minutes before measurements were taken. The cell was connected to a Genrad model GR 1689/1689M precision RLC Digibrige.

I.3.3.1. Solvents:

Solvents used were ethylene carbonate (EC) , diethyl carbonate (DEC), dimethyl carbonate (DMC), and propylene carbonate (PC), and methyl ethyl carbonate (MEC). Different combinations of electrolyte were prepared by adding 1M solute of lithium hexafluorophosphate ($LiPF_6$, Hashimoto) to either 1:1 of EC/DEC, EC/PC, EC/DMC, DEC/PC, DEC/DMC, PC/DMC (1/1 by volume). Solvents and salt were used as received. Table I.3.5. shows the various solvents and electrolytes used in this work.

Table I.3.5: Solvents and electrolytes used in this study

EC	DEC	DMC	PC	EMC
EC-$LiPF_6$	DEC- $LiPF_6$	DMC-EC	PC-$LiPF_6$	EMC- $LiPF_6$
EC-DEC- $LiPF_6$	DEC- EC-$LiPF_6$	DMC-DEC	PC-DEC-$LiPF_6$	EMC-EC-$LiPF_6$
EC-DMC- $LiPF_6$	DEC-PC- $LiPF_6$	DMC- $LiPF_6$	PC-DMC-$LiPF_6$	EMC-PC-$LiPF_6$
EC-PC- $LiPF_6$	DEC-EC-PC- $LiPF_6$	DMC-PC- $LiPF_6$	PC-EC-DMC-$LiPF_6$	EMC-EC-PC-$LiPF_6$

I.3.3.2. Materials

Pure solvents

1. Dimethyl carbonate (DMC), diethylene carbonate (DEC), methyl ethyl carbonate (MEC), ethylene carbonate (EC), and propylene carbonate (PC).

Single solvent electrolyte:

2. DEC + (0.4-1M)$LiPF_6$, DMC + (0.4-1M)$LiPF_6$, MEC + (0.4-1M)$LiPF_6$, EC+ (0.4-1M)1M$liPF_6$ and PC+(0.4-1)M$liPF_6$.

Binary electrolytes (1:1) with (0.4-1M) $LiPF_6$ salts:

3. EC + DEC(1:1) + (0.4-1)M$liPF_6$, EC + PC(1:1) + (0.4-1M)$LiPF_6$, and EC + DMC(1:1) + (0.4-1M)$LiPF_6$.

Ternary solvent electrolytes with (0.4-1M) $LiPF_6$ salts:

4. EC + DMC + PC + (0.4-1M)$LiPF_6$, EC + PC + DEC + (0.4-1M)$LiPF_6$, EC + EMC + PC + (0.4-1M)$LiPF_6$.

The electrolytes used in this work contain 0.4M, 0.6M, 0.8M, and 1M of $LiPF_6$. For each conductivity measurement the cell was washed with methanol and vacuum dried at 100° C. The cell was filled with electrolytes inside of a dry box filled with pure Argon. The cell was sealed and transferred from the box for conductivity measurements.

I.3.3.3. Conductivity Measurements

The conductivity cell was thermally equilibrated at the temperature of measurement for 30 minutes or when the cell temperature did not change for 10 minutes. The conductivity value was measured using a Genrad model GR1689 M precision RLC Digibrige. A Teflon top was designed to cover the conductivity cell to prevent possible evaporation of solvent. The solvent evaporation during conductivity measurement was negligible even at 60°C. During conductivity measurements, it is important to maintain the electrolyte temperature constant. A constant temperature circulating bath with an accuracy of 0.1°C was used. The conductivity was measured from -40 to 50°C. This temperature range is normally accepted for testing electrolytes for battery applications.

I.3.4. Results and Discussions

I.3.4.1. Conductivity of single solvents versus concentrations and temperatures

Conductivity of various electrolytes based on organic carbonate solvents containing $LiPF_6$ was measured. Three sets of conductivity measurements were performed. The first class of electrolytes contained only single carbonate solvent with different concentration of salt. The salt concentrations were chosen as 1M, 0.8M, 0.6M, and 0.4M. Figure I.3.1 shows the conductivity of the electrolyte made from Propylene carbonate and $LiPF_6$.

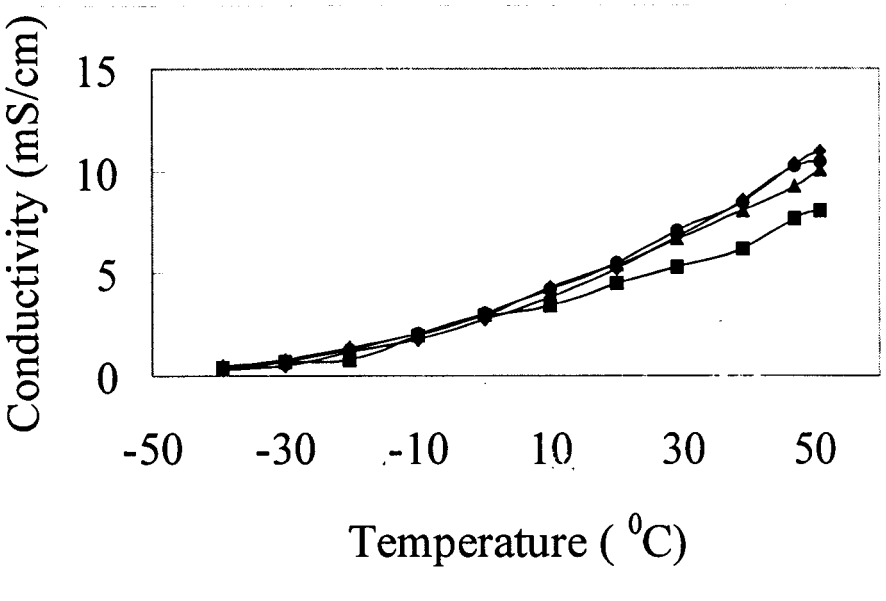

Figure I.3.1: Conductivity of propylene carbonate containing, (♦) 1M, (●) 0.8M, (▲) 0.6M, and (■) 0.4M of $LiPF_6$ from –40 to 50°C .

The conductivity of PC-$LiPF_6$ is effectively similar at low temperatures (t<0°C) for various salt concentrations. Only at high temperatures the conductivity increases at higher salt concentrations. Even at high temperatures, the conductivity of 1M solutions and 0.8M solutions are indistinguishable. This is important, as the lithium batteries operate in this range of temperatures (-40 – 50°C), there is no need to use 1M electrolytes and the 0.8M can provide the same conductivity as 1M solutions. This may reduce the cost of salt in lithium battery by 20%. The salt is one of the most expensive components of the cell. A similar trend was observed for other carbonate solvents.

Figure I.3.2. shows the conductivity of dimethyl carbonate (DMC) containing 1M, 0.8M, 0.6M, and 0.4M of $LiPF_6$. The boiling point of the DMC is 87°C . Therefore care must be taken to prevent evaporation of the solvent during conductivity

measurements around 50°C . The Teflon top, described before, prevents significant evaporation of electrolyte solvent during conductivity measurements.

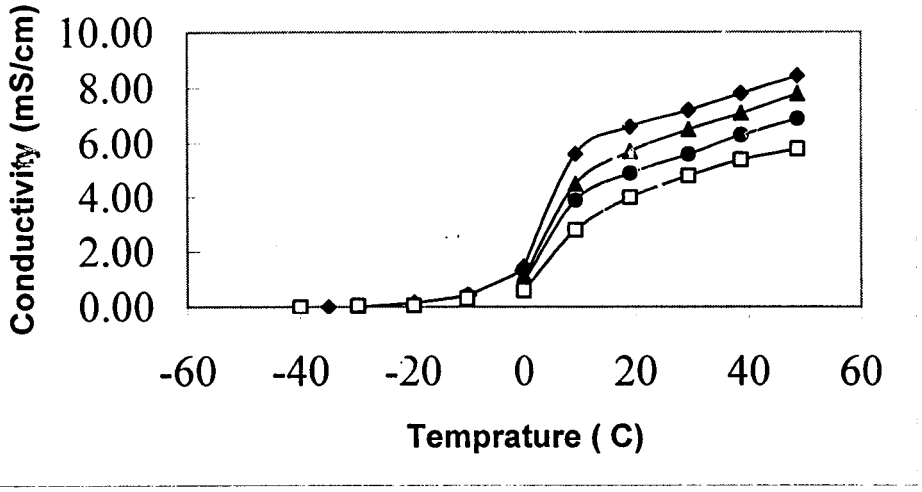

Figure I.3.2: Conductivity of dimethyl carbonate containing, (♦) 1M, (▲) 0.8M, (●) 0.6M, and (□) 0.4M $LiPF_6$.

The conductivity of dimethyl carbonate markedly decreases around 0°C. In addition, the conductivity of the DMC based electrolyte is negligible below 0°C, and is not practical for battery application. However, their conductivities are higher than propylene carbonate based electrolytes above 30°C. The behavior of electrolyte containing mixed PC-DMC solvents will be discussed in the section of multicomponent electrolytes.

The conductivity of an asymmetric linear carbonate solvent containing various amounts of $LiPF_6$ is shown in Figure I.3.3. The conductivity of methyl ethyl carbonate (MEC) based electrolytes containing $LiPF_6$ remain high even at low temperatures (-40°C). This solvent as shown in Table I.3.1 has very low melting point. It is interesting

that substituting one of the methyl groups from DMC with an ethyl group significantly affects the melting and boiling temperatures of MEC-based electrolytes. The substitution of methyl group with an ethyl one introduces significant disorder in the electrolyte system that markedly changes the glass transition and the fluidity of this solvent. The asymmetric solvents such as MEC are good candidates for low temperature electrolyte and investigation of the electrochemical properties of materials at low temperatures.

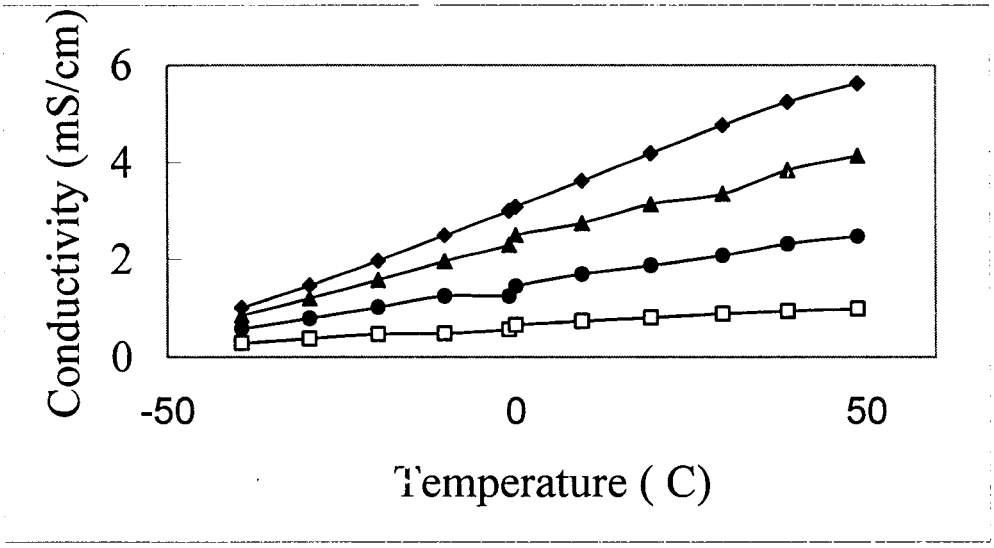

Figure I.3.3: Conductivity of methyl ethyl carbonate (MEC) containing, (♦) 1M, (▲) 0.8M, (●) 0.6M, and (□) 0.4M $LiPF_6$.

I 3.4.2. Conductivity of binary solvents –$LiPF_6$ electrolytes versus concentrations and temperatures

The requirements of the electrolyte for a lithium battery are very demanding and it is almost impossible to find a single solvent electrolyte to meet all the contradictory requirements for application in devices. In this section the conductivity of mixed organic carbonate will be discussed. As shown in previous chapter, according to the Walden rule, the conductivity of an electrolyte is inversely proportional to its viscosity. Therefore it

will be interesting to develop a multi-blend electrolytes with solvents with different viscosities. The mixture of cyclic and linear carbonate solvents has been studied. Figure I.3.4. shows the conductivity of mixed PC-DMC-based electrolyte for various salt concentrations in a wide temperature range (-40 – 50°C).

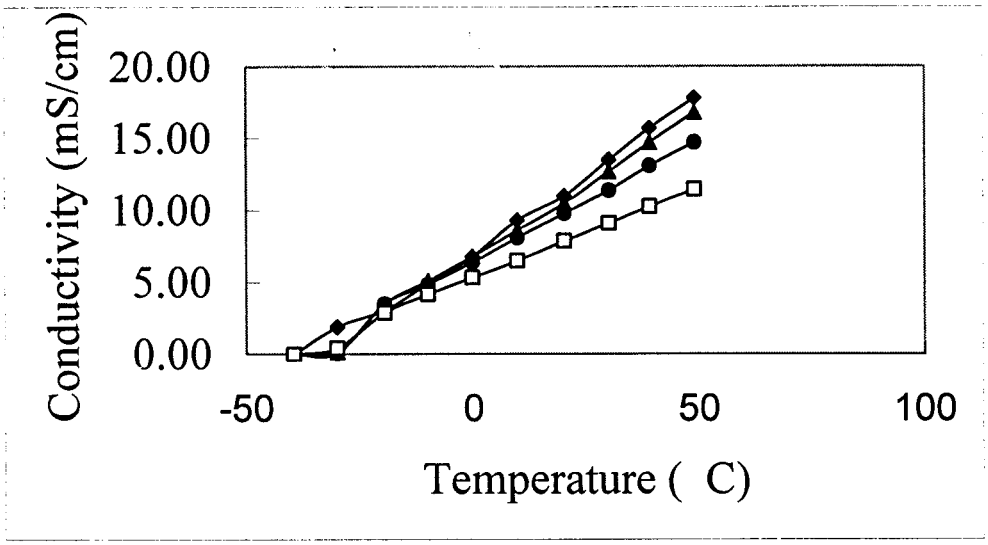

Figure I.3.4: Conductivity of Ethylene carbonate – dimethyl carbonate (EC-DMC) containing, (♦) 1M, (▲) 0.8M, (●) 0.6M, and (□) 0.4M $LiPF_6$.

It is remarkable that the conductivity of this mixture is very different than the single solvent electrolyte. The conductivity of DMC–$LiPF_6$ has very poor conductivity below –10°C. The conductivity of DEC-$LiPF_6$ is very negligible below 30°C, as DEC melts above 39^0C. However, the mixed solvent is fluid down to –30°C, and has significant conductivity from –30 to 50°C.

The conductivity of EC-EMC containing various amounts $LiPF_6$ from –40 to 50°C is shown in Figure I. 3.5. Again, high ionic conductivity was observed at

temperatures well below the melting point of the EC solvent. This mutual interaction of solvents in mixed electrolytes has opened a new area in search of electrolyte with unique properties for low temperature electrochemistry.

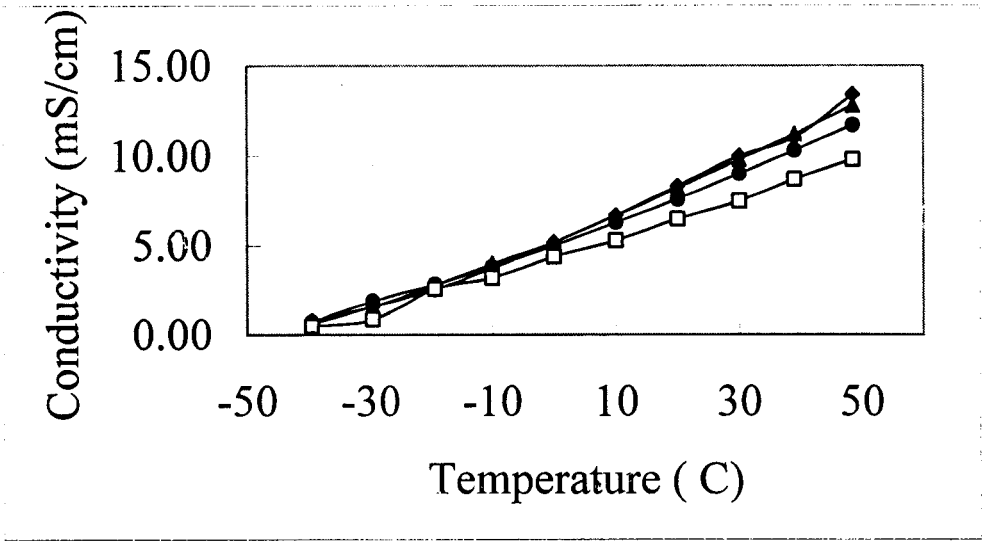

Figure I.3.5: Conductivity of ethylene carbonate – methyl ethyl carbonate (EC-MEC) containing, (♦) 1M, (▲) 0.8M, (●) 0.6M, and (□) 0.4M $LiPF_6$.

The most striking feature of the EC-MEC mixed electrolyte is that its conductivity does not change significantly for 1M, 0.8M, and 0.6M $LiPF_6$ salt concentrations, even at high temperatures. Using this remarkable electrolyte the cost of salt can be reduced by 40%. The other remarkable property of this electrolyte is that the EC with melting point of 39 °C does not phase separate at temperatures significantly below its melting point.

I.3.4.3. Conductivity of ternary solvents – $LiPF_6$ electrolytes versus concentrations and temperatures

In order to optimize the performance of the electrolyte in lithium batteries, several electrolytes with a ternary solvent mixture have been studied. The conductivity of PC-EC-DME containing 1M, 0.8M, 0.6M, and 0.4M of $LiPF_6$ as a function of temperature is

shown in Fig.I.3.6. Several interesting observations are worth mentioning. First the conductivity of salts with 1M, 0.8M and 0.6M of $LiPF_6$ are almost the same over the entire temperature range of –40 to 50°C. Second, the overall conductivity of the ternary solvent is higher than that of the single and binary solvent electrolytes. Third, there is no effect of salt precipitation and phase separation of EC (with melting point of 39°C). The conductivity for 0.4M solution is markedly lower than the 0.6-1M solutions. This ternary solvent is suitable for an advanced lithium battery, because it provides sufficient conductivity at low temperatures. It also contains the ethylene carbonate, which selectively solvate the lithium ion, and its decomposition over the lithiated graphite anode provides a good protective SEI layer. The nature of the SEI film formed in this electrolyte will be discussed in Chapter 4. Further, the electrolyte containing sufficient EC concentration can be used with a graphite anode, because this solvent does not co-intercalate between the graphite layers. The ternary solvents can be tailored to reduce the amount of lithium salt used in lithium batteries.

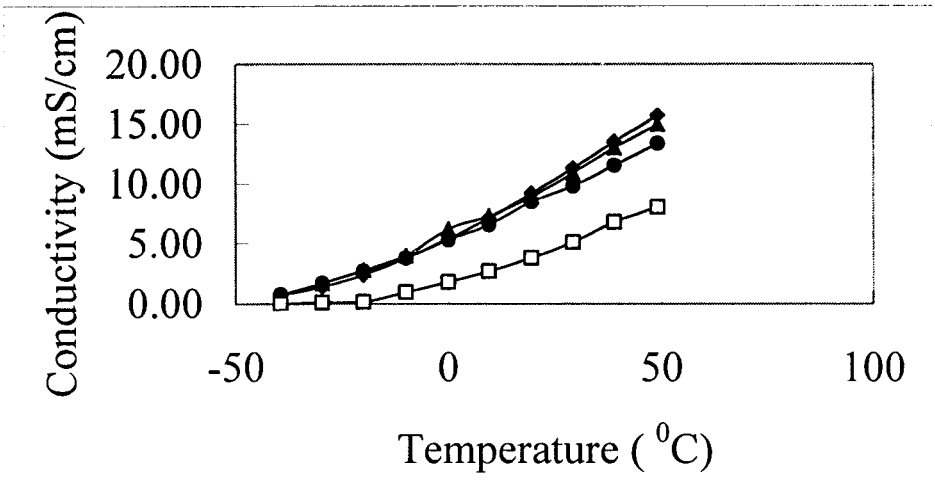

Figure I.3.6: Conductivity of propylene carbonate - ethylene carbonate – dimethyl carbonate (PC-EC-DMC) containing, (♦) 1M, (▲) 0.8M, (●) 0.6M, and (□) 0.4M $LiPF_6$.

The conductivity of multi-blend solvents PC-EC-DEC containing 1M, 0.8M, 0.6M, and 0.4M $LiPF_6$ as a function of temperature is shown in Fig I.3.7. The conductivity of these electrolytes is not as high as in the case of PC-EC-DMC. However, similar behavior is observed, namely the conductivity of 1M, 0.8M, and 0.6M solutions are very close, and for a practical lithium battery, electrolytes with low salt concentration can be used. There is no sign of salt precipitation and EC phase separation from this solution.

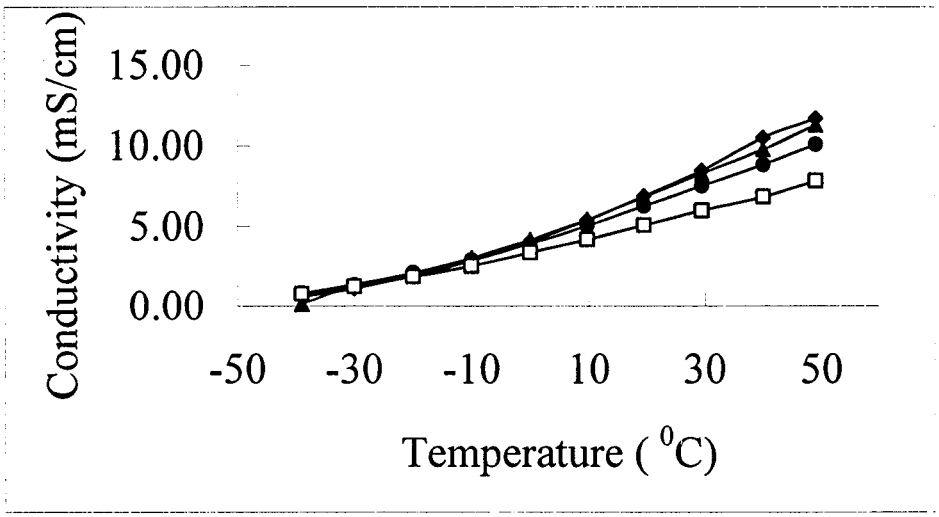

Figure I.3.7: Conductivity of propylene carbonate - ethylene carbonate – diethyl carbonate (PC-EC-DEC) containing, (♦) 1M, (▲) 0.8M, (●) 0.6M, and (□) 0.4M $LiPF_6$.

The conductivity of multicomponent electrolyte with PC-EC-EMC containing 1M, 0.8M, 0.6M, 0.4M of $LiPF_6$ is shown in Figure I.3.8. The conductivity of this series of electrolytes containing different amounts of salt concentrations are very similar over a

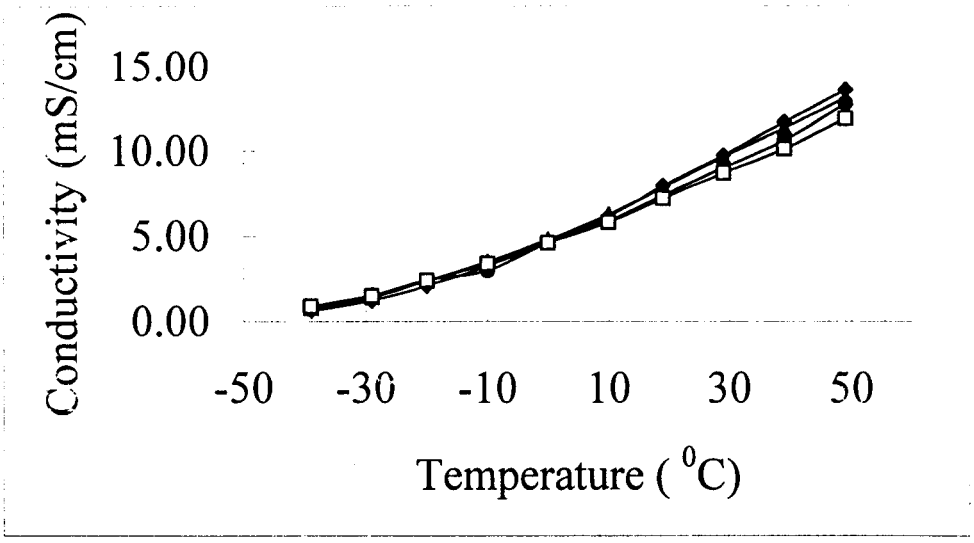

Figure I.3.8: Conductivity of propylene carbonate - ethylene carbonate – diethyl carbonate (PC-EC-DEC) containing, (♦) 1M, (▲) 0.8M, (●) 0.6M, and (□) 0.4M $LiPF_6$.

a wide range of temperatures. In general, when linear carbonates, particularly the asymmetric carbonates, are added to the cyclic carbonate, a conductivity enhancement is obtained. In addition the conductivity values for electrolytes with salt concentrations in the range of 1M to 0.6M are very similar.

The electrolytes with ternary solvent mixtures are the electrolytes of choice for a lithium battery. The overall properties of the electrolyte can be tuned to match the application by blending the solvent. The multi-blend solvent also provides the opportunity to use less salt and reduce the overall cost of the lithium battery. In most commercial cells, electrolytes with 1M $LiPF_6$ are still in use. This high salt concentration is even detrimental to the performance of the cells at low temperatures (-30-40°C), due to the possibility of salt precipitation.

I.3.5. The Electrochemical Stability of Organic Electrolytes

The electrochemical stability of nonaqueous electrolytes is crucial for the efficient charge-discharge cycles of lithium batteries. The electrolyte must be electrochemically stable up to the high voltage cut-off (the highest voltage at which cell is allowed to operate) of the cell, and stable down to the lowest voltage cut-off of the cell. In general, lithium batteries have wide cut-off voltages exceeding 4 volts. The electrochemical stability of various organic solvents has been tested on microelectrodes. The oxidation potential of solvents are measured using linear sweep voltammetry at low sweep rates (1-10 mV/sec).

The solvent stability tests were performed in electrolytes containing 1M and 0.8M $LiPF_6$. The electrolyte oxidation is measured on the surface of a Pt microelectrode. The reference and counter electrodes were metallic lithium. The electrolyte was stored over the molecular sieve for at least 48 hours before a stability test to remove residual moisture. The solvents were purified by distillation. The $LiPF_6$ was purified from excess HF by vacuum treatment at 70°C. The onset of electrolyte oxidation on the surface of Pt microelectrode is reported in Table I.3.6.

Table I.3.6: Oxidation potentials of organic solvents used for lithium battery applications [79].

Electrolyte solvent	Oxidation potential (V)
Propylene carbonate (cyclic carbonate)	4.3
Ethylene carbonate (cyclic carbonate)	5.2
Dimethyl carbonate (linear carbonate)	5.1
Diethyl carbonate (linear carbonate)	5.2
Methyl ethyl carbonate (linear carbonate)	5.2
Gama-butyrolactone	5.2
Diethoxyethane (DEE)	4.5
Tetrhydrofuran	4.1
2-methyltetrahydrofuran	4.3
1,3 dooxolane	4.2
Acetonitrile	3.8

Figure. I.3.9. shows the various electrochemical reactions that may take place on the surface of platinum microelectrode during a voltage scan from the cathodic to anodic regions.

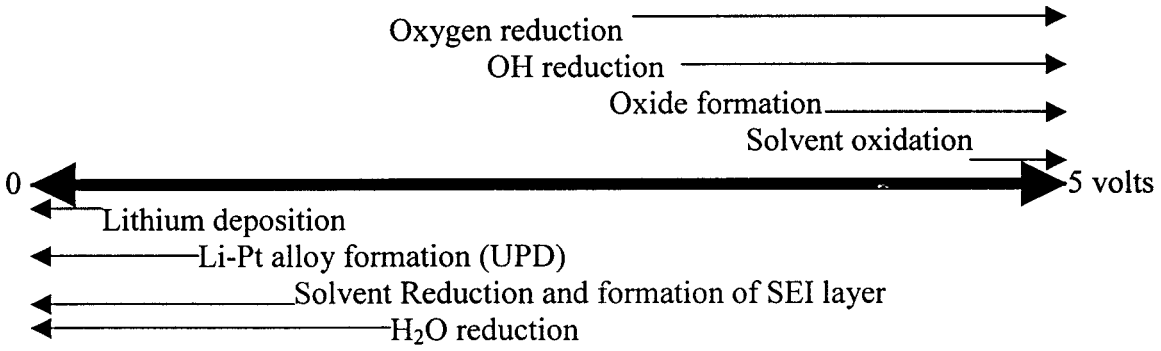

Figure. I.3.9. Schematic of various electrochemical reactions and their voltage ranges.

Chapter 4

SPECTROSCOPY OF NONAQUEOUS ELECTROLYTES

I.4.1. Spectroscopy of Non-aqueous Electrolytes

I.4.1.1. Introduction:

Vibrational spectroscopy has a unique sensitivity and selectivity for analysis of ion-association and ion-solvent interactions in electrolytes. Infrared spectroscopy provides qualitative and quantitative analysis of ion solvation process and is capable of identifying selective (or preferred) solvation of ions when mixed solvents are used in the make-up of the electrolyte. High-speed Fourier transform infrared (FTIR) spectrometers have been used routinely for molecular identification, quantification, and process control of organic and inorganic compounds [80-84].

The Fourier transform infrared instruments usually work on the principal of the Michelson interferometer. The FTIR optic bench has been shown in Chapter 2, Figure.I.2.4). To obtain a low noise FTIR spectrum, it requires a constant speed of moving mirror over a long range (over 10 cm). The exact position of mirror at any instant must be known. The interferograms are collected at precisely spaced retardation intervals and averaged with respect to the zero point retardation. For mid-IR spectroscopy (500-4000 cm^{-1}) the IR radiation is generated from a Globar source. The Globar source is an inert solid, usually a tungsten carbide (WC) rod, 50 mm in length and 5 mm in diameter, designed in a helical shape and heated electrically to a temperature 1500 – 2200 K, to produce a continuous radiation with strong energy output in the mid-IR region. The intensity of the Globar source drops to about 1% in the far-IR region (500 - 10 cm^{-1}) and in near-IR region above 10,000 cm^{-1} [79]. The FTIR instrument for mid-IR spectroscopy is equipped with a KBr beam splitter and a liquid nitrogen cooled MCT detector.

In this work, the Attenuated Total Reflection (ATR) spectroscopy is used for analysis of electrolytes. In the past, ATR was used for obtaining infrared spectra of samples that are difficult to deal with, such as solids with limited solubility, films, pastes, adhesives, and compressed powders. However, we have found that the attenuated total reflection method provides the most reproducible and reliable IR spectra for liquid electrolytes as compared with other thin film methods.

The aim of this work is to understand the degree of ion- solvent interaction and the importance of selective solvation of Li^+ in mixed carbonate-based electrolyte. Nonaqueous electrolytes containing blend of mixed organic carbonates are used in most advanced lithium batteries. The development of new electrolyte for lithium batteries is intensively under investigation [68,85-94]. During the past decades, the design of electrolyte for lithium batteries has been mostly based on trial-and-error with some chemical intuitions guided by the physical properties of solvents (e.g. dielectric constant, dipole moment, viscosity). Recently, theoretical calculations based on molecular orbital (MO) simulations have been applied to understand the ion-solvent interactions [95].

Vibrational spectroscopy has proven to be most useful in probing the salt-solvent interactions in electrolytic systems [15,70,71,86,96,97]. The vibrational spectrum provides frequencies, intensities, and band properties (band shape) that can be used to identify molecular species, solvent-solvent and ion-solvent interactions [92]. Such studies could help to identify factors that influence the chemical and physical properties

of an electrolyte. For example Kakihana et al [91] have shown that backbone flexibility of polymeric electrolytes, such as skeletal motion in polyethylene oxide (PEO) and polypropylene oxide (PPO) doped with salt, has a great effect on the conductivity of the complex ploy-electrolytes. Chen et al. [90] have indicated that addition of an ion-chelating agent to the polymeric electrolytes to reduce ion-pairing (as detected using Raman spectroscopy) will markedly increase the ionic conductivity of polyelectrolyte. McLin et al. [93] have correlated the ion- associations in polyelectrolytes with the viscosity and conductivity values.

Characteristic vibrational frequencies such as the C=O stretch, the C-H wag, and the ring deformation modes in cyclic carbonate based electrolytes are sensitive to the addition of salt. These vibrational modes can be monitored to study the degree of ion-solvent interactions. For example, the IR absorption around 708-712 cm^{-1} has been assigned to the symmetric ring-breathing mode for cyclic propylene carbonate [94]. This mode of vibration is very sensitive when ion-solvent complexes are formed.

Characteristic group frequencies of cyclic and linear organic carbonates are given in the region of; ring deformation mode (600-800 cm^{-1}), C-H wag and C-O stretch modes (800-900 cm^{-1}), C-H bending (1100-1300 cm^{-1}), and the C=O stretching vibrations (1700 – 1850 cm^{-1}), as given in table I.4.1.

Practical organic electrolytes are usually falling in the category of concentrated electrolytes and extensive ion-associations such as ion-pairing, ion multiples, and aggregates may exist when salt concentrations exceed 0.1M. Theoretical calculation of

vibrational spectra, infrared and Raman intensities are reported for various configurations of ion-pairs [91,92]. In the case of $LiClO_4$ dissolved in propylene carbonate, the results indicate that the tridentate geometry is the most stable configuration for the C_{3v} model [84]. It has been shown that the vibrational spectrum of the tridentate ion-pair have two IR active vibrational modes at 877 cm^{-1} and 879 cm^{-1}. The ion association for the $LiPF_6$ in dimethyl carbonate also has been studied. The IR band around 844 cm^{-1} has been assigned to the vibration of PF_6^-, and the splitting of the band at concentrations higher than 0.2M has been interpreted for the presence of ion-pairs. The IR peak at 836 cm^{-1} has been assigned to the PF_6^- vibration. In this chapter the interaction of organic carbonate solvents with $LiPF_6$ and the influence of mixed solvent on ion-association will be discussed.

I.4.2. Experimental Section

I.4.2.1. Materials:

Solutions containing propylene carbonate and lithium hexafluorophosphate were prepared inside a dry box filled with pure Ar (99.999%). The oxygen and moisture contents were less than 1 ppm in the dry box. Propylene carbonate (PC), ethylene carbonate (EC), diethyl carbonate (DEC) and dimethyl carbonate (DMC) with high purity were obtained from Fluka Chemicals. $LiPF_6$ was obtained from Hashimoto, Japan. It is important to note that $LiPF_6$ is very moisture sensitive and packaging of this salt requires special attention to prevent increasing the level of HF in the salt. After opening the salt bottle, it should be stored in the dry box. It is also very important to evacuate the $LiPF_6$ at moderate temperatures (40-70 °C) to remove the adsorbed HF that comes from synthesis

of $LiPF_6$. Commercial $LiPF_6$ usually has adsorbed HF. The thermal analysis of commercial $LiPF_6$ has shown that adsorbed HF can be removed by vacuum and heating to about 80 °C. The amount of HF can be minimized by vacuum drying according to the following equation.

$$LiPF_6\text{-}HF \text{ --------Heat/vac----------} \rightarrow LiPF_6 + HF \quad (46 \text{ Kcal/mole})$$

Further heating of the sample to 200 °C may decompose the salt to PF_5 and HF according to the following reaction.

$$LiPF_6 \text{ ----------heat ----------} \rightarrow PF_5 + LiF \quad (190 \text{ Kcal/mole})$$

The drying process of the $LiPF_6$ at 70 °C under vacuum reduces the HF level to less than 150 ppm.

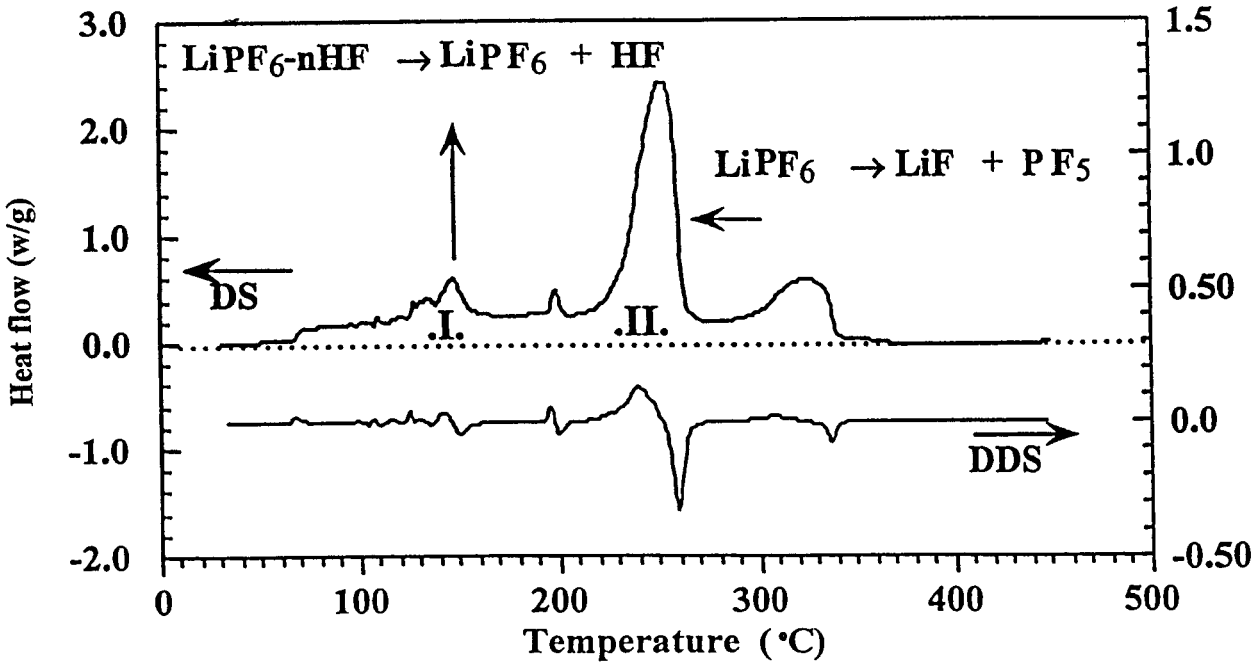

Figure I.4.1: Differential Scanning Calorimetry (DSC) of $LiPF_6$.

Electrolyte solutions were formed by the addition of ultra pure $LiPF_6$ to various mixtures of carbonate solvents. Both cyclic carbonates, such as ethylene carbonate (EC), propylene carbonate (PC), and linear carbonates, such as dimethyl carbonate (DMC), diethyl carbonate (DEC), and the asymmetric methyl ethyl carbonates MEC) were used. The electrolyte preparation was performed in a Vacuum Atmosphere dry box filled with 99.999% Argon. The dry box is equipped with Nitrain and catalyst recirculation units. All electrolytes were made in a dry box. The atmosphere of the box was continuously circulated over Cu shaving catalyst to remove residual oxygen and moisture, and over titanium sponge (Nitrain) held at 700 °C to remove residual nitrogen. To double-check the purity of the box, a 40 W tungsten light bulb was cracked and installed in the box. Each lamp usually last over two months before burning out. (Care should be taken when cracking the light bulb; a sharp triangular file or a diamond-cutting saw can be used). Monitoring the life of a cracked light bulb inside a dry box is a simple method to check the purity of the dry box atmosphere. However, the light-bulb technique may not work well when there are reactive solvent vapors or other reactive chemicals with high vapor pressure in the dry box. In this case using calibrated oxygen and moisture sensors are most suitable.

A Fourier transform infrared spectrometer (Bruker model 113), with a Globar source, equipped with a KBr beam splitter for Mid-IR spectroscopy, and a liquid nitrogen cooled MCT (mercury cadmium telluride) detector were used.

The ATR cell used in this work was from Spectratech, (circle liquid analyzer model 0005-011) with a ZnSe crystal rod. The ATR cell consists of an IR transparent rod, 83mm long and 6.35mm in diameter. Both ends of the rod are cut in 45° cone shapes. A set of mirrors shown in Figure. (I.4.2) focuses the IR incident beam perpendicularly to the 45^0 cut cone shape of the ZnSe rod. The cone shape ends provide a perpendicular entry and exit for the IR beam. Another, similar, mirror assembly collects the beam after exiting the rod and focuses the exiting beam toward the IR detector. The ATR rod is located in the center of a cylindrical cavity, which contains the electrolyte. The electrolyte is in intimate contact with the ATR rod. The ATR rod in this case is a ZnSe rod, which provides over 25% transparency for the IR beam. A schematic of the ATR cylindrical cell used in this work is shown in Chapter 2, Figure (I.2.6).

The beam penetration into the electrolyte zone allows studying the vibrational spectra of the electrolyte near the surface of ATR element shown in Figure I.4.2. The cylindrical cell used in this work provides very accurate and reproducible spectra for liquid samples. The penetration of IR beam into the electrolyte zone depends on the ratio of the refractive index of the ATR element to that of the electrolyte solution. In principal the electric field of the evanescent wave produced on total reflection at the ATR rod-electrolyte interface decays exponentially according to following equations [94].

$$E = E_0 \exp\left(\frac{z}{d_p}\right)^{1/2} \qquad \text{(I.4.1)}$$

And the penetration depth (d_p) at which the intensity drops to 1/e is expressed as;

$$d_p = \frac{\lambda}{2\pi n_1}\left[\sin^2\theta - \frac{n_2}{n_1}\right]^{-1/2} \qquad \text{(I.4.2)}$$

where the λ is the wavelength of the radiation, n_1 is the refractive index of the ATR element and n_2 is the refractive index of the solution, θ is the angle of internal reflection, and in this case is 45°. The absorbance value using ATR technique is given according to the following equation [94].

$$A = \frac{n_2}{n_1}\frac{\alpha}{\cos\theta}\int_0^z E\, d_p \qquad \text{(I.4.3)}$$

Where the α is the absorption coefficient per unit thickness that would be obtained for the band in the transmittance spectrum.

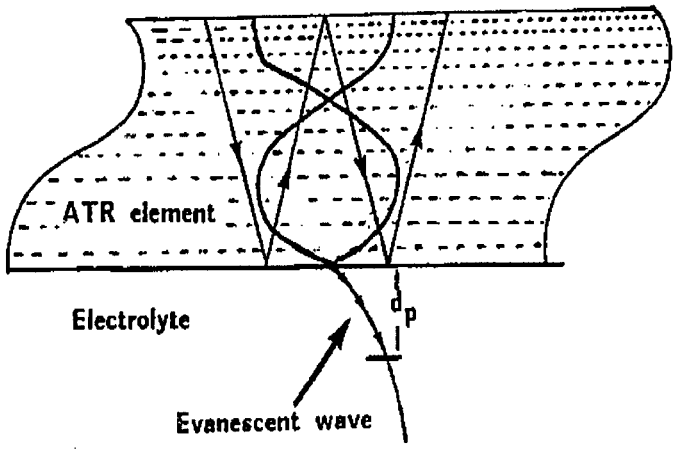

Figure I.4.2: Penetration of IR beam at the ATR/electrolyte interface [23].

The IR spectrum of $LiPF_6$ was collected using KBr pellet technique. The KBr powder was dried at 120°C under vacuum and transferred in the dry box for use. In order to prevent exposure to air, a sandwich type pellet was made and that the well-ground

$LiPF_6$ powder was placed in the middle of two thin KBr pellets and pressed again to form a single pellet. The spectrum was collected at $4cm^{-1}$ resolution, for 256 scans and in the range of 500-$4000cm^{-1}$. The reference was taken from a thicker KBr pellet that has similar output to that of the sample pellet. Using a sample and reference with similar output provides IR spectra with a flat background. No background correction was then needed when the output of sample and reference were controlled to similar values.

The basic requirements for an electrolyte for electrochemical devices are discussed in detail in Chapter 3. They include high ionic conductivity, low melting and high boiling points, as well as chemical and electrochemical stability. The composition of nonaqueous electrolyte solutions for secondary lithium batteries plays an important role in determining cycle life, cell performance, operating temperature range, and storage temperature. There are several reviews concerning the conductivity and properties of nonaqueous electrolyte containing single carbonate solvent [65-68].

The water content of solvents and electrolytes were checked by the Karl Fischer method. The initial water content was in the order of 1000 ppm. The commercial cyclic carbonates, PC and EC had more than 1000 ppm water. The linear carbonates, DMC, DEC and MEC had less than 1000ppm water contamination. However, after storing the solvents and electrolyte over a molecular sieve for 24 hours the water content was reduced to less than 30 ppm.

The following solutions were made of single solvent or multi-blend of solvents.

1. Pure solvents

Dimethyl carbonate (DMC), diethyl carbonate (DEC), ethylene carbonate (EC), ethylene carbonate (EC) and propylene carbonate (PC).

2. Single solvent electrolyte

DEC + 1MLiPF$_6$, DMC + 1MliPF$_6$, EC + 1MliPF$_6$ and PC + 1MliPF$_6$,

3. Binary electrolytes: LiPF$_6$ in (1:1 mole) solvents

EC + DEC(1:1) + 1MliPF$_6$, EC + PC(1:1) + 1MliPF$_6$, and EC + DMC(1:1) + 1MliPF$_6$.

4. Binary electrolytes with different solvent ratios

EC + DMC(1:4) + 1MliPF$_6$, EC + DMC(1:3) + 1MliPF$_6$, EC + DMC(1:2) + 1MliPF$_6$, EC + DMC(2:1) + 1MliPF$_6$, EC + DMC(3:1) + 1MliPF$_6$, EC + DMC(4:1) + 1MliPF$_6$.

5. Ternary electrolytes LiPF$_6$ in (1/3:1/3:1/3 mole) solvents

EC-DMC-PC (1/3:1/3:1/3) + 1M LiPF$_6$, EC-DEC-PC (1/3:1/3:1/3) LiPF$_6$

For salt, LiPF$_6$ has been used in this work, which is the common salt in most commercial lithium batteries. The LiPF$_6$ is stable up to about 5.0 V vs. Li electrode [95,98-102]. The PF6$^-$ anion is an interesting probe for IR spectroscopy to monitor the dynamic of lithium salt in electrolyte. Therefore IR spectroscopy of electrolyte containing LiPF$_6$ was performed. The PF$_6^-$ anion has a sharp peak around 850 cm^{-1}.

I.4.3 Results and Discussions

Electrolytes were made from cyclic and linear organic carbonates containing the lithium salt. The cyclic carbonates have large dielectric constants (60 to 90) and high viscosity (1.5-2 centipoise). The high dielectric constant has the advantage of dissolving more salt, but the high viscosity is a disadvantage as it retards the ion transport and lowers the conductivity. Therefore, a mixture of cyclic and linear carbonate solvents is used. The linear carbonates have low dielectric constants (2 to 7) and very low viscosity (0.4 to 0.8 centipoise). Addition of the linear carbonate to the cyclic carbonate modifies the viscosity according to the rule of mixtures discussed in Chapter 3. In this chapter, the significance of solvent-solvent interactions and ion-solvent interactions will be discussed. The IR spectra of pure solvents without any salt were collected as a reference. Figure I.4.3 show the IR spectra of ethylene carbonate, propylene carbonate, dimethyl carbonate and diethyl carbonate. The IR peaks are marked for comparison. The IR peaks around 1700-1900 cm^{-1} correspond to the C=O stretching vibration of the organic carbonate solvents. The IR spectra are given for each organic carbonate solvents for ease of comparison. The cyclic carbonates are shown in Figure I.4.3 and Figure I.4.4, and the IR spectra of linear carbonates are shown in Figure I.4.5 and Figure I.4.6.

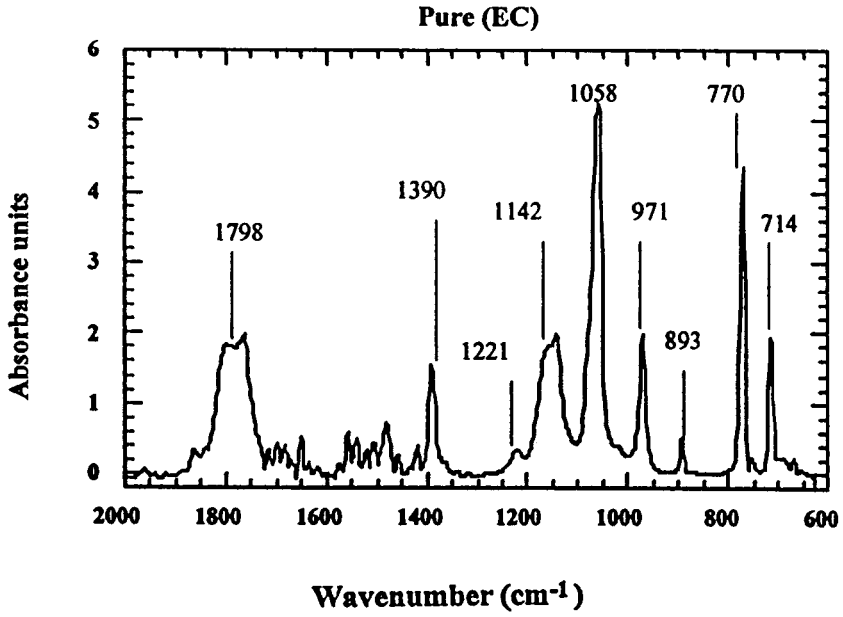

Figure I.4.3: FTIR spectrum of pure ethylene carbonate, EC.

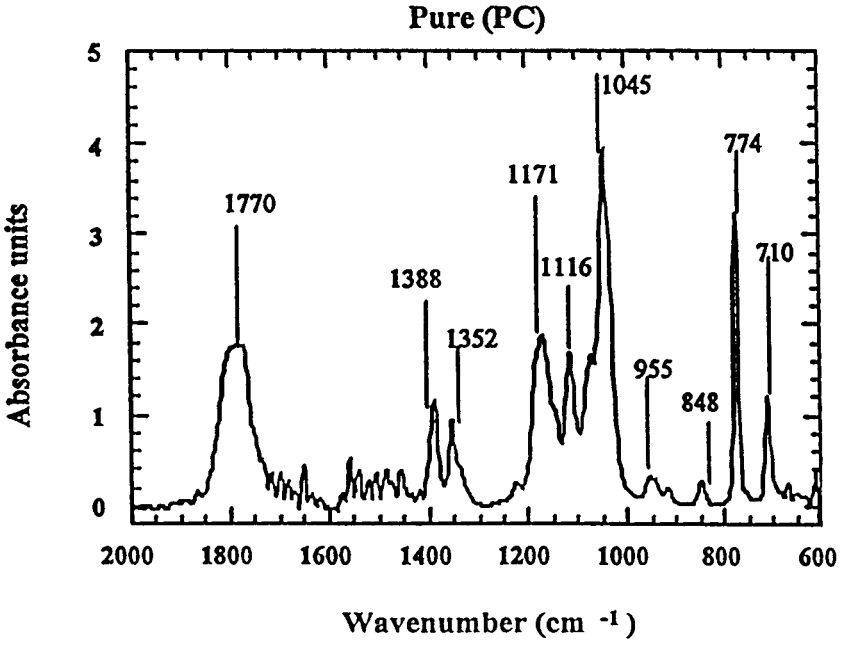

Figure I.4.4: FTIR spectrum of propylene carbonate, PC.

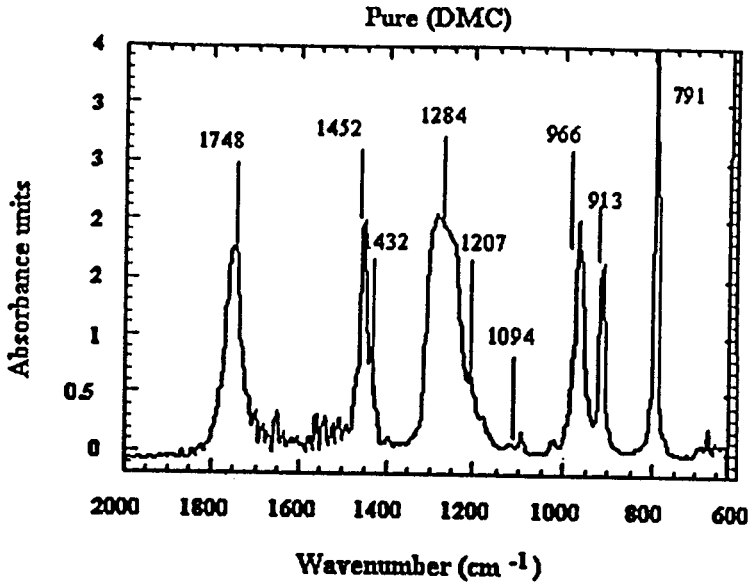

Figure I.4.5: FTIR spectrum of dimethyl carbonate, DMC.

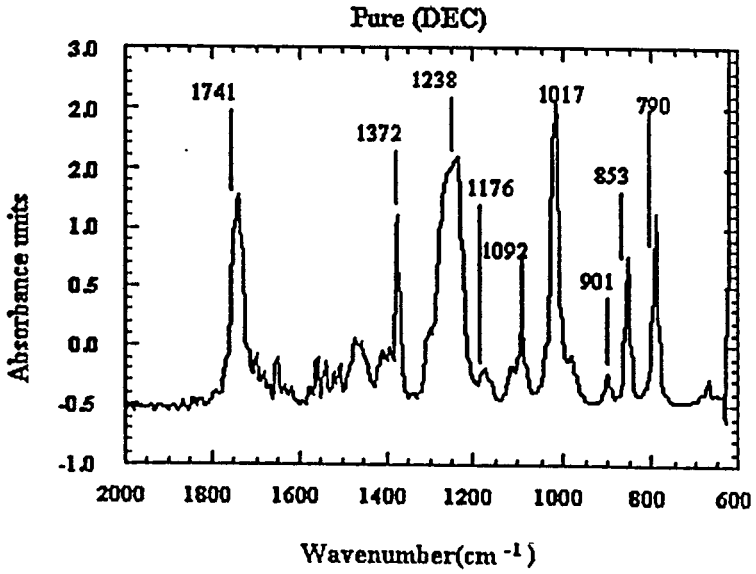

Figure I.4.6: FTIR spectrum of diethyl carbonate, DEC.

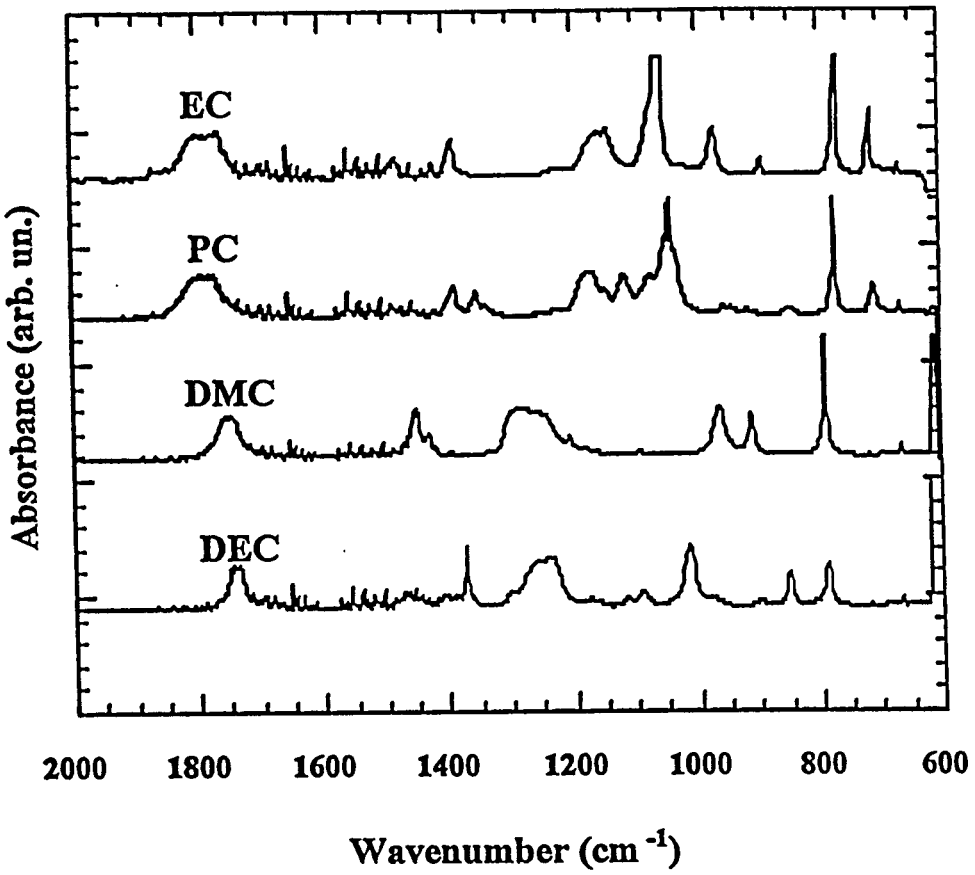

Figure I.4.7: IR spectra of pure solvents (EC, PC, DMC, DEC)

The observed vibrational frequency modes for cyclic and linear carbonates are listed in Table I.4.1. The IR absorption for the C=O stretching modes for both cyclic and linear carbonates are strong. However, this absorption peak is very sharp for the linear carbonates, but it is broadened significantly for the cyclic carbonate.

Table I.4.1: Characteristic Infrared frequency of PC, EC, DMC, DEC

PC	EC	DMC	DEC	Assignment
711 s	714s	791vs	790 vs	symmetric ring deformation
774 vs	770vs			ring deformation
848 m	893w	914s	854 s	$C_7 - H + O_6 - C_5 - C_4$ bending
1045 vs	1059vs	967s	1017vs	$C_5 - H$ twist + $C_4 - H$ bending
1116 vs		1094	1092s	$C_7 - H$ wag + $C_4 - H$ bending
1148 vs	1142s	1207w	1176w	$C_5 - C_4 + C_2 - O_6 + C_2 - O_3$ stretch
1172 vs	1170s	1284s	1176w	$O_6 - C_5$ stretch + $C_7 - H$ wag
1337 sh	1221w		1238vs	$C_7 - H$ bending
1353 vs			1299w	$C_7 - H$ bending
1386 s	1390s	1432w	1372 s	$C_5 - H$ wag + $C_7 - H$ bending
1485 w	1481w	1452s	1468s	$C_7 - H$ umbrella
1785 s	1780s	1748 s	1741vs	$C_2 = O_1$ stretching

s = strong, m = medium, w = weak, v = very, sh = shoulder,

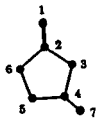

The peak broadening for the cyclic carbonate is in part due to the higher viscosity of the cyclic carbonate as compared to that of the linear carbonate. Although the viscosity of the cyclic carbonates are higher than the linear carbonates, the C=O stretching vibrations for the cyclic carbonate are up-shifted to around 1780 cm^{-1} as compared with that of linear carbonates with C=O stretching vibrations around 1740 cm^{-1}. The IR spectra have shown a stronger interaction of C=O with Li^+ for the cyclic carbonate as compared with that of the linear carbonates. This stronger interaction has significant impact on selective solvation of Li^+ with the cyclic carbonate, and hence marked influence on the performance of the electrolyte in the lithium cell, as it will be discussed in Chapter 5. In addition, the stronger interaction of Li^+ with the C=O of the cyclic carbonate may cause a weaker interaction of Li^+ with the C-O part of the ring. The interaction of Li^+ with the C-O of the linear carbonate is stronger than that of the cyclic carbonate. It can be concluded that a more homogeneous charge distribution exists in

linear carbonate favoring bidendate interaction with Li^+, and a more favorable monodendate interaction of Li^+ with the cyclic carbonate as compared with the same interaction in linear carbonate.

Figure I.4.8 shows the effect of $LiPF_6$ and mixed solvent on the vibrational spectra of ethylene carbonate. A strong IR band at 834 cm^{-1} appears when $LiPF_6$ was added to the EC solvent which is a characteristic vibration band of PF_6^-. Addition of

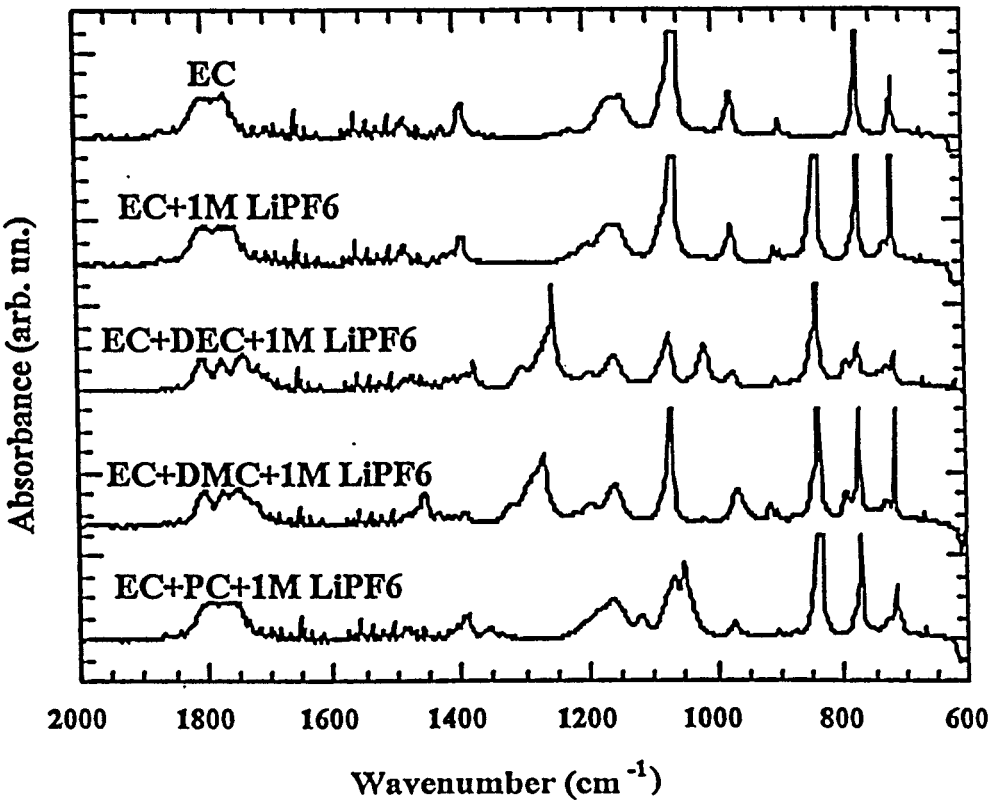

Figure I.4.8: Effect of $LiPF_6$ and solvents on vibrational spectrum of ethylene carbonate.

$LiPF_6$ to the ethylene carbonate also splits the EC ring deformation band. The strong ring deformation band of EC molecule at 714 cm^{-1} splits and a new but weaker band appears at 729 cm^{-1}. The O-C-C bending mode also splits and a new down-shifted band is formed at to 894 cm^{-1}. The original O-C-C band is at 903 cm^{-1}. The new down-shifted band is assigned to the Li^{+}-EC complex as the intensity of the 894 cm^{-1} is concentration dependent. The C=O stretching vibration is also down shifted to 1760 cm^{-1}.

A surprising change in the vibrational spectra of EC-$LiPF_6$ was observed when DMC was added to this solution. A marked decrease in the intensity of the EC ring deformation mode and peak splitting were observed. This result is a clear indication that there are significant solvent-solvent interactions between the EC and DMC molecules. It is worth mentioning that the viscosity of the solution also significantly decreased when DMC was added to the EC-$LiPF_6$ solution, and solution remained liquid well below the freezing point of EC, and no phase separation has been observed for EC down to -10^{0}C. The C=O stretching vibration at 1750 cm^{-1} for DMC was down shifted to 1721 cm^{-1}. A better resolution (peak separation) for the C-H wag and C-H bending vibrations were also observed in mixed solvent electrolyte.

Addition of third solvent, DEC, to a mixture of EC-$LiPF_6$ had a similar effect as discussed above for the EC-DMC-$LiPF_6$ solution. A strong reduction of the ring deformation intensity and the splitting of most of the IR bands were noticeable. In the region of C=O stretching vibration, four well-separated peaks were observed, corresponding to the C=O stretching vibrations for free molecules, and two peaks for the

damped C=O---Li^+ complexes. The C=O---Li^+ complexes are strongly downshifted by about 20 cm^{-1}. These results indicate strong interaction of Li^+ with the C=O part of the organic carbonates. The interaction of Li^+ with the organic carbonate also has significant impact of the ring deformation mode of the cyclic carbonates, and the C-O-C vibration of the linear carbonates.

IR spectra of EC-PC-$LiPF_6$ are also shown in Figure I.4.8. Addition of PC solvent to EC-$LiPF_6$ has reduced the mixture viscosity significantly, and the electrolyte remained liquid well below the freezing point of the EC. The complex Li^+--EC and Li^+--PC have a down-shifted C=O stretching vibration as compared with that of the salt-free solvents. The ring deformation modes of EC and PC molecules are also affected when $LiPF_6$ was added to the mixed solvent. The C=O stretching and the C-O-C bending modes are very sensitive to the salt addition. When lithium salt was added to organic carbonates, in all cases, a better resolution and peak separation was observed for the C-H wag and bending vibrations.

The effect of lithium salt and addition of EC to the vibrational modes of DEC is shown in Figure I.4.9. The pure diethyl carbonate has a strong well-resolved C=O stretching vibration. This peak splits when $LiPF_6$ salt is added to the solvent.

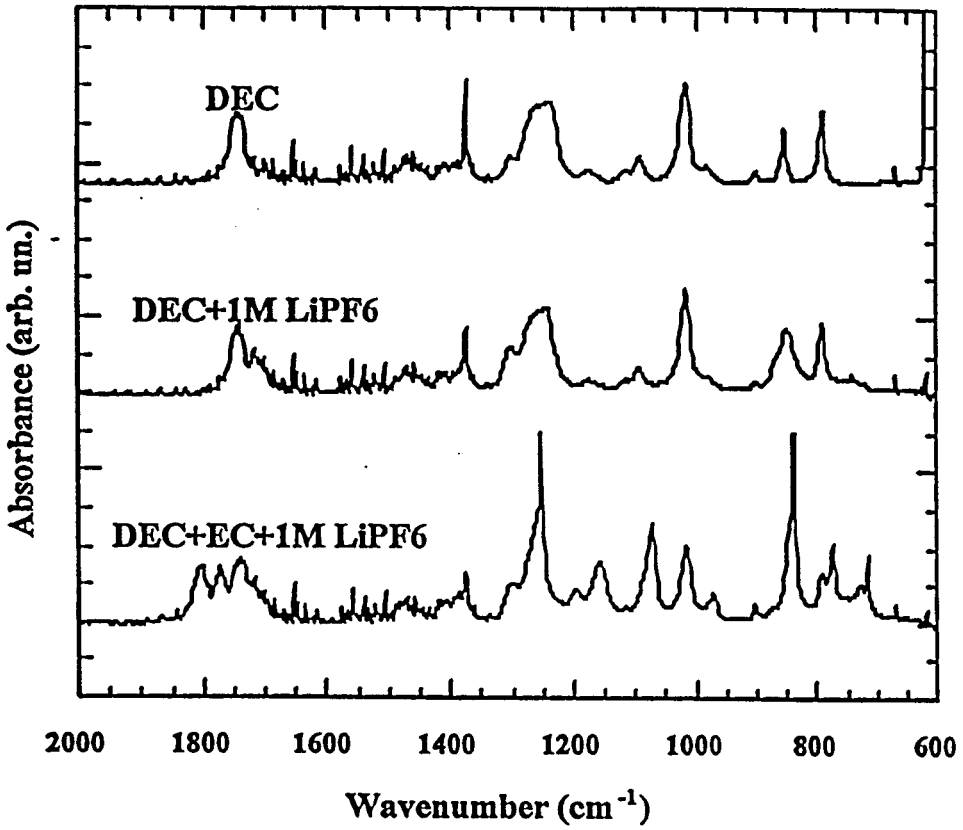

Figure I.4.9: IR spectra of pure DEC, DEC+1MLiPF$_6$, DEC+EC+1MLiPF$_6$.

The new peak is down shifted by 27 cm^{-1}. The intensity of the new peak is also sensitive to the salt concentration. This downshifted peak at 1715 cm^{-1} has been assigned to the C=O stretching vibration of Li^+--DEC complex. The C-O-C bending mode also splits when $LiPF_6$ is added to the solution, and a new peak appears at 740 cm^{-1}. This new peak is assigned to the C-O-C bending mode when interacted with Li^+. This interaction can be visualized for the formation of a bidendate complex of Li^+ with the DEC molecule, where

the Li^+ ions interact with both the oxygen of C=O and the oxygen of C-O-C. Although the C-O stretching vibration is affected by the Li^+ interaction as it was discussed in the case of DMC-$LiPF_6$, the C-O stretching vibration of DEC (853 cm^{-1}) strongly overlaps with the vibration of PF_6^- (849 cm^{-1}) and it is difficult to resolve. It is surprising to observe that C-H bending and wagging vibrations are up shifted and more resolved when Li^+ is interacted with DEC molecule. This situation was also observed for the DMC-$LiPF_6$. This can be interpreted in a way that the induction effect of Li^+ and electron withdrawing form the organic carbonate toward Li^+ makes the C-H bond free to vibrate.

The addition of cyclic carbonate, EC, to the DEC-$LiPF_6$ has a marked effect on the conductivity of the mixture as discussed in the previous chapter. It also has an interesting effect on the vibrational spectra of the DEC. The intensity of the ring deformation mode of the EC is reduced significantly and splits into two peaks at 728 and 716 cm^{-1}. It is very important to note that not only the Li^+ interact with the solvents, but there is also a strong solvent-solvent interaction between organic carbonate molecules. This phenomenon also has been observed on the change in the macroscopic properties of the mixed DEC-EC solvents. In particular, the viscosity of the mixed solvent electrolytes has been reduced. The C=O stretching vibration is also affected when mixed solvent is used. Four well resolved IR peaks (at 1804, 1773, 1739, and 1718 cm^{-1}) were observed for the C=O stretching of the DEC-EC-$LiPF_6$ solution. The two down shifted peaks (1773 and 1718 cm^{-1}) correspond to the C=O---Li^+ complexes (for EC and DEC respectively), and two peaks (1804 and 1739 cm^{-1}) for unsolvated EC and DEC molecules. It is also interesting and surprising to observe that the vibration of PF_6^- is less affected in mixed

DEC-EC mixture. This effect can be interpreted as the strong solvent-solvent interactions cause a weaker ion-solvent interaction. This less ion-solvent interactions in multi-solvent electrolytes may have beneficial effect on the conductivity, due to a weaker interaction of Li^+ with the solvent molecules. This may guide researchers to design an electrolyte with higher conductivity by using mixed solvents with strong solvent-solvent interactions.

The effect of $LiPF_6$ and additional solvent on vibrational spectra of DMC is shown in Fig. I.4.10. The dimethyl carbonate is a linear and symmetric carbonate and most often used as a viscosity reducer in nonaqueous electrolyte for lithium batteries. The Li^+ ions interact with the C=O part of the DMC and splits the C=O stretching vibration. As the C=O---Li^+ is significantly damped, the C=O stretching vibration is down shifted and a new peak at 1719 cm^{-1} is observed for the Li^+---O=C complex. The C=O stretching vibration of pure DMC is at 1750 cm^{-1}. This significant down shift (31 cm^{-1}) is a clear indication of a strong interaction of Li^+ with the C=O of the DMC molecule. A new peak also appears at 741 cm^{-1} corresponding to C-O---Li^+ vibration. The vibrational mode of PF_6^- also split in two peaks (844 and 863 cm^{-1}). As we observed in the case of DEC-EC-$LiPF_6$, with the addition of cyclic carbonate to DMC-$LiPF_6$, the vibration of PF_6^- becomes more symmetric and closer to a single peak. This can be interpreted as the mixed solvent effect. When strong solvent-solvent interaction exist a weaker ion-solvent interaction may result, particularly for a bulky anion such as PF_6^-. The ring deformation mode and the C-O vibrations of EC molecule in DMC-EC-$LiPF_6$ are also split into two peaks, 722 and 731 cm^{-1} for the ring deformation mode, and 777 and 793 cm^{-1} for the C-

O stretching modes. The peak splitting also indicates that Li^+ ions interact with the oxygen of C-O-C in the molecule, favoring the bidendate complex formation.

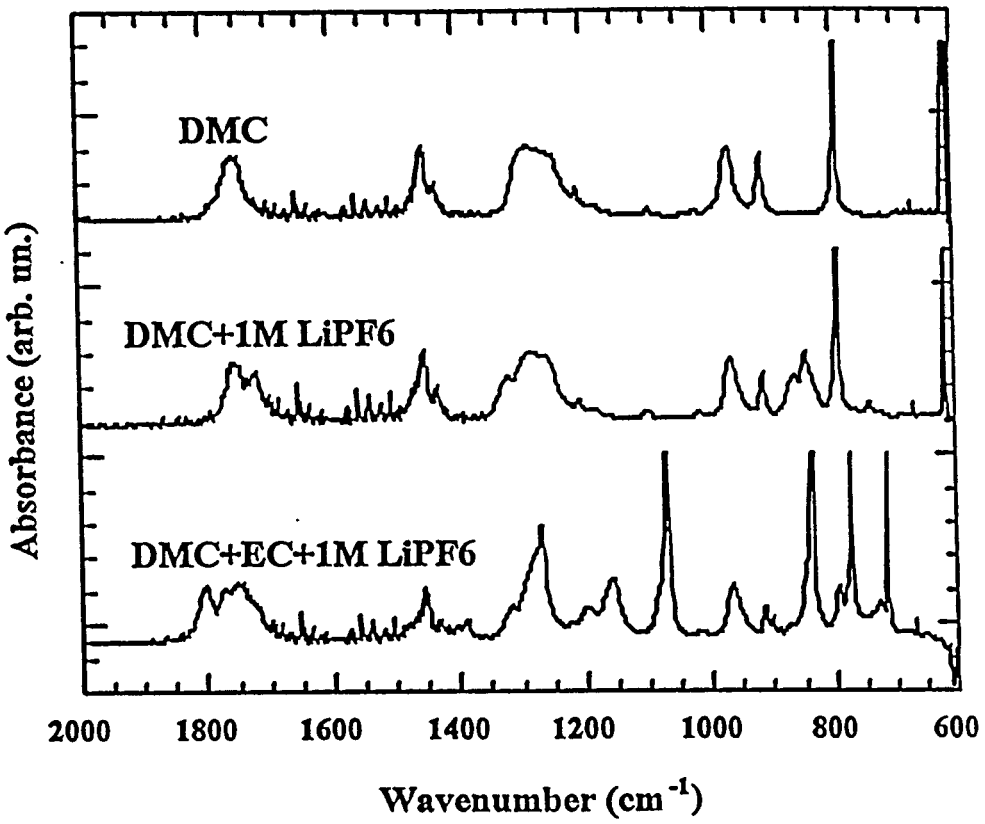

Figure I.4.10: IR spectra of (Pure DMC, DMC+1M$LiPF_6$, DMC+EC+1M$LiPF_6$)

Figure I.4.11 shows the effect of $LiPF_6$ and additional solvent to the vibrational modes of PC. Just in contrast to the linear carbonate, there is not a strong interaction of PF_6^- with the cyclic carbonate, and the vibrational peak of PF_6^- at 836 cm^{-1} remains strong with a symmetric profile. The intensity of the C=O stretching vibration is reduced due the interaction with Li^+ and formation of the C=O---Li^+ complex. The C=O stretching

vibration of the cyclic carbonate is also broadened significantly by the addition of $LiPF_6$. When EC was added to the PC-$LiPF_6$, the vibration of PF_6^- remains sharp and symmetric. However, more band broadening was observed for the C=O stretching vibration with a slight down- shift in wavenumber. The C-O-C bending mode of the EC molecule is more affected than that of the PC molecules. The overall observation indicates a stronger interaction of Li^+ with the EC molecule than with the PC.

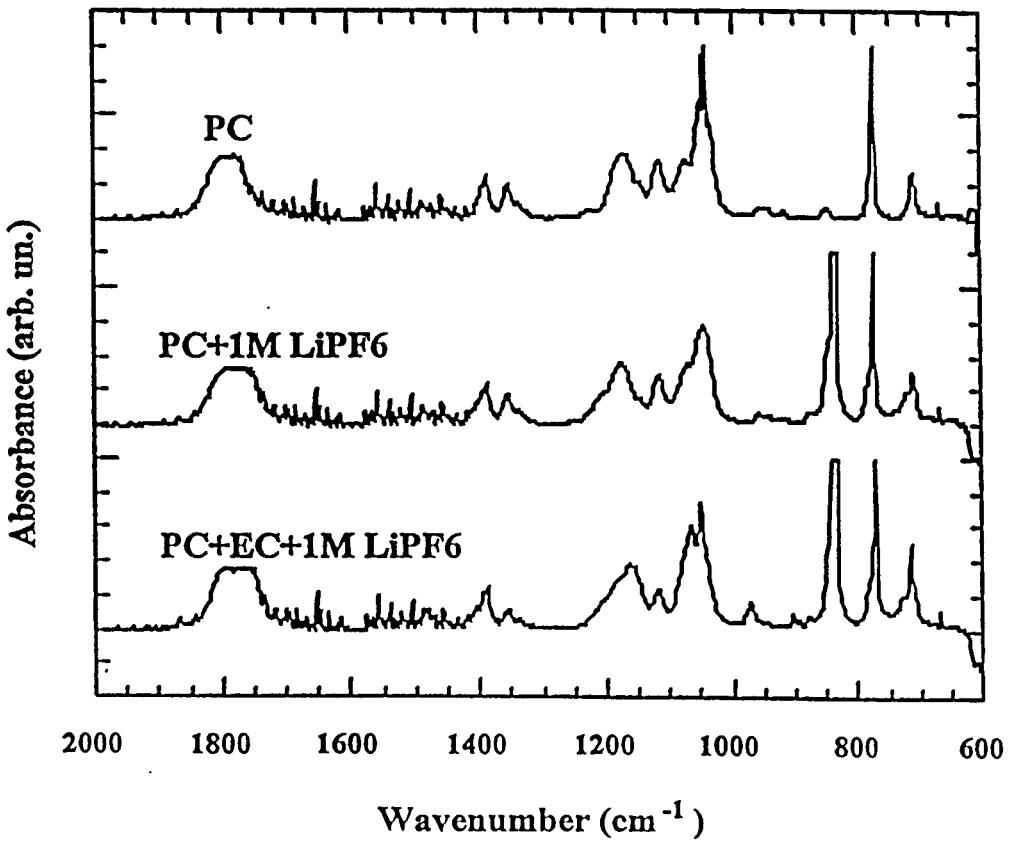

Figure I.4.11: IR spectra of (Pure PC, PC+1M$LiPF_6$, PC+EC+1M$LiPF_6$)

Figure I. 4.12 shows the IR spectra of pure $LiPF_6$, Li_2O, and Li_2CO_3. These spectra show that the $LiPF_6$ is free from common impurities (Li_2O and Li_2CO_3). The main vibration of PF_6^- around 840 cm^{-1} is similar to that observed in the electrolyte containing $LiPF_6$.

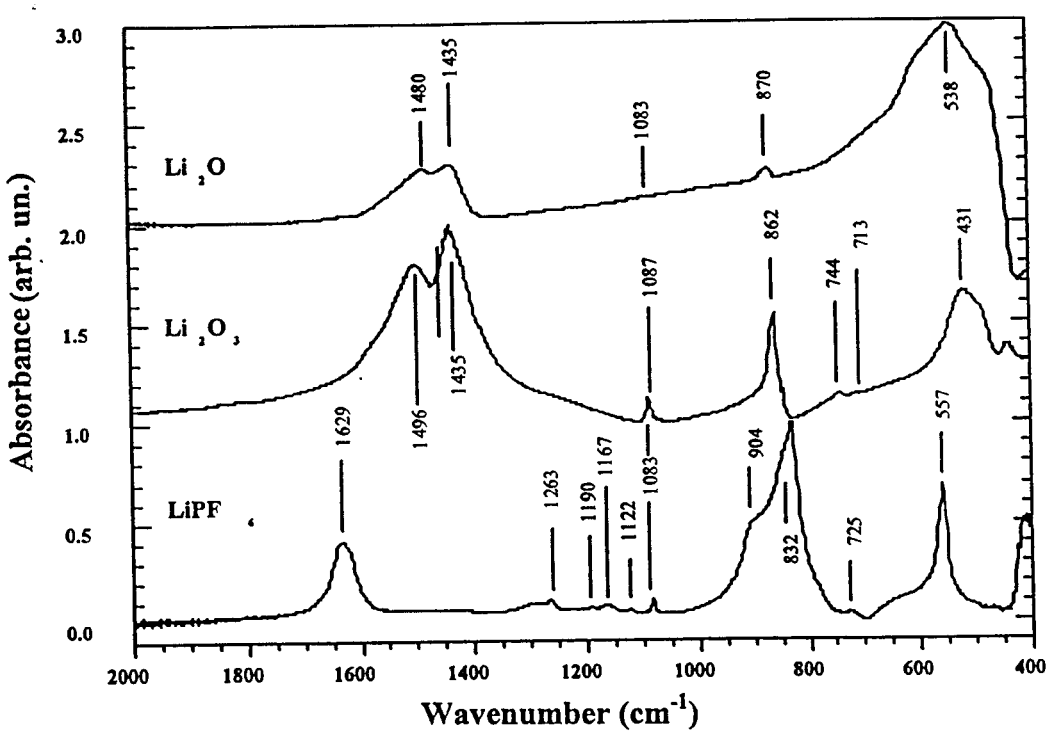

Figure I.4.12: IR spectra of $LiPF_6$, Li_2CO_3, and Li_2O.

I.4.4. General Conclusions:

The ring deformation modes in cyclic carbonates (700-800 cm^{-1}) and the C-O stretching in the ring (900-950 cm^{-1}) are very sensitive to the addition of a lithium salt. The C=O stretching is also broadened when a salt is added to the cyclic carbonates. However, the broadening increases by addition of more salt and resolution of peak splitting is reduced. The addition of a salt has increased the viscosity of the electrolyte

and has damped the vibrational modes of the solvents. The ring deformation mode is shifted to lower wavenumbers when salt is added to the solvent. For example, the ring deformation mode of EC is shifted from 732 to 725 cm^{-1}. The ratio of the peak intensity for the solvated molecules to that of the bulk can be used as a measure of the degree of solvation. In a mixed solvent electrolyte, the C=O stretching vibration of the cyclic carbonate is down- shifted and overlaps with the C=O stretching mode of the unsolvated linear carbonate. The selective solvation of Li^+ with the cyclic carbonate as compared with that of the linear carbonates correlates well with the higher donicity of the cyclic carbonate. Our results are in good agreement with an earlier NMR study [94,95]. A ^{13}C NMR study of the cyclic carbonates and linear carbonates containing $LiPF_6$ has shown that the C=O bond more strongly interacts with Li^+ than with the C=O of the linear carbonates. In addition, the oxygen in the C-O-C of the linear carbonate has a stronger interaction with the Li^+ than the C-O-C of the cyclic carbonate.

The intensity of the ring deformation mode (774 cm^{-1}) is decreased by the addition of $LiPF_6$. A significant band broadening is observed for C=O stretching when salt is added to the organic carbonate. However, the C-O stretching vibration did not change significantly. It can be concluded that the cyclic carbonates interact more strongly with the C=O than with the C-O in the ring. Although the possibility of bidendate Li^+ - PC exists, a stronger interaction exists between the C=O---Li^+ than that of the C-O---Li^+ complex.

Chapter 5

ELECTRODE – ELECTROLYTE INTERFACE IN LITHIUM BATTERIES

I.5.1. Introduction

The recent commercialization of the advanced lithium batteries is mainly due to the breakthrough in the stabilization of the anode-electrolyte interface. Although metallic lithium has the highest energy density (3,860 mAh/g) than all other alternative anodes, its poor performance and safety issues related to the low melting point of lithium (170 °C), dendritic growth during deposition (charge), and high reactivity toward electrolyte decomposition have hindered the commercialization of the rechargeable lithium batteries. Moli Energy Limited in Canada commercialized the first rechargeable lithium battery, (Li/MoS_2) with a metallic lithium anode. However, the Moli cells had a major setback due to the explosion of the cell in an operating device in Japan. This failure caused cell recall and finally stopped the production of this type of battery. The failure of the Moli cell was caused by the formation of lithium dendrites with a high surface area that reacted with the organic electrolyte and generated flammable gaseous species. In addition to gas generation, a passive film also forms on the surface of the metallic lithium. The surface film is electronically insulating, but it allows the transport of Li^+ across the film during charge and discharge of the cell. Despite extensive research efforts, the problem of dendrite formation during lithium deposition has not been solved. Many combinations of electrolytes with various organic additives have been used to suppress the dendritic growth of lithium electrode [103-111]. The use of metallic lithium anode has not been successful despite extensive research efforts during the past few decades [98,111-122]. Lithium dendrites usually penetrate through the electrolyte and cause an electric short in the cell with a massive generation of flammable gases. Therefore, much effort has been focused on search for an alternative anode for rechargeable lithium batteries [123-128].

There have been several approaches to solve the problem of lithium anode. One important approach has been the development of alternative anodes to avoid the use of metallic lithium. The development of lithium alloys, particularly the binary and ternary alloys have been very popular [121-132]. However, lithium alloys have poor performances mainly due to the large volume change (100-200%) during lithiation and delithiation processes. This expansion and contraction processes may cause the alloy particles to crack and lose contact with the electrode substrate. In addition, the lithium alloys with high concentration of lithium are very reactive toward electrolyte decomposition. Therefore a problem similar to that of the metallic lithium also exists for Li-alloy anodes. Recently, some success has been made using intermetallic alloys such as Cu_6Sn_5 that insert lithium topotactically over a wide composition range $Li_xCu_6Sn_5$ ($0<x<13$) [133]. Despite the good volumetric energy density of these alloys, their gravimetric energy density is poor and there is significant capacity loss during multiple cycling.

The early transition metal oxide anodes also have been proposed for application in rechargeable lithium batteries. In particular, the use of lithium intercalated titanium oxide [134-139]. The lithium titanium oxide anode is described as a zero-strain insertion anode owing to negligible volume change during the lithium insertion/extraction process. In addition, the titanium oxide anode does not decompose the organic electrolytes, hence it can be considered as a safe anode for rechargeable lithium batteries. The drawback of the lithiated titanium oxide anode is its high redox potential (1.5 V vs Li). Therefore, there is 1.5 volt less voltage when using a titanium oxide anode. Titanium oxide is a

semiconductor with a band gap of (3.26 eV for the anatase and 3.05 eV for the rutile phase) [140-143], and also requires conductive additives (carbon) to make a practical anode.

When the titanium oxide anode is combined with the current $LiCoO_2$ cathode, $Li_{1/2}TiO_2/LiCoO_2$ it provides an average cell voltage of 2.25 V with an excellent cycle life performance. The particle size of titanium oxide also can be tailored to nanoscale, suitable for high-power (high rate) batteries. Ohzuko et al. [144] have shown very good reversibility and electrochemical performances for $Li_4Ti_5O_{12}$. The oxide can be described in spinel notation as $Li[Li_{1/3}Ti_{5/3}]O_4$, indicating a mixture of Li and Ti on the 16d octahedral sites.

Lithium transition metal nitrides and phosphides also have been considered as anodes for rechargeable lithium batteries [145-151]. The voltage profiles of nitrides and phosphides during charge-discharge are between 0 V to 1.5 V vs Li. There is also a large voltage hysteresis between the charge and the discharge of nitrides and phosphides. The principal mechanism is believed to be the formation of lithium nitride and phosphide during reduction of transition metal ions to the metallic state. The nano-scale transition metal clusters formed in this process are catalytically active, and during lithium extraction reaction they tend to form the original compound. The slow kinetics and large hysterises between charge and discharge is a major drawback for the nitride and phosphide anodes.

In early 1990, a breakthrough was announced by researchers form Sony Energytech: an anode based on lithium intercalated carbon or graphite for rechargeable lithium battery was used [152]. The volume change during full lithium intercalation in graphite (LiC_6) is less than 9% according to the in-situ X-ray diffraction study. The specific capacity of the lithiated graphite is only LiC_6 (370 mAh/g), much lower than that of metallic lithium (3,860 mAh/g). In spite of much lower energy density, the current rechargeable lithium battery (Li-ion battery) technology uses a lithiated carbonaceous anode [153-157]. The success of the LiC_6 anode is mainly due to the fast stabilization of the anode/electrolyte interface and the high electrochemical reversibility of lithium intercalation/deintercalation process. The LiC_6 anodes have been charged and discharged over 1000 times without an appreciable capacity loss. The Li-ion battery is currently replacing all other battery types in the market, particularly in the field of electronics, computers, and communications. In recent years, the application of the Li-ion batteries for more power demanding applications such as power tools, stationary, and transportation has started. The production of Li-ion batteries in 2002 have exceeded 500 million cells, with Japan as the main producer (over 70%).

Lithium intercalation in graphite is not new and has been fully studied by physicists in search of high T_C superconductors during the last 50 years [158,159]. The hexagonal structure of graphite in ABAB arrangement is shown in Figure I.5.1. The layer B is shifted with respect to the A layer, but AA and BB layers are on exact registry with each other. When lithium intercalates between the layers, the layer B glides to make an exact AAAA structure.

Crystallographic structure of graphite

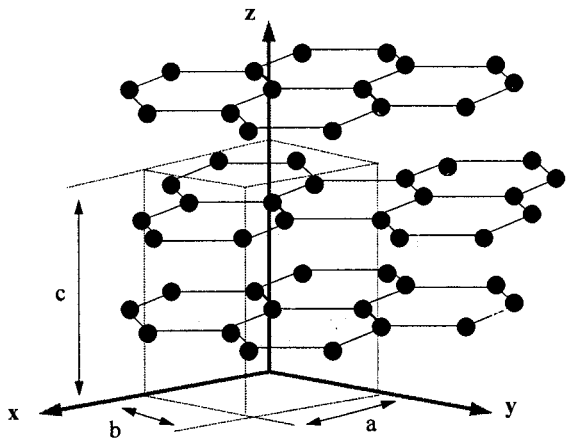

Figure I.5.1: Schematic of graphite and lithium intercalated graphite.

Graphite has an ideal layered structure with weak van der Waals bonding between the graphene layers. Thus, Li can be stored between the layers of graphite. According to recent ^{6}Li- and ^{7}Li- NMR studies, the nature of lithium in graphite is partly ionic. There is partial charge transfer from lithium to the π-orbital of the graphene planes. The lithium in the graphite has also a high mobility, which is an ideal situation for application in high-power battery. In addition, the graphite has very high electronic conductivity, hence electrode resistance is very low. Natural graphite is abundant, and synthetic graphite also can be made from variety of precursors. Heat treatment of various organic polymers, particularly those with a conjugated benzene rings goes through a carbonization process around 1200-1500 °C and graphitization around 2300-3000°C. During graphitization, the rate of growth in ***a*** and ***c*** directions are strongly temperature dependent. Therefore, graphite flakes with extended ***a*** or ***c*** directions can be made for different applications. The ideal graphite structure consists of layers of carbon atoms arranged in hexagonal

rings that are stacked in an ABAB sequence Figure I.5.1. The graphite comprises planar hexagonal networks of carbon atoms (honeycombs) with two different crystalline forms, hexagonal (*2H*) and rhombohedral (*3R*). The *2H* graphite structure is the most common and the carbon layers are arranged in the ABAB sequence, where the B layers are shifted to a registered position with respect to the A layers. In the *3R* (rhombohedral) structure, the stacking sequence is ABCABC, where the C layers are also shifted by the same distance with respect to the B layers, as the B layers are shifted with respect to the A layers [160].

The separation of the layers in well-graphitized sample is 3.35 Å, and layers are held together with weak van der Waals bond. The softness and the lubricity of graphite can be attributed to the easy glide of these layers over one another. Within each graphene layer only three carbon atoms surround each carbon atom. After forming one σ bond which each neighbor, each carbon atom would still have one electron and these are paired up into a system of π bonds [161]. Resonance with other structures having different but equivalent arrangements of the double bonds makes all C-C distances equal at 1.415 Å. This is a little longer than the C-C distance in benzene, where the bond order is 1.5, and agrees with the assumption that the bond order in graphite is $\cong$ 1.33.

Earlier studies of alkaline metal intercalation in graphite have shown that the ABAB structure of graphite shifts to form an AAAA structure when the alkali metal is intercalated between the graphene sheets. This layer gliding is not surprising, as the bonding between the graphene sheets are weak that makes the graphite a good solid lubricant.

I.5.2. Experimental:

Several natural and synthetic graphite samples (BG-34, BG-35, CPC, CN-39, CN-39A, SFG-15) with different morphology, particle size, and surface area were obtained from Superior Graphite Co. Figure I.5.2 shows the morphology of various graphite samples examined in this work.

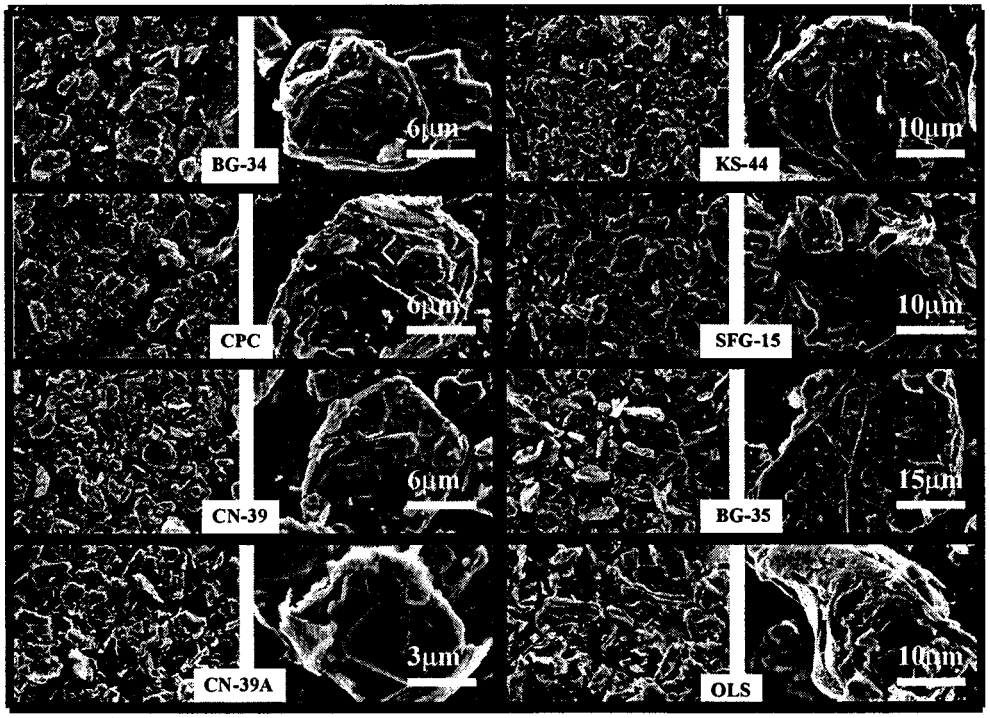

Figure I.5.2: SEM morphology of natural graphites BG34, BG35, KS44, and synthetic graphite samples CPC, CN-39, CN39A, and SFG-15.

The X-ray diffraction of various graphitic samples used in this work is shown in Figure I.5.3. The shape and intense 002 peak is the indication of good crstallinity of the samples.

Table I.5.1: Surface area of various commercial graphite samples

Graphite	**BG-35**	**BG-34**	**KS-44**	**CN-39**	**CN-39**	**CPC**
Surface area (m^2/g)	7.0	7.8	10	10.5	12.5	7.0

The surface area of different graphite samples used in this work is listed in Table I.5.1. These samples are considered low surface area, and suitable for battery applications. Because of the high reactivity of lithiated graphite, lower surface area samples are preferred.

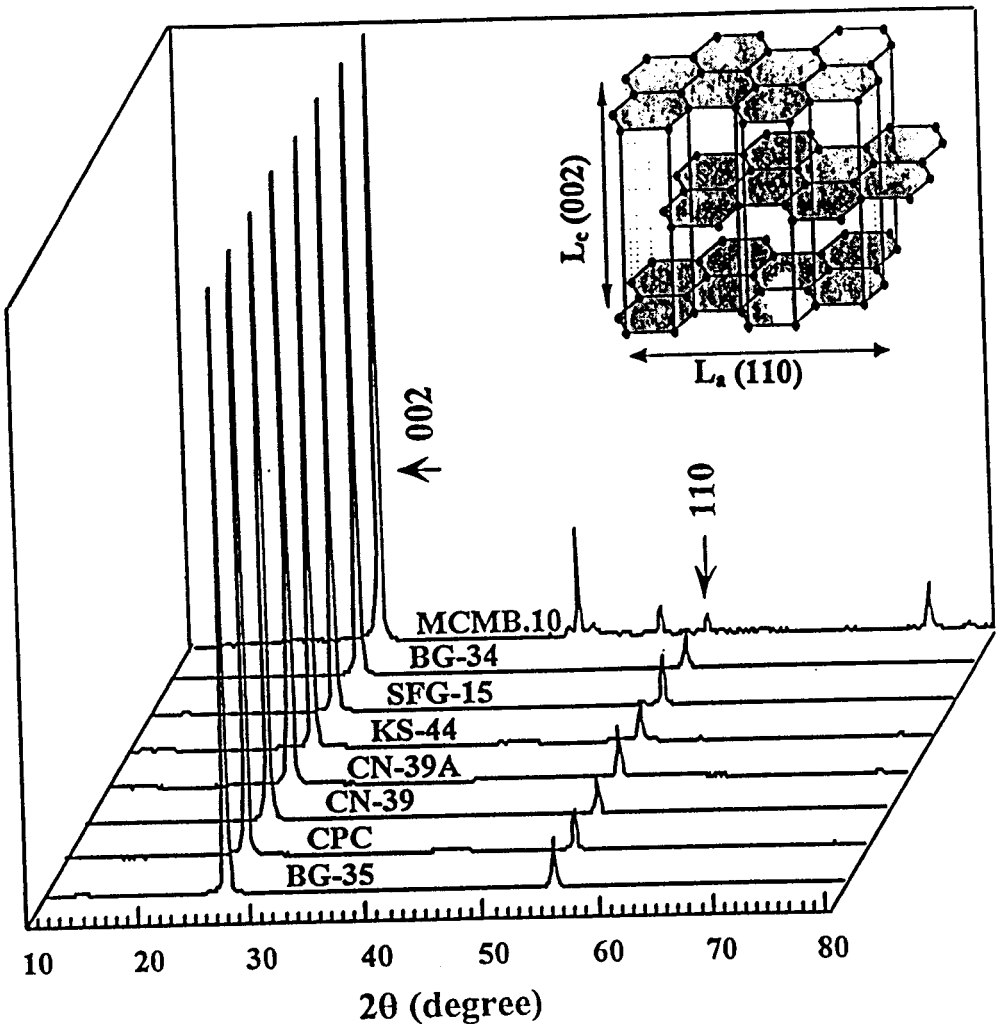

Figure I. 5.3: X-ray diffraction of various graphite samples.

The graphite samples were heated in vacuum between 700-900°C to remove moisture and attached functional groups, which usually exist at the edge of graphene sheets. It is very important to remove the water molecules trapped in graphite before useing it in a lithium battery. Previous temperature program desorption (TPD) study has shown that almost all surface functional groups can be removed at 700-900°C. The heat treated graphite was then transferred into a dry box, and mixed with 8-10 w% conductive diluent carbon (Shwaingan black). The mixture was then mixed with 4-5 w% EPDM binder to make an ink-type slurry. The EPDM binder was prepared by dissolving 5 W% in xylene. The mixture of graphite sample, diluent carbon, and binder was ball milled together for 10 minutes using a commercial micronizer (from M^{c}CRONE Accessories & Components). An ink-type slurry is formed during the milling process. The slurry was spread on the surface of a 13-micron thick copper foil. The coated copper foil was dried in the vacuum oven anti-chamber of the dry box at 100°C for at least 4 hours to remove xylene. To improve the adhesion of sample to the copper foil, the sample was hot pressed inside of a dry box at 100°C for 10 minutes. The coating process to make an electrode for lithium cells is shown in Figure I.5.4.

Electrodes were cut from the coated foil to make the lithium cells. Two types of cells were constructed. A 10x10 cm^2 electrode was also cut to study the surface reaction and electrolyte decomposition using GC-MS system. Figure I.5.6 shows the structure of cell used for measuring gaseous species formed during electrolyte decomposition. The graphite electrode was against a metallic lithium electrode with a porous polyethylene

polypropylene separator soaked with electrolyte between the two electrodes. The cell was placed inside of polyethylene coated aluminum pouch and sealed Figure I.5.6.

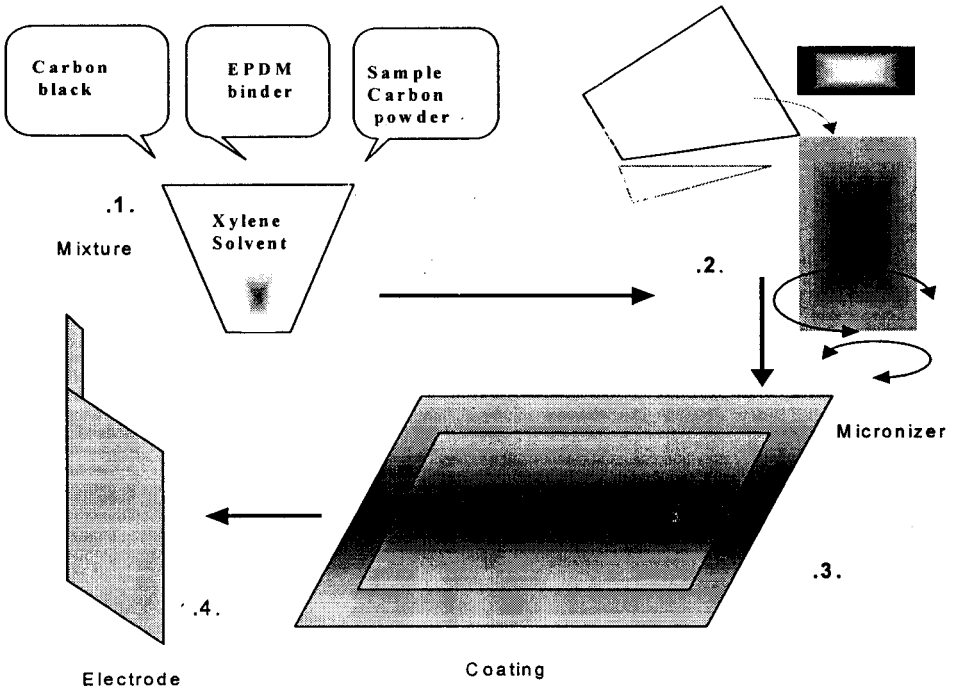

Figure. I.5.4: Coating process to make electrode for lithium cells, Anode is metallic lithium the cathode is the graphite electrode, and reference electrode is lithium wire inserted in the cell between to layers of porous separator.

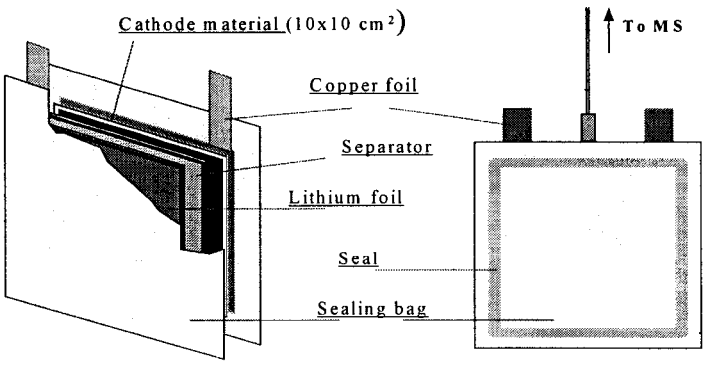

Figure. I.5.5: Schematic of Li/Graphite cell for in-situ GC-MS analysis of electrolyte decomposition during lithium intercalation in graphite electrodes.

A 5 cm^2 disc electrode was cut for evaluation of energy capacity and cycle life tests. Figure. I.5.6 shows the assembly used for testing the energy capacity and reversibility of graphite electrodes.

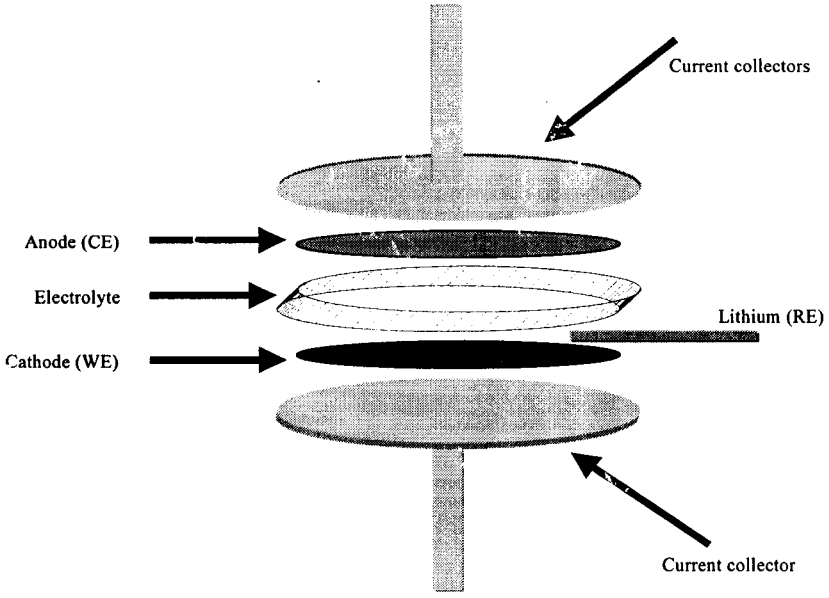

Figure I.5.6: Schematic of lithium cell for evaluation of graphite anodes. WE = working electrode, CE = counter electrode and RE = reference electrode.

The electrolyte decomposition occurs on the surface of graphite during initial lithium intercalation. In order to investigate the nature of the evolving gas, a special cell assembly is constructed to allow the generated gas to escape from the cell and be sampled by in-situ GC-MS analysis. Before sealing the cell shown in Figure I.5.5 a flexible 2 mm diameter tube was inserted in the cell. The tube was connected to an on-line GC-MS system. Figure 1.5.7 shows the combined GC-MS equipment used for in-situ analysis of gases forming during initial lithium insertion into graphite anode. The GC system is

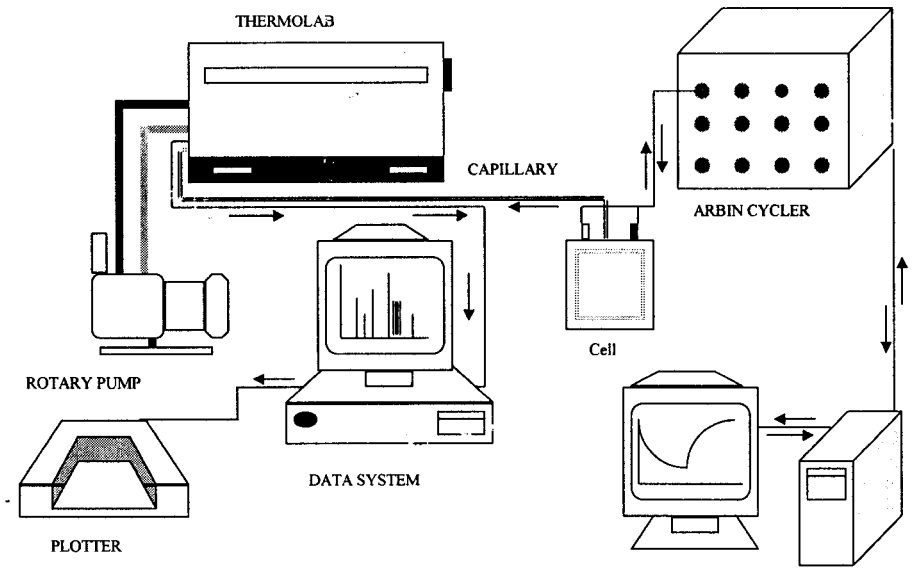

Figure I.5.7: Schematic of on-line GC-MS for analysis of gases generated during lithium intercalation in graphite anode due to electrolyte decomposition.

equipped with a calibrated propac column heated to 120 °C. The mass spectrometer used in this work was a MS Thermal Analytical (TA) system with 1-200 m/e range.

The electrochemical charge-discharge of the cell was performed using a Macorr-type battery cycler . The Macorr cycler is capable of applying constant current in the range of 0-100 mA and monitoring the cell voltage in real-time during lithium intercalation (charge) and deintercalation (discharge) processes. The Macorr battery cycler was a multi channel battery tester with 24 channels.

The X-ray diffraction facility and the infrared spectrometer used in this work have been described in Chapter 2. The Li/graphite cells after charging and discharging cycles were disassembled, and the electrode was rinsed with pure dimethyl carbonate (3 times) to remove excess salt. The IR spectra of the surface film was then obtained using a diffuse reflectance accessory that allows to install the sample inside the dry box and later transferred to the IR spectrometer for analysis.

In order to understand the thermal properties of the surface film, a sample was collected from the surface of the graphite electrode (inside the dry box) and placed in a hermetically sealed DSC pan. The sample was analyzed using a Perkin Elmer Model 7 differential scanning calorimetry. The temperature of the sample was raised at 5 °C/minutes and the heat absorbed or released during heating was monitored. The DSC pan was a screw-top stainless steel model from Perkin Elmer.

I.5.3. Results and discussion

The lithium intercalation – deintercalation process between the graphene planes of graphitic samples is facile. The high lithium storage in graphite (up to LiC_6) with a high lithium mobility, has provided a unique anode for rechargeable lithium battery. The voltage of the lithiated graphite is very close to the voltage of metallic lithium (100-300 mV vs Li). In addition, the voltage profiles of the graphite anode during lithium intercalation/deintercalation process are flat with a very small hysteresis. The electrochemical lithium intercalation into graphite can be described as,

$$Li^+ + 6C + e^- \rightarrow LiC_6$$

The graphite can accommodate one lithium per six carbons to form the so-called "stage one" (LiC_6) compound. High-pressure intercalation synthesis has yielded a lithium rich phase, LiC_3. However, the LiC_3 phase is not stable at ambient pressure. It is interesting to note that the amount of lithium in 1 cm^3 of LiC_3 is higher than that of the pure metallic lithium.

The lithium intercalated graphite is highly reactive and reacts with the electrolyte solution. The by-product of the electrolyte decomposition forms a solid film on the surface of the electrode. The electrolyte decomposition during the lithium intercalation occurs at about 0.8 V vs Li. In parallel with the electrolyte decomposition, lithium intercalation in graphite also proceeds. The film formed on the graphite surface is called solid electrolyte interface (SEI layer). The film is electronically insulating and ionically conducting. The SEI layer protects the lithiated graphite from further reaction with electrolyte. Therefore, the electrolyte decomposition stops at subsequent charge – discharge cycles. The nature of the film formed on the surface of the carbonaceous anodes depends on the composition of electrolyte. Ethylene carbonate based electrolytes tend to form a good compact SEI layer, and in most commercial lithium battery the electrolyte contain EC in addition to other carbonate solvents. The use of electrolyte with only propylene carbonate solvent has not been successful, due to the co-intercalation of solvent and exfoliation of the graphitic anode. In practice, usually EC in combination with other linear carbonate solvents such as dimethyl carbonate, diethyl carbonate, or methyl ethyl carbonates are used. Figure I.5.8 shows the voltage profile of graphitic anode during the lithium intercalation process.

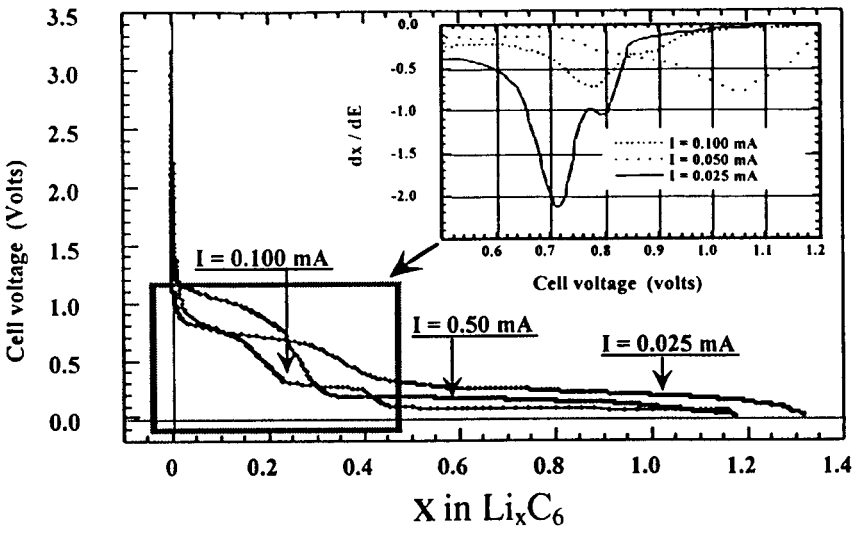

Figure I.5.8: Voltage profile of graphite anode as a function of lithium concentration at 0.025 mA, 0.5mA, and 0.1mA constant current charging.

The voltage plateau at about 0.8 volt is due to the electrolyte decomposition. It is important to note that when charging the electrode at a higher current density, a more protective film is formed, and less electrolyte decomposition occurs. The voltage plateaus between the 0.3 –0.01 volts are an indication of the staging phenomena usually observed for the formation of LiC_6, LiC_{12}, and other dilute phases of LiC_n (n= 24, 36, etc). The insert in Figure.I.5.8 shows the derivative of the voltage profile for the electrolyte decomposition part of the graph. The first charge-discharge of various graphitic electrodes is shown in Figure I.5.9. After initial lithiation, in the first cycle the electrode/electrolyte interface is stable and does not react with the electrolyte. The voltage of the graphite drops to very low value (300 mV vs. Li) by intercalation of a small amount of lithium ($Li_{0.05}C_6$).

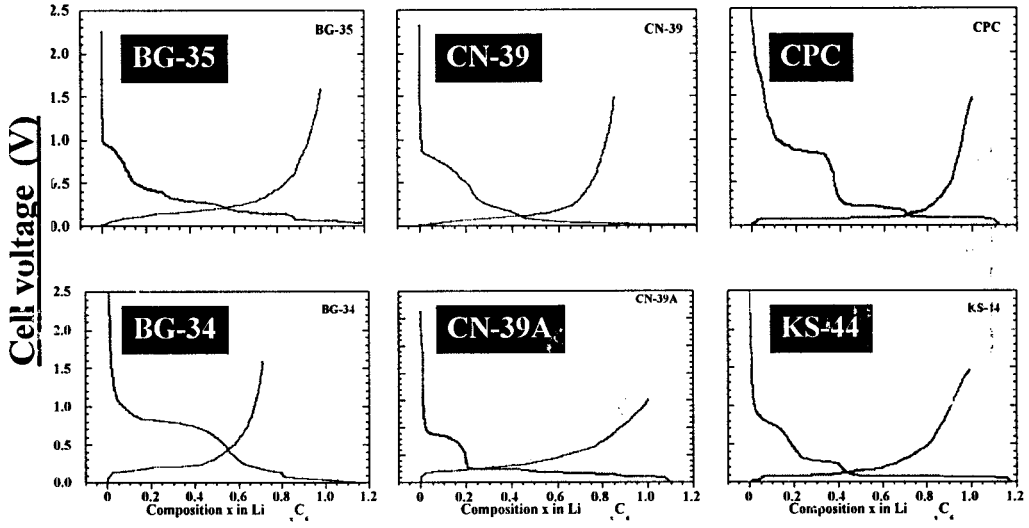

Figure I.5.9: The voltage profile of graphitic electrodes, (BG-35, CN-339, CPC, BG-34, CN-39A, and KS44).

All samples have shown some degree of electrolyte decomposition during the first lithium intercalation. The decomposition plateau for the BG-35 is less than for the other samples. When sample has high degree of crystallinity, the staging phenomenon is observed with better resolution, as seen for the case of highly crystalline KS-44.

The amount of electrolyte decomposition is also depends on the composition of electrolyte. Figure I.5.10 shows the voltage profile of electrode made from CPC during lithium intercalation process in different electrolyte compositions. The electrolyte containing EC-DEC-$LiPF_6$ show less electrolyte decomposition. This suggests that the electrolyte containing cyclic ethylene carbonate and linear carbonate may provide a safer operation for the lithium battery. In Chapter 3, we also discussed how the addition of

linear carbonate to cyclic carbonate may improve the conductivity of the electrolyte, particularly at lower temperatures.

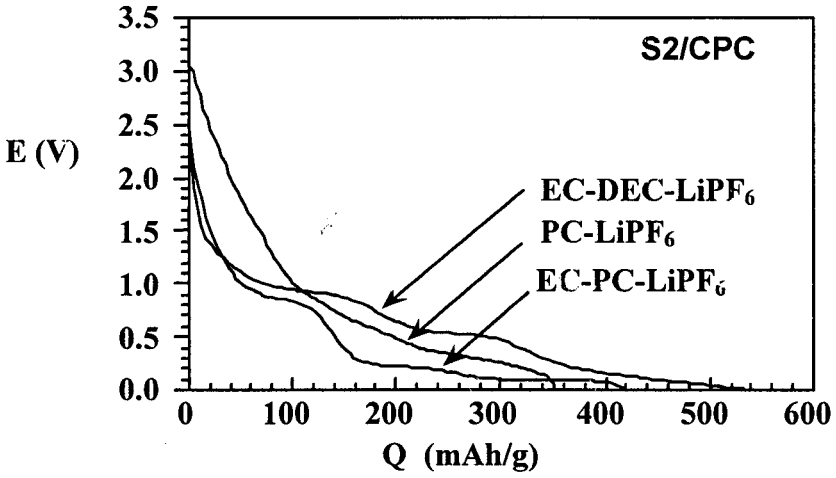

Figure I.5.10: Voltage profile of CPC graphite anode in different electrolytes.

The interface of graphite electrode is stabilized after the first charge-discharge cycle. The subsequent cycles do not show any sign of electrolyte decomposition. The multiple charge-discharge cycles of the graphite anode are shown in Figure I.5.11. The charge-discharge cycles are very reversible, and there is no sign of an electrolyte decomposition, (plateau at 0.8V). At low charging rate, low current densities (<1mA/cm^2), close to theoretical capacity (372 mAh/g) were obtained. The rate at which the electrode can be charged depends also on the amount of active materials loaded on the substrate. For the design of a high rate (power) battery, the coating is thinner that the electrode designed for high-energy applications.The usual loading for high power battery is about 10-20 mg/cm^2 and for the high-energy cells the loading may exceed 100 mg/cm^2.

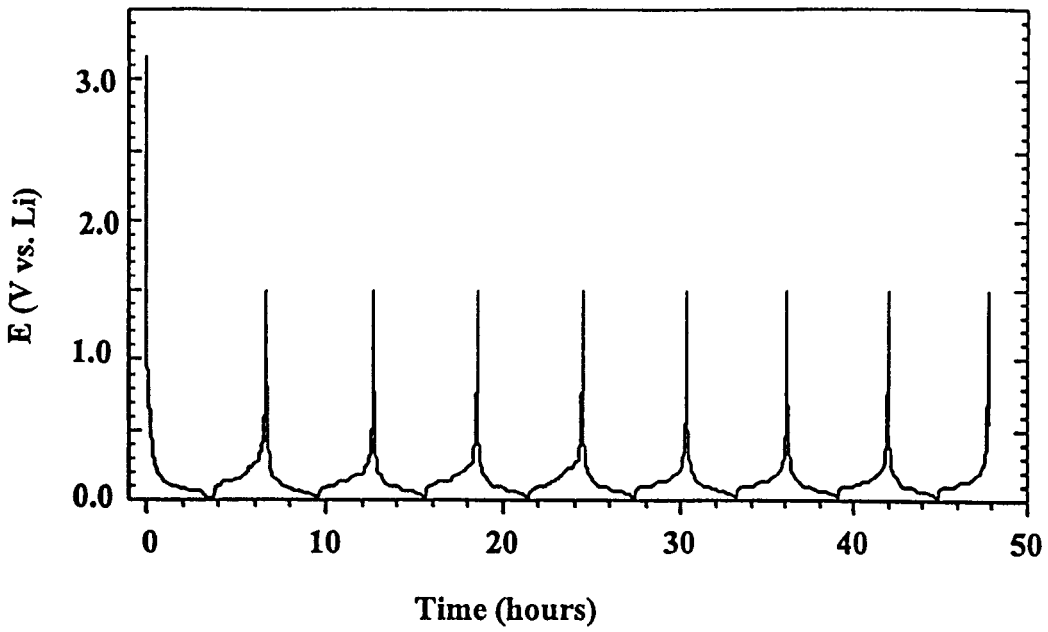

Figure. I.5.11: The multiple charge-discharge cycles of the graphite electrode after stabilization of the electrode/electrolyte interface and formation of the SEI layer.

Disordered carbons also have been used as anode. However, their capacity is almost ½ that of the graphitic anodes, and their voltage profile during lithium intercalation does not show the staging process that often observed for the graphitic anodes. Some special carbon anodes with extended single layer graphene sheets, store lithium to a level more than the theoretical capacity (372 mAh/g). In this case, the lithium is being adsorbed on both sides of the graphene sheets. However, the cycle life of this type of carbon is poor and there is significant capacity loss during multiple charge-discharge cycles. In addition there is considerable amount of voltage hysterises between the charge and discharge voltage profiles. The sloping charge-discharge profile also suggests that there are various sites for lithium with different affinities.

I.5.4. Gas generation on carbon anodes

Carbonaceous anodes are widely used in lithium-ion battery, mainly because of high reversibility, high specific energy density, and high rate capability. Despite the superior performance of carbonaceous anodes vs. other alternative anodes, there is considerable reactivity of lithiated graphite with organic electrolytes during the first charge cycle, which is a major safety concern. The nature of the gaseous species being generated on the surface of graphitic anodes during initial lithium intercalation is studied in this work. The correlation between graphite surface area and their irreversible capacity loss has been investigated. A linear relationship was observed between the surface area and the irreversible capacity loss of graphite anodes.

Several natural and synthetic graphite materials, BG-34, BG-35, CPC, CN-39, CN-39A, SFG-15, etc. have been studied. The excessive electrolyte decomposition during the first lithiation process causes the irreversible capacity loss. The formation of gaseous species is detrimental to the performance of lithium cells and they are considered safety hazard as the majority of the gaseous species formed are flammable. Some of the gaseous species may also dissolve in organic electrolyte and participate in parasitic reactions.

The structure and degree of graphitization of the carbon electrode plays a critical role in the performance and safety of Li-ion batteries. The major effort is directed to understanding the relationship between the physicochemical properties of carbonaceous materials and their electrochemical performance. The crystallinity of carbonaceous material and the nature of the electrolyte used are important factors on the

electrochemical stability of Li-ion cells and on the nature of gases generated during the Lithium insertion/extraction process. The volume and composition of gaseous specious generated on various graphitic electrodes depends on the graphite crystallinity, surface area, and composition of electrolyte used. Graphite anodes with high degree of crystallinity generate less gas during the first lithium intercalation cycle.

Table I.5.2: Gas Chromatography and Mass Spectrometry analysis of the various gases generated on the surface of different graphite anodes during the first lithium intercalation process

Graphite	Electrolytes	C_2H_4	CH_4	C_2H_6	C_3H_6	CO	O_2	H_2	CO_2	Vol_{total} (ml/g)
BG-35	EC-DEC	3.33	0	0	0	2.25	0	1.25	0	10.11
	EC-PC	2.36	0	0	0.98	3.33	0	0.98	0	19.13
	EC-DMC	0.56	0	0	0	3.96	0	1.02	0	12.82
	PC-DMC	0	0	0	0.66	4.58	0	1.21	0	29.36
CPC	EC-DEC	1.23	0	0	0	1.85	0	1.23	0	12.32
	EC-PC	0.39	0	0	1.11	2.98	0	0.21	0	19.97
	EC-DMC	0.69	0	0	0	3.44	0	0.98	0	12.92
	PC-DMC	0	0	0	2.03	3.99	0	1.20	0	32.53
CN-39	EC-DEC	0.11	0	0	0	2.55	0	0.84	0	8.06
	EC-PC	0.22	0	0	0.97	3.68	0	0.96	0	11.58
	EC-DMC	0.34	0	0	0	4.11	0	0.99	0	12.24
	PC-DMC	0	0	0	2.11	5.22	0	1.06	0	24.05
CN-39A	EC-DEC	0.31	0	0	0	3.02	0	1.02	0	9.36
	EC-PC	0.33	0	0	0.78	3.68	0	1.11	0	15.12
	EC-DMC	0.31	0	0	0	4.58	0	1.23	0	17.12
	PC-DMC	0	0	0	0.99	4.89	0	1.22	0	28.06
KS-44	EC-DEC	0.87	0	0	0	2.31	0	0.78	0	10.13
	EC-PC	0.54	0	0	1.02	2.97	0	0.29	0	13.14
	EC-DMC	0.35	0	0	0	3.33	0	1.00	0	19.12
	PC-DMC	0	0	0	1.33	3.69	0	1.31	0	29.86
SFG-15	EC-DEC	0.69	0	0	0	2.22	0	0.96	0	11.02
	EC-PC	0.68	0	0	0.97	3.09	0	0.56	0	13.77
	EC-DMC	0.35	0	0	0	2.99	0	1.08	0	13.98
	PC-DMC	0	0	0	2.02	4.21	0	1.04	0	30.93
BG-34	EC-DEC	0.98	0	0	0	3.01	0	0.87	0	10.02
	EC-PC	0.57	0	0	1.87	3.77	0	0.59	0	15.63
	EC-DMC	0.48	0	0	0	4.56	0	1.17	0	16.67
	PC-DMC	0	0	0	2.96	4.89	0	1.19	0	34.13

Careful analysis of various carbonaceous anodes indicates that a gel-type film is also forming on electrode surface as a result of electrolyte decomposition. The nature of the

film formed on a carbonaceous anode has a significant impact on the rate capability and the overall cell impedance.

I.5.5. Infrared spectroscopy of SEI layer on graphite anodes

The film formed on the surface of graphite anode during electrolyte decomposition can be probed using IR spectroscopy. After initial charge-discharge, the cell was opened in the dry box, and a disc (1 cm diameter) was cut from the electrode. The disc was rinsed with salt free dimethyl carbonate solvent to remove excess electrolyte, and dried in the ambient of the dry box for at least 2 hours prior to IR study. The sample was placed in a diffuse scattering IR accessory (from Spectratech) and sealed inside the dry box and transferred to the IR spectrometer. The IR spectra of graphite electrode without the electrochemical cycling test were used as the reference spectra. The IR spectra of the film formed on the surface of BG-34 graphite anode after one full charge-discharge cycles are shown in Figure I.5.12. The complex IR spectrum with several absorption peaks obtained indicates, formation of an organic moiety different from the electrolyte used. The IR peaks around 870-890 and 1456 cm^{-1} are assigned to the formation of Li_2CO_3. There is also an indication of the formation of lithium-organic compounds such as CH_3OCOLi with an IR absorption peak around 1600-1630 cm^{-1} assigned to the C=O stretch.

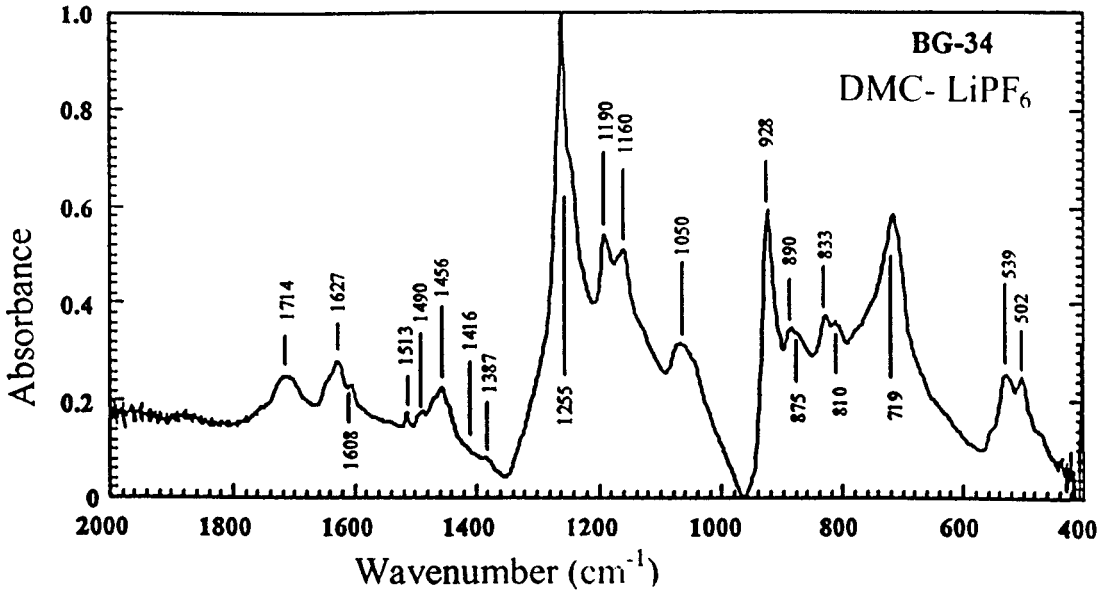

Figure I.5.12: IR spectrum of the film formed on the surface of graphite anode during lithium intercalation in (EC-DMC 1:1mol) + 1M $LiPF_6$ electrolyte.

Table I.5.3: Vibrational Frequencies on the surface layer on BG-34 graphite in DMC-$LiPF_6$.

		Assignment	
ν observed (cm^{-1})	ν assigned	bands	Compounds
1714br			
1627br		CO_2 stretch	
1608sh		-	
1513w		-	
1490sh		-	
1456br	1420-1470	-	Carbonate ion
	1441	-	Li_2CO_3
1416sh		-	
1387sh	1360-1380	CH bend	$LiOCH_3$
1255sp	1280	-	Dimethyl Carbonate
1190m		CO stretch	
1160m	1150-1170	CH stretch	$LiOCH_3$
1050br	1050-1070	CH stretch	$LiOCH_3$
	1020-1090	CO stretch	Carbonate ion
928sp	969-914	-	Dimethyl Carbonate
890m		-	
875sh	820-890	-	Carbonate ion
	866	-	Li_2CO_3
833m	820-890	-	Carbonate ion
	846	CO_3 bend	Li_2CO_3
810sh		-	
719sp	680-750	-	Carbonate ion
	738	CO_2 asym. bend	Li_2CO_3
539m	550-650	LiO stretch	$LiOCH_3$
502m		-	

(w : weak , m : medium, s : strong , sh : shoulder, br : broad, v : very, sp : sharp)

As we observed in the analysis of gaseous species generated when DMC is present in the electrolyte, the formation of $CH_2=CH_2$ is also suggests the following decomposition reactions.

$$2Li^+ + 2e^- + CH_3OCOOCH_3 \rightarrow Li_2CO_3 + CH_3-CH$$
$$2Li^+ + 2e^- + CH_3OCOOCH_3 \rightarrow CH_3OCOLi + CH_3OLi$$
$$CH_3OCOLi + CH_3OLi + \text{residual } H_2O \rightarrow Li_2CO_3 + CH_3OLi + CO_2.$$

The IR spectrum of the film formed on BG-34 in EC-DMC(1:1mol) + $LiPF_6$ is more complex, indicating significant involvement of EC decomposition on the surface of lithiated graphite Figure I.5.13. The peaks corresponding to the formation of organo-lithium compounds as well as Li_2CO_3 are present. The IR peaks at 844 and1483 cm^{-1} are assigned to the lithium carbonate. The peak at 1083 can be assigned to CH_3OLi, and CH_3OCO_2Li, various C-H bending of CH_3 and CH_2 groups.

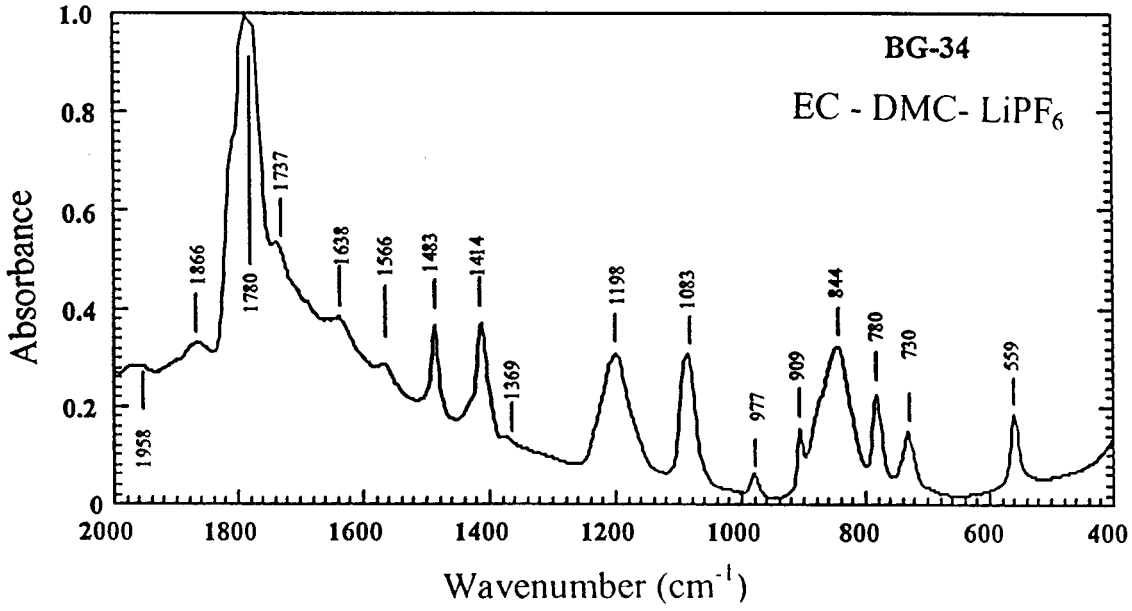

Figure I.5.13: IR spectrum of film formed on lithiated graphite during the first lithium intercalation process in EC-DMC (1:1mol) + 1M$LiPF_6$ electrolyte.

Table I.5.4: Vibrational frequencies on the surface layer on BG-35 graphite in EC-DMC-$LiPF_6$.

		Assignment	
ν observed (cm^{-1})	**ν assigned**	**bands**	**Compounds**
1958vw			
1866w	1870-1750	-	Organic Carbonate
	1870	-	Ethylene Carbonate
1780sp	1870-1750	-	Organic Carbonate
	1760	-	Dimethyl Carbonate
1737sh	1870-1750	-	Organic Carbonate
1638sh	1629	-	$LiPF_6$*
1566sh	1580	O-C-O stretch	RCOOLi
1483sp		CH_2 bend	
1414sp	1441	-	Li_2CO_3
	1420	-	Li_2CO_3
1369sh	1380-1360	CH bend	$LiOCH_3$
1198br	1170-1150	CH stretch	$LiOCH_3$
1083sp	1089	CO stretch	Li_2CO_3
	1085	CO stretch	RCO_3Li
	1074	-	Ethylene Carbonate
	1083	-	$LiPF_6$*
977m	974	-	Ethylene Carbonate
909sp		-	
844br	846	CO_3 bending	Li_2CO_3
	858	-	Dimethyl Carbonate
	850	-	LiF
	832	-	$LiPF_6$*
780sp	745-789	-	LiO
	774	-	Ethylene Carbonate
		-	
730sp	738	CO_2 asym. bend	Li_2CO_3
	740	CO_2 asym. bend	Li_2CO_3
559sp	550	-	LiF
	557	-	$LiPF_6$*
	552	LiO stretching	Li_2O_2

(w : weak , m : medium, s : strong , sh : shoulder, br : broad, v : very, sp : sharp)

The IR spectrum of film formed on graphite during first lithium intercalation in EC-DEC (1:1mol) + 1M$LiPF_6$ is shown in Figure I. 5.14. The complex spectrum with several IR absorption peaks shows decomposition by-product of the EC-and DEC solvents. The richness of the spectrum indicated that besides $Li_2CO_{3(\text{solid})}$, $CH_2{=}CH_{2(gas)}$, and $CH_3\text{-}CH_{3(gas)}$ there are various other organo-lithium compounds present. The IR peaks at around 700-800 are matched with the bending mode of δ_{CO3} in $ROCO_2Li$. Because of the gelatinous nature of the film formed on the surface of the graphite, there is a possibility of ring opening decomposition of EC and formation of organo-lithium dimers or trimers of EC (similar to the ring opening polymerization).

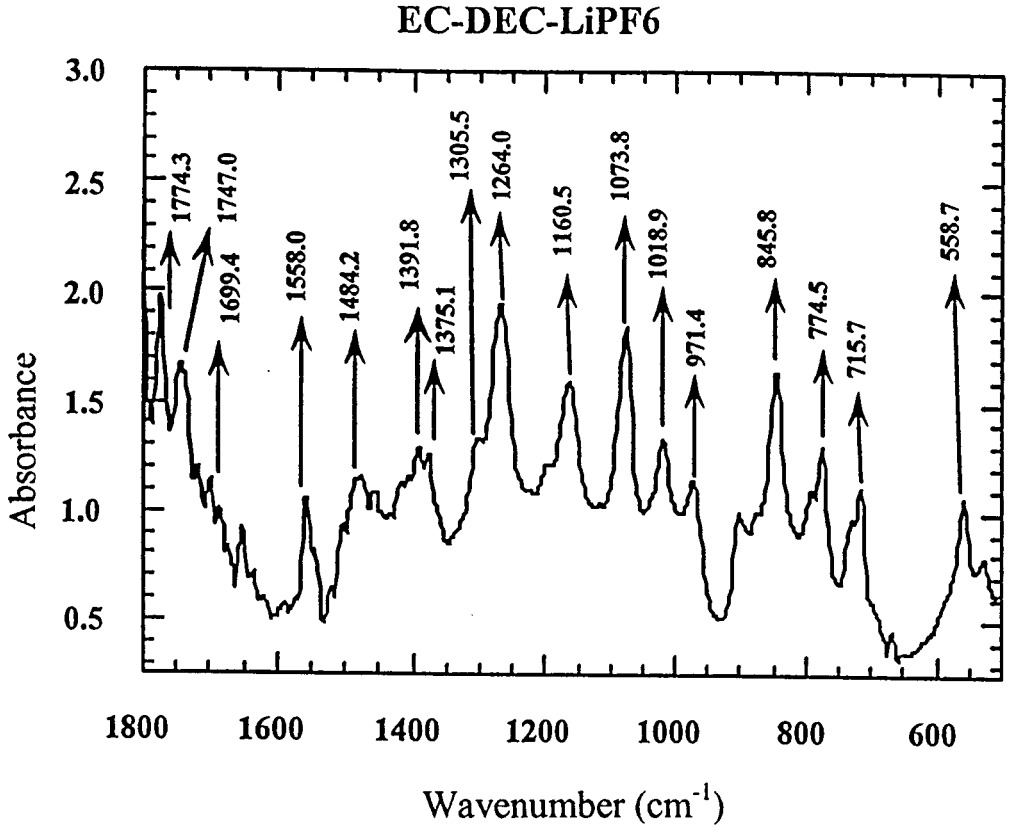

Figure I.5.14: IR spectrum of film formed on BG-34 in EC-DEC + 1MLiPF$_6$ during first lithiation process.

The IR peak assignments for SEI layer formed on the surface of graphite during the first lithium intercalation are listed in Table I.5.5. The IR peaks correspond to the formation of residual lithium carbonate with peaks around 1400 cm^{-1}, formation of various organo-lithium compounds as well as IR peaks for the C=O stretching vibrations at 1650-1800 cm^{-1}.

Table I.5.5: Vibrational frequencies on the surface layer on graphite in EC-DEC-$LiPF_6$.

Observed	Assignment ν assigned	bands	compounds
1966sp			
1860sh	1870		Ethylene Carbonate
1809sp	-		
1771sp	1750-1870		Organic Carbonate
1746m	1750		Diethyl Carbonate
1699w	-		
1685w	-		
1652m	1650	CO_2 stretch	RCO_3Li
1555sp	1580		RCOOLi
	1580		LiOH
1505sh	1500		$(CH_2OLi)_2$
1479w	-	-	Ethylene Carbonate
1457w	1450-1480	CH bend	$LiOCH_3$
	1445	CH, CH_3 asy. bend	Ethyl-CO_3Li
1390w	-	-	Ethylene Carbonate
	1360-1380	CH bend	$LiOCH_3$
1374w	1351	CO_2 sym. stretch	Ethyl-CO_3Li
1296sh	-		
1267sp	1262	-	Diethyl Carbonate
1195sh	-	CO stretch	
1161sp	1162	-	Ethylene Carbonate
	1152	CO stretch	Ethyl-CO_3Li
1072sp	1074	-	Ethylene Carbonate
	1085	CO stretch	Ethyl-CO_3Li
	1100	CO stretch	$(CH_2OLi)_2$
1017sp	1021	-	Diethyl Carbonate
	1010	CO stretch	Ethyl-CO_3Li
973m	974		Ethylene Carbonate
903sh	890		$(CH_2OLi)_2$
844sp	858	-	Diethyl Carbonate
	826	CO_3 bend	Ethyl-CO_3Li
	850	-	LiOH
774sp	774	-	Ethylene Carbonate
730sh	738		
717m	720	CO_2 asym. bend	Ethyl-CO_3Li
666w	660-550	LiO stretch	$LiOCH_3$
556sp	500-600	LiO stretch	Ethyl-CO_3Li
529w	400-500		LiOH
-	-		

The IR spectrum of the film formed on the surface of graphite anode during lithium intercalation in PC-$LiPF_6$ solution is shown in Figure I.5.15. The IR spectrum is rich in by- product of the PC decomposition. The IR signals of Li_2CO_3, around 850 and 1460 cm^{-1} have also been observed. The film formed in this case is much thicker than the

film formed when EC was used. This indicates that the film formed from decomposition of PC is not very protective and further electrolyte decomposition may proceed.

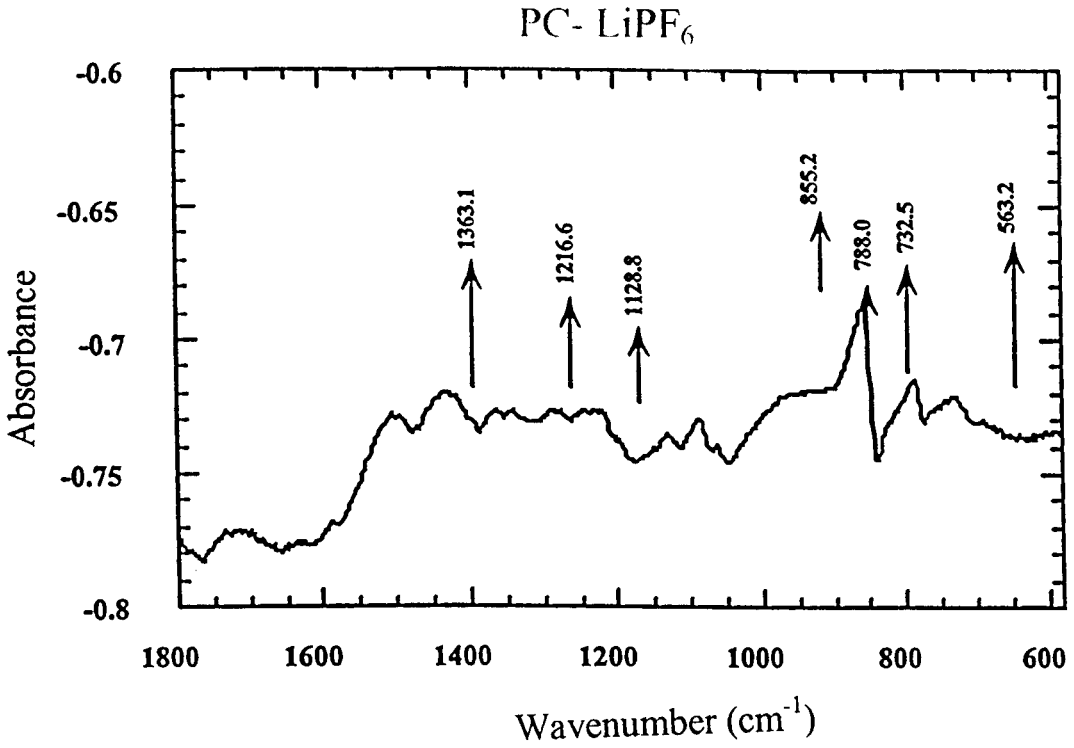

Figure I.5.15: IR spectrum of film formed on graphite anode during the first lithium intercalation process in PC-1M $LiPF_6$.

Table I.5.6: Vibrational frequencies on the surface layer on graphite in PC-$LiPF_6$

ν observed (cm^{-1})	ν assigned	Assignment bands	Compounds
1862sh			
1817sp		-	
1785sh	1760	-	Dimethyl Carbonate
1732w		-	
1715br		-	
1630w	1629	-	$LiPF_6$*
1588sh	1580	-	RCOOLi
1500br		-	
1430br	1441	-	Li_2CO_3
1360br		CO_2 sym. stretch	
1338br		-	
1289br	1280	-	Dimethyl Carbonate
1250w	1263	-	$LiPF_6$*
1233w		-	
1134m	1122	-	$LiPF_6$
1088m	1089	CO stretch	Li_2CO_3
	1083	-	$LiPF_6$*
1065w	1060	-	Li_2O
960w	969-914	-	Dimethyl Carbonate
865sp	866	CO_3 bend	Li_2CO_3
	832	-	$LiPF_6$*
	870	-	Li_2O
	866	-	LiO
791sp	793	-	Dimethyl Carbonate
	789-745	-	LiO
734br	738	CO_2 asym. bend	Li_2CO_3
691sh	730-689	-	LiO
562sp	557	-	$LiPF_6$*
	650-550	LiO stretch	$LiOCH_3$

The IR spectrum of film formed on the surface of lithiated graphite in PC-DMC-$LiPF_6$ is shown in Figure. I.5.16. The film formed with electrolyte containing PC was always thicker and richer in PC decomposition by-product. It is also observed that film formed from solution containing EC solvent is also rich in EC decomposition by-products.

The IR spectra of surface films formed on lithiated graphite anodes in solutions containing both the cyclic and the linear carbonates have been studied. The composition of the film is dominated by the decomposition by-product of the cyclic carbonate. This observation may suggest that the cyclic carbonates that selectively solvate the Li^+ in the

electrolyte, carry its solvation shell to the graphite surface, and preferentially saturate the electrode-electrolyte interface with the cyclic carbonate. This observation may explain the beneficial effect of EC in commercial electrolyte for lithium batteries.

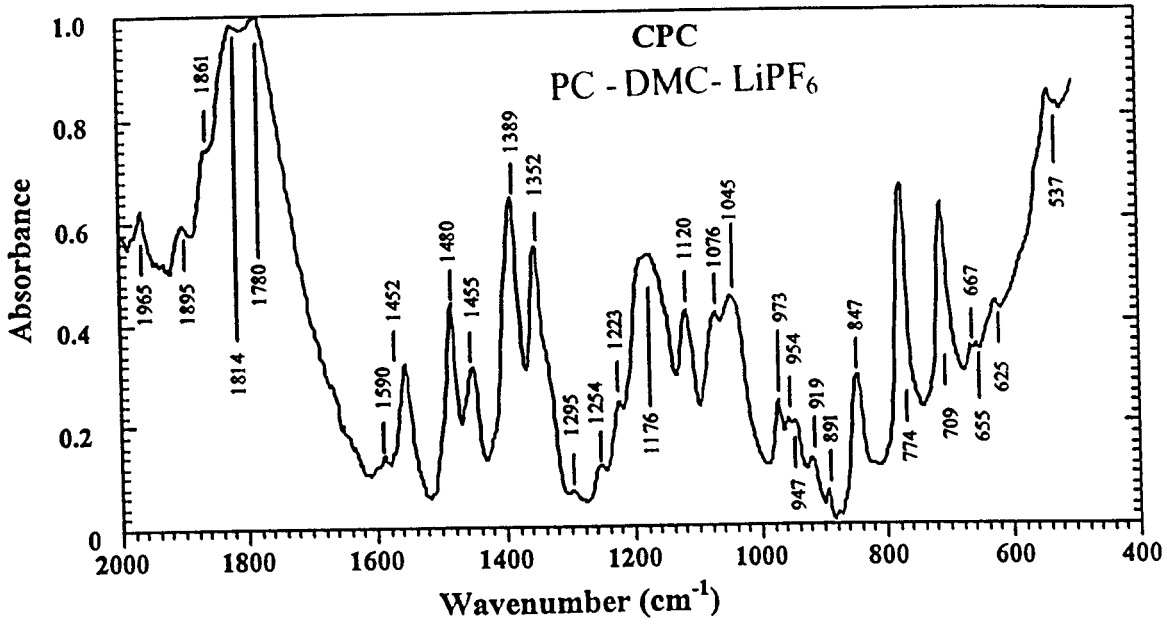

Figure I.5.16: IR spectrum of film formed on the surface of graphite anode during lithium intercalation in PC-DMC (1:1mol) + 1M $LiPF_6$.

Table.I.5.7: IR frequencies of the surface layer on cycled CPC in PC-DMC-$LiPF_6$

v observed (cm^{-1})	v assigned	Assignment bands	Compounds
1965m			
1895m			
1861sh	1750-1870	-	Organic Carbonate
1780br	1760	-	Dimethyl Carbonate
1590w	1630-1590	-	Carbonate ion
1555sp	1580	-	RCOOLi
1480sp	1480-1450	CH bend	$LiOCH_3$
1455sp	1450-1480	CH bend	$LiOCH_3$
	1441	-	Li_2CO_3
1389sp	1380-1360	CH bend	$LiOCH_3$
1352sp		-	
1295sh		-	
1254w	1250-1280	-	Organic Carbonate
1223w		-	
1176br	1170-1150	CH stretch	$LiOCH_3$
1120sp		-	
1076w	1070-1050	CH stretch	$LiOCH_3$
	1089	CO stretch	Li_2CO_3
1045br		-	
973sp	970-1020	-	Organic Carbonate
891sp	866	CO_3 bend	Li_2CO_3
847sp	826	CO_3 bend	Ethy-CO_3Li
	846	CO_3 bend	Li_2CO_3
774sp	774-793	CO_2 asym. bend	Organic Carbonate
709sp	720	CO_2 asym. bend	Ethy-CO_3Li
625w	550-650	LiO stretch	$LiOCH_3$
537w	529	CO bend	

(w : weak , m : medium, s : strong , sh : shoulder, br : broad, v : very, sp : sharp)

I.5.6. Thermal analysis of SEI layer on graphite anodes

The thermal characteristics of the surface film formed on the graphite anode during lithium intercalation are very important for practical reasons [162]. The lithium battery may be subject to the different thermal conditions during its operational life. Therefore its thermal safety characteristics must be known. In this work, the thermal property of films formed on graphite anode has been studied using differential scanning calorimetry (DSC). The graphite electrode was charged and discharged in carbonate-based electrolytes, and the surface film formed on the anode was collected for DCS study. The surface layers were placed inside a hermetically sealed stainless steel DSC pan inside a dry box and transferred to the DSC system. Figure I.5.17 shows the thermal behavior of the surface film in contact with Li_xC_6, (x= 0.2, 0.4, 0.6, 0.8, 1.0).

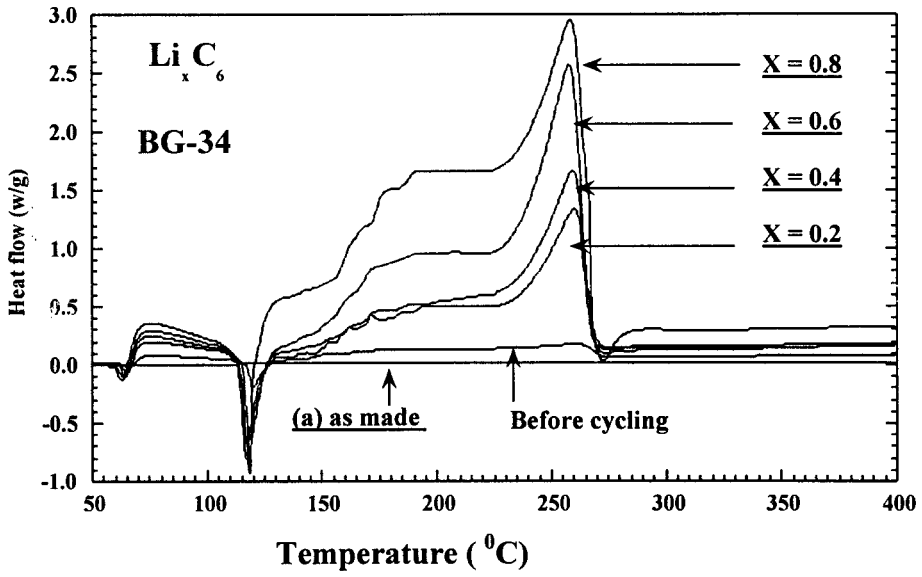

Figure I.5.17: Differential scanning calorimetry of surface film formed on graphite anode at different states of charge. (X=0.2-0.8)

The sample has an endothermic peak near the boiling point of DMC, and then the exothermic process starts around 150 °C. A major exotherm was observed at 220-240°C. The intensity of the exotherm peak correlates well with the amount of lithium remaining in the graphite. It is very important to stress the safety aspects of the Li-ion cells when they are exposed to temperatures above 150°C. Further electrolyte decomposition with massive gas generation may occur above 150°C, and cell temperature may rise to above the flash point of the electrolyte components. Therefore care should be exercised dealing with lithium-ion batteries with graphitic anodes, particularly in the charged state (x value close to one in Li_xC_6).

A similar thermal behavior was observed for almost all graphitic anodes. The temperature- induced degradation of the SEI layers occurs first around 120-140°C

followed by an exothermic reaction and the decomposition of trapped $LiPF_6$ around 210-230° C. We have found a direct correlation between the BET surface area of the graphite anode, amplitude of the DSC exothermic peak and the irreversible capacity losses measured for C/Li cells. Figure I.5.18 shows the correlation between the volume of gas generated on the surface of lithiated graphite anodes and the surface area of the graphite material used.

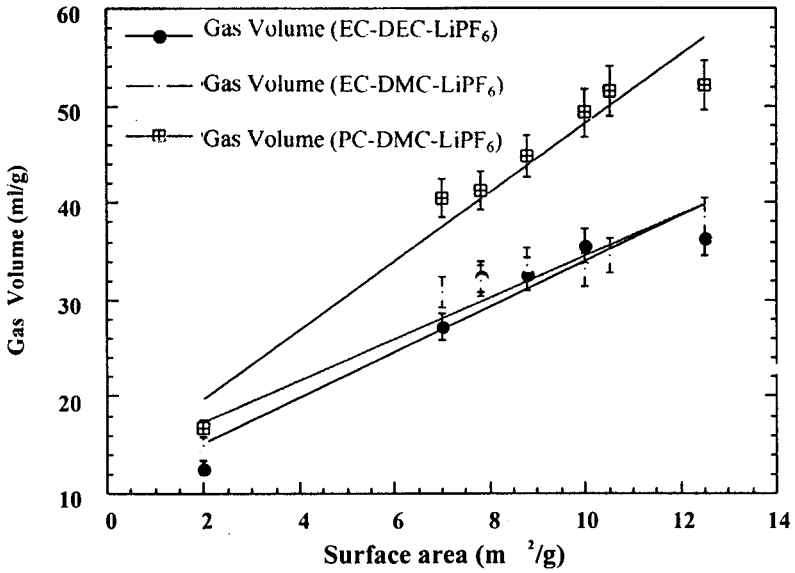

Figure I.5.18: The correlation between the volumes of gas evolved during lithium intercalation in graphite anode and the surface area of the graphite.

I.5.7. General conclusions

The following general conclusions can be made from this study.

1. Organic carbonates are not electrochemically stable over a lithiated graphite electrode. However, the decomposition by-products formed on the surface can

protect the electrode and the electrolyte decomposition is eliminated in subsequent charge-discharge of cycles.

2. The nature of film formed on the surface of lithiated graphite depends on the composition of electrolyte, and in the case of electrolyte made of organic carbonates, the by-products are organo-lithum compounds as well as some lithium carbonate.
3. The composition of the film is dominated by the by-product of cyclic carbonate decomposition, and less by the linear carbonate decomposition.
4. The film formed from the decomposition of cyclic ethylene carbonate is denser and more protective as compared with films formed from other carbonates.
5. The gaseous species formed during the first charge discharge are mostly flammable and care should be taken when preparing large lithium cells.
6. The thermal analysis has shown that the film formed on the surface of lithiated graphite is not stable above 150 °C. If lithium cells are exposed to heat, or if internal heat exceeds 150 °C, the protective film could be destroyed and further electrolyte decomposition of the freshly exposed surface of lithiated graphite may occur. Therefore, it can be concluded that the current lithium-ion cells are not very safe above 150 °C, and their application in such conditions must be avoided. In addition, a safer and more robust anode is needed, particularly for large size applications of high-energy and high-power lithium batteries.

PART II

Electrochemical, Spectroscopic, Thermal, and Structural Analysis of Polyaromatic Compounds

Chapter 6

ELECTROCHEMICAL AND THERMAL ANALYSIS OF POLYAROMATIC COMPOUNDS

II.6.1. ELECTROCHEMISTRY OF POLYAROMATIC COMPOUNDS

II.6.1.1. INTRODUCTION

Polyaromatic molecules are the basis for molecular semiconductors. Their physico-chemical properties are well correlated to their structure and the number of π electrons [163-172]. Polyacetylene, perylene, and phthalocyanines are good examples of this class of compound. Graphite with polycyclic graphene layers can also be considered as the ultimate element of the aromatic polycyclics with layers arranged in a hexagonal structure with 0.3353 nm separation between the layers and 0.1421 nm for the C-C bond distance within the layer. The polyaromatic compounds with extend π electrons have shown strong cooperative properties depending on the details of stacking in the solid-state. Their properties in crystals may vary markedly from their single molecule behavior. As discussed in Chapter 3, the dispersion forces in this class of compounds are strong and dominating. The dispersion energy between molecules with polarizable π electrons is the main cause of molecular aggregation. This phenomenon is often observed in thin-film polyaromatics, and is currently the focus of many research groups [162-164]. The dispersion energy is short range ($1/r^6$) and strongly depends on the polarizability (α^2) and the ionization potential (I_p) of the molecule, as described in Chapter 3 [40].

$$U_{dispersion} = -(\alpha^2.I_p)/4r^6 \qquad (I.3.8)$$

The physical properties of polyaromatics correlate well with the number of π electrons in the system according to the following equation [173].

$$E_{parameter} = a + bK^n \qquad (II.6.1)$$

where $E_{parameter}$ is the energy parameter such as ionization potential, IP, electron affinity, $A_{affinity}$, a, b, and k are constants and n is the number of π electrons. Table II.6.1 shows the value of energy parameters of some members of polyaromatic molecules.

Table II.6.1: Energy parameters of various aromatic polycyclics [173-175].

Molecules	IP_{gas}	$IP_{solid\text{-}state}$	$A_{affinity\text{-}gas}$	E_{gap}(eV)
Benzene	9.2		-1.4	6.0
Naphthalene	8.1	6.8	-0.2	5.0
Anthracene	7.4	5.75	0.61	3.9
Tetracene	6.9	5.40	0.8	2.8
Pentacene	6.55	5.04	1.2	2.2

Many aromatic polycyclics have been studied for their application in solar cells, including polymerized naphthalene [174], perylene [175], coronecene [176], aneracene [177], tetracene [178] pentacene [179], tetrathiotetracene [180], p-quaterphenyl [181], dibenzothiophene [182], and other polyacenes [183].

When a polyaromatic molecule absorbs photon energy, it goes to an electronically excited state, and the stored energy in the excited state molecules can be used to do work. Currently the efficiency of organic-based solar cell is low, but there have been steady improvements during the last decade.

Polyaromatic diimides have been used as electron acceptors in many fundamental studies of photo induced electron-transfer including photosynthesis [184], solar energy conversion [185], molecular electronics [186], electrochromic devices and photorefractive materials [187, 188]. These molecules have been widely used in electron-transfer studies because they undergo reversible one- electron reduction at modest potentials to form stable radical anions.

Perylene derivatives, with their promising electroactive and photoactive properties have attracted much attention for potential applications in organic molecular electronics [189-191], and are of particular interest for use in light emitting materials for the fabrication of electroluminescent display devices [192-195].

The perylenedicarboximide derivatives form classes of organic dyes. They are chemically and thermally stable and, as such, are being investigated as potential active components in xerography, photography, electroluminescance and molecular electronics [155]. The redox potential of these molecules are especially valuable for selecting materials for different applications such as the photogeneration of H_2 and O_2 from water or the generation of electricity in dye sensitized solar cell. Although the ionization potential of these molecules can be measured in the gas phase by UV – photon electron spectroscopy, the electrochemical oxidation – reduction potentials, that may be correlated to the HOMO – LUMO of the molecule, can be measured using cyclic voltammetry

techniques. The perylenetetracarboxylic di-anhydride molecule (PTCDA) shown in Figure II.6.1 is the central moiety to a large family of PTCD derivatives.

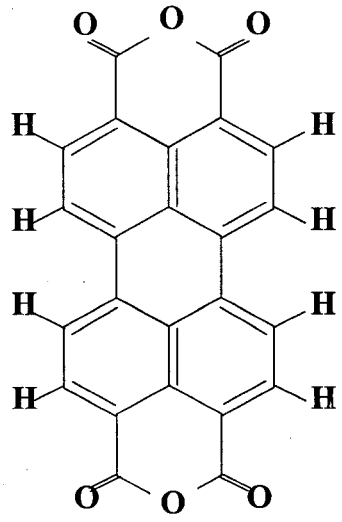

Figure II.6.1: Structure of perylenetetracarboxylic dianhydride (PTCDA)

A number of theoretical reports on the electronic properties of PTCDA and related aromatic moieties have been reported in the past [164-166]. Of the various PTCD materials, a great deal of work has been focused on the growth of thin solid films of 3,4,9,10-perylene tetracarboxylic dianhydride (PTCDA) [166-171]. For instance, Armstrong et al. [170] have grown ultra thin films of PTCDA and N,N=-di-n-butyl-perylene-3,4,9,10-bis(dicarboximide) on (001) alkali halide surfaces and Bohninger et al. [171] have reported the images of PTCDA on Ag(110) using STM. A theoretical study of a perylene derivative on gold (111) has also been reported [172]. It has been demonstrated that PTCDA molecules exhibit intermolecular electronic interactions that allow it to be grown in thin films with an extended electronic structure. It is also known that PTCDA molecules in very dilute solutions (<1μM) already exist in aggregated form

and show strong absorption and fluorescence due to the extended electronic structure of the aggregates [196]. The extended electronic structure of the perylene leads to high carrier mobility and high conductivity. In addition, due to the highly extended electronic interaction, high quality thin films of these organic molecules can be formed. An epitaxial layer of PTCDA on naphthalene-tetracarboxylanhydride (NTCDA) has shown a quantum well effect in alternating layers. The quantum confinement effects have been observed for several polyaromatic thin films of 10 to 500 Å thick.

The energy parameters and thermal stability of polyaromatics are important in determining their potential applications. A convenient way to study the energy parameters and electronic properties of polyaromatics molecules is to determine their redox potential with respect to a well-defined reference electrode. The electrochemical redox potential that corresponds approximately to the HOMO-LUMO energies can be measured using a cyclic voltammetry technique. The $E_{1/2}^{red}$ and $E_{1/2}^{ox}$ potentials approximately related to the ionization potential (IP), and the electron affinity ($A_{affinity}$) of the compounds respectively. The cyclic voltammetry method provides information about the energy of the oxidized and reduced state of molecules. During oxidation, the electron is transferred from the highest occupied molecular orbital (HOMO) to the electrode, hence the oxidation potential approximately corresponds to the energy of the filled orbital in the molecule. The reduction potential is also approximately related to the energy of electron transfer from the electrode to the lowest unoccupied molecular orbital (LUMO) of the sample.

In this work electrochemical properties of various polyaromatics compounds have been studied using cyclic voltammetry in a nonaqueous electrolyte. The half potentials, $E_{1/2}$ of some of the polyaromatics studied in this work are tabulated vs. saturated calomel electrode.

The important oxidation-reduction properties of PTCDA and related molecules are not well known and there are only a few data published in the literature [197] A systematic study of the redox potentials of PTCD derivatives, as determined by cyclic voltammetry, was the objective of the present work in our group, similar to our previous studies on phthalocyanines [198]. A new carbon paste micro-electrode technique was used to investigate the electrochemical properties of perylenetetracarboxylic derivatives since the materials are virtually insoluble in most organic solvents. Although a carbon paste electrode technique has been used in the past, the technique was previously utilized to investigate the electrochemical capacitance of high surface area carbon and to determine properties of solution species [199-202]. Further, the carbon paste technique was previously directed toward the development of the double-layer capacitors and investigation of the capacitive current due to the double-layer charging of highly conductive carbon [203]. Capacitance of the electrode was estimated from $C = i/A\nu$, where i is current, A is surface area and ν is the sweep rate (in mV/sec). Madec and Courtot-Coupez have studied the effect of various electrolytes on the redox potential of polynuclear aromatic molecules [197], and they found that the redox potential in this class of compounds is solvent independent, and they suggested that their redox potential can be used as reference potential. Kojima et al. [195] have investigated the

electroluminescence of perylene-doped organic materials and they found that, upon doping, the electron-hole carrier transport was improved over one order of magnitude. Although the carbon paste technique is used often in the field of supercapacitors for analysis of high surface area conductive carbons, in this work we developed a new carbon paste micro-electrode for investigation of redox behavior of insoluble organic solids such as PTCDA. In this study, a new procedure to prepare carbon paste micro-electrodes is developed. In this procedure the electrode contains composite of active material (PTCDA) within the matrix of conductive carbon that allows study of the electrochemical properties of organic solids.

II.6.2. EXPERIMENTAL

II.6.2.1. Cyclic voltammetry

The three - electrode cell consisting of the carbon micro-electrode coated with sample as the working electrode, platinum mesh (2x2 cm^2) as the auxiliary electrode, and the saturated calomel electrode (SCE) as the reference electrode, was used. The cell configuration with three electrodes is shown in Figure I.2.1. The cell geometry and electrode design allow to place the tip of the reference electrode very close to the working electrode to minimize the solution resistance, hence reducing the IR-drop during cyclic voltammetry.

II.6.2.2. Electrode preparation:

The working electrode is a microelectrode, (from Bioanalytical Systems). The electrode surface area was 0.018 cm^2. The working electrode was polished before each

experiment with 0.1μ alumina powder and washed and rinsed with distilled water and dried under vacuum at 100^0C. The polished electrode was stored inside of a dry box filled with high purity (99.999%) Argon ready for coating with the sample. Samples, PTCDA , Thio-PTCD, and other PTCD derivatives (ca. 80w%) were mixed with conductive carbon black (15w%) and 5w% EPDM (ethylene propylene diene monomer) binder that was dissolved in xylene solvent (5 w%). The mixture was then ground to form an ink-type slurry. A small drop of this ink slurry was placed on the tip of the microelectrode and dried (overnight) under vacuum at 100°C. The carbon-paste microelectrode was used as the working electrode. The electrolyte was prepared from ultra-pure acetonitrile containing anhydrous 1M $LiClO_4$.

The BAS 100B/W electrochemical workstation, which is a microprocessor-base electrochemical analyzer, was used in this work. The BAS electrochemical workstation is driven by electrochemical software capable of scanning the electrode potential vs. reference electrode in a controlled way while the current response can be measured. This method of cyclic voltammetry was used to study redox behavior of polyaromatic materials. The cyclic voltammetry of the samples were performed between -1500 and 1500 mV vs. SCE. The scan rates were chosen from 2 mV/sec up to 200 mV/sec. Cyclic voltammetry of ferrocene was study to calibrate the electrochemical oxidation potential and the performance of the cell. The cyclic voltammogram of ferrocene in acetonitrile + 1M $LiClO_4$ is shown in Figure II.6.2.

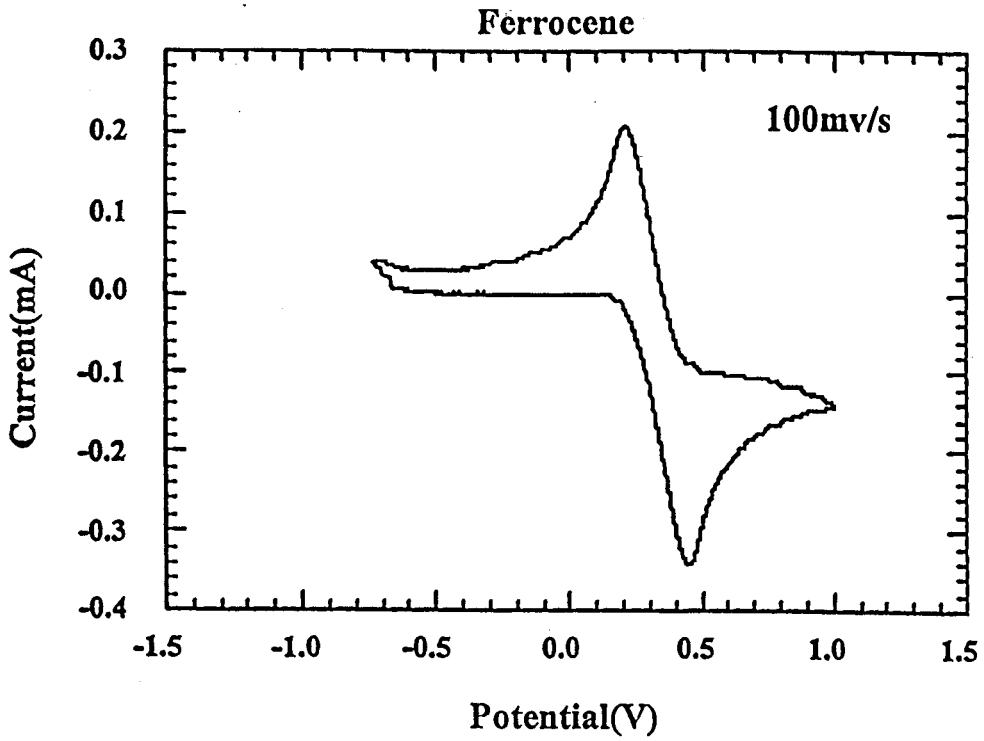

Figure II.6.2: Cyclic voltammogram of ferrocene $Fe(C5H5)_2$ in acetonitrile + 1M $LiClO_4$ used to calibrate the electrochemical set-up.

When the voltage of the electrode is scanned from zero to positive value, the ferrocene molecules oxidize and electrons are transferred from the ferrocene molecules to the electrode. The current reaches a maximum when the majority of the ferrocene on the surface of the electrode is oxidized. The maximum current obtained is called the anodic peak current, I_p^a, and the voltage of electrode at I_p^a is called the anodic peak potential, E^a_p. When the voltage of the electrode is scanned back, the oxidized ferrocene, $[Fe(C_5H_5)_2]^+$ is reduced to its neutral state, $Fe(C_5H_5)_2$ and the current again reaches a maximum when the majority of the $[Fe(C_5H_5)_2]^+$ on the electrode surface is reduced. The

maximum current for reduction is called the cathodic peak current, I_p^c, and the potential for at I_p^c is called the cathodic peak potential, E^c_p. For an ideal reversible reaction the I_p^c/I_p^a = cathodic 1, and peak separation is $\Delta E_p = E^c_p - E^a_p = 59$ mV/n, where n is the number of electrons involved in the oxidation-reduction process. The half potential, $E_{1/2}$, for reversible oxidation reaction is defined as;

$$E_{1/2} = (E_p^a - E_p^c) \qquad \text{(II.6.2)}$$

The $E_{1/2}$ of ferrocene and the shape of the oxidation-reduction curves indicate a reversible redox process. This test shows that our electrochemical cell is working well. The position of the reference electrode tip was carefully placed very close to the working electrode, 1-2 mm, to avoid a major IR drop in the solution during fast voltage scans. The synthesis (by Dr. James Duff from the Xerox Research Center of Canada) and structural characterization of PTCD materials (except the PTCDA compound) have been previously reported using Raman spectroscopy [199-202,205].

II.6.3. RESULTS AND DISCUSSIONS

The experimental value for HOMO of PTCDA have bean measured to be 8.22 eV [206], which is 1 eV different from the calculated value. The correlation of IP with oxidation potential for a large series of organic dyes has resulted in the following empirical equation [207,208],

$$IP_{exp} \simeq IP_{oxidation\ potential} \sim 0.6941\ E_{[HOMO]} + 1.9049. \qquad \text{(II.6.3)}$$

The rational for equating the IP with oxidation potential has been discussed in the past [207]. However, the relationship developed best represents molecules with similar structures. The following approximate equations also have been developed to correlate

the oxidation potential with that of the electron affinity $A_{affinity}$ [207] and the ionization potential IP of molecules [209].

$$A_{electron\ affinity} \simeq E_{1/2}^{red} + 4.3 \qquad \text{(II.6.4)}$$

$$IP \simeq E_{1/2}^{ox} + 4.3 \qquad \text{(II.6.5)}$$

Where the $E_{1/2}^{red}$ is the reduction potential, and $E_{1/2}^{ox}$ is the oxidation potential in volts, versus the saturated calomel electrode (SCE). The constant 4.3 includes the free energy change between an electron in the SCE and the same electron in vacuum.

A series of cyclic voltammograms of PTCDA obtained for scan rates varying from 5 mV/s up to 200 mV/s are shown in Figure II.6.3.

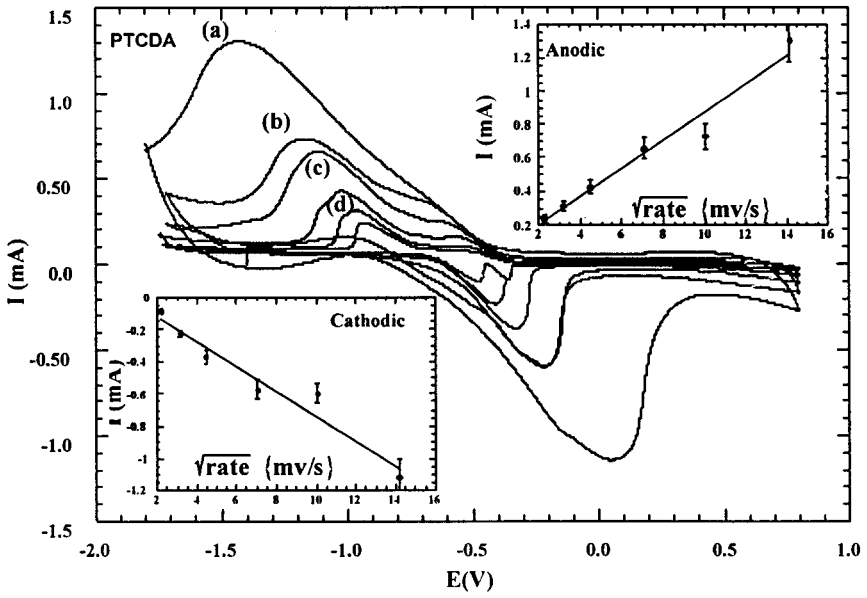

Figure II.6.3: Cyclic voltammograms for PTCDA at various scan rates. The trace a) corresponds to a scan rate of 200 mV/s, b) 100 mV/sec, c) 50 mV/sec, d) 20 mV/sec, and the two lower current voltammorgams are recorded for 5 and 2 mV/sec scan rates. The insets show plot of the anodic and the cathodic peak currents vs. the square root of the scan rates.

A well resolved oxidation-reduction peaks are observed with similar I_p^a and I_p^c, indicating a reversible oxidation-reduction process. The reduction of PTCDA forms an anion, and the radical anion oxidizes to a neutral state during oxidation. This redox process can be illustrated as:

$$A + e^- \rightarrow A^- \text{ (reduction)}$$

and

$$A^- \rightarrow A + e^- \text{ (oxidation)}$$

The anodic and cathodic peak currents increases linearly versus square root of sweep rate ($\nu^{1/2}$), indicating that the reaction is a diffusion controlled process.

Similar trends were obtained for cyclic voltammograms of the thio-PTCD molecule as shown in Figure II.6.4. However, the anodic and cathodic peaks are splited in two peaks with about 150-200 mV peak separation. At negative potentials, two pairs of reversible reduction/oxidation peaks were obtained. The oxidation and the reduction peak potential are more positive compared to that of the PTCDA. The reduction potential is at least 100 mV more positive and the oxidation peak is about 300 mV more positive for the 100 mV/sec scan rate. This indicates that it is more difficult to oxidize the thio-PTCDA and the PTCDA itself. At the cathodic potential, the reduction of the thio-PTCDA occurs and the anion is formed. The anions which are formed are stable to be observeed during reverse potential scan to anodic region. This is a general characteristic of most polyaromatics, that they form stable anions.

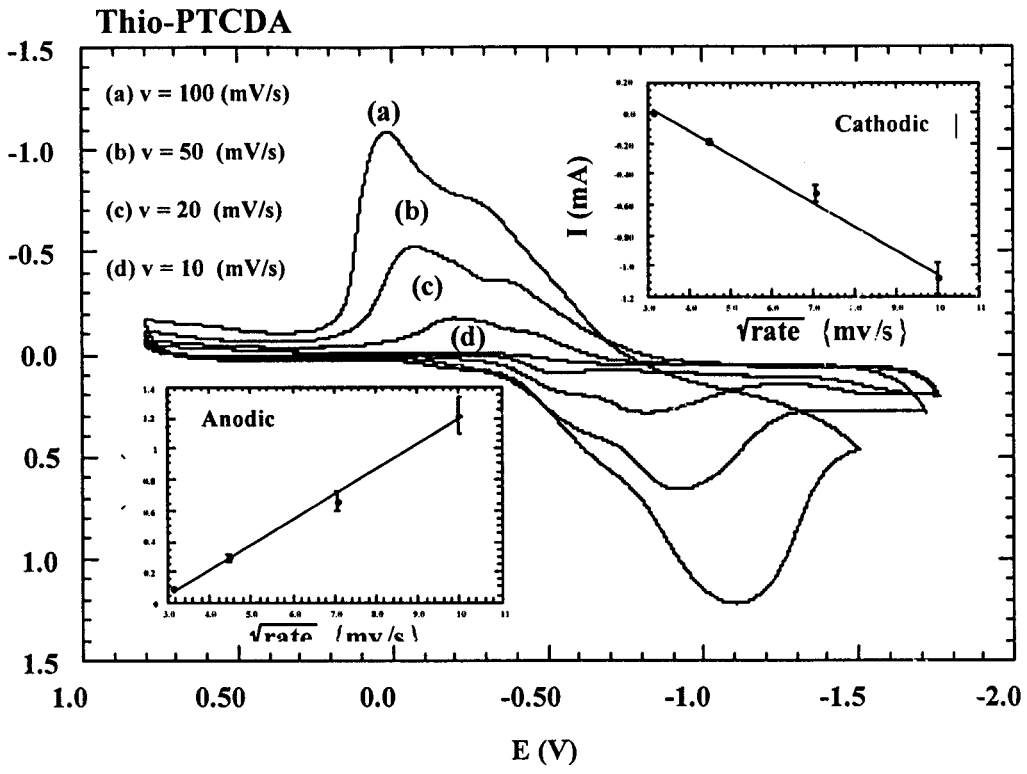

Figure II.6.4: Cyclic voltammograms for thio-PTCDA at various scan rates. The trace a) corresponds to a scan rate of 100 mV/sec. The inset shows a plot of the anodic and the cathodic peak currents vs. the square root of the scan rate.

The radical anion which is formed during reduction process is stable and can be oxidized in reverse potential scans. The shift in the peak potential with the scan rate is clearly observed and is expected because of the capacitive effect during fast scan rates. In the insets, it is also shown that the anodic and the cathodic peak current are proportional to the square root of the scan rate, an indication of a diffusion controlled charge-transport process. Note that for a quasi-reversible process, the current is not proportional to the square root of the scan rate [209]. At low scan rates (5 mV/s) the CV shows splitting of the redox peaks which is a clear sign of multistep charge transfer

processes. The presence of at least two distinct peaks in the CV of the PTCD series is evident for the materials studied.

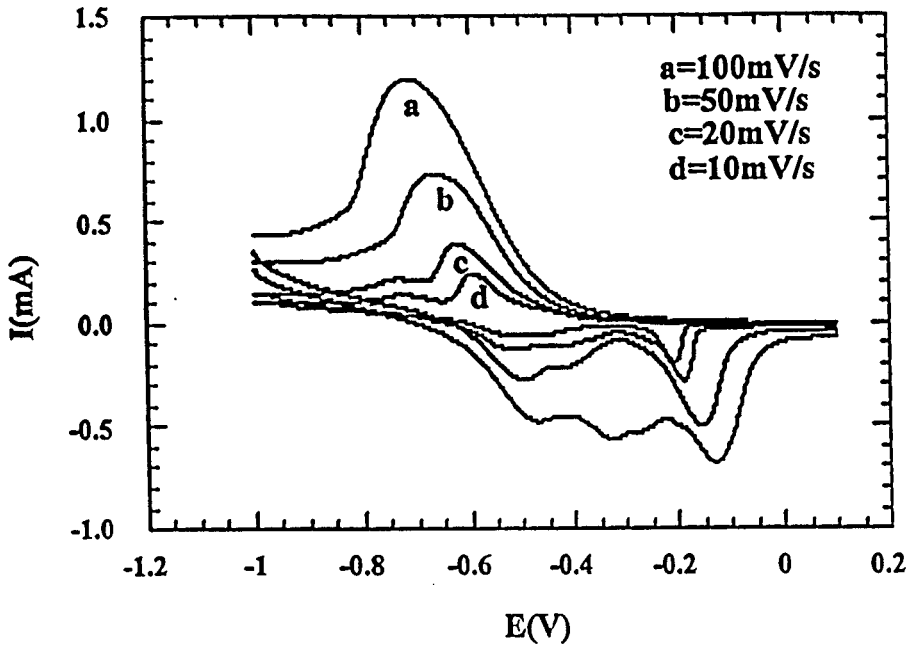

Figure II.6.5: Cyclic voltammograms for bis-(3-fluorobenzylimido)perylene SR2 at various scan rates.

The cyclic voltammogram of the bis-(3-fluorobenzylimido)perylene is shown in Figure II.6.5. A reduction peak below –0.5 V vs. SCE and an oxidation peak above –0.3 V have been observed. The smaller peak separation as compared with PTCDA and Thio-PTCD indicate a more facile oxidation - reduction process for the bis-(3-fluorobenzylimido)perylene. The mechanism of oxidation – reduction process follows a diffusion-controlled process since the anodic and cathodic peak currents are linearly dependent on the square root of sweep rate.

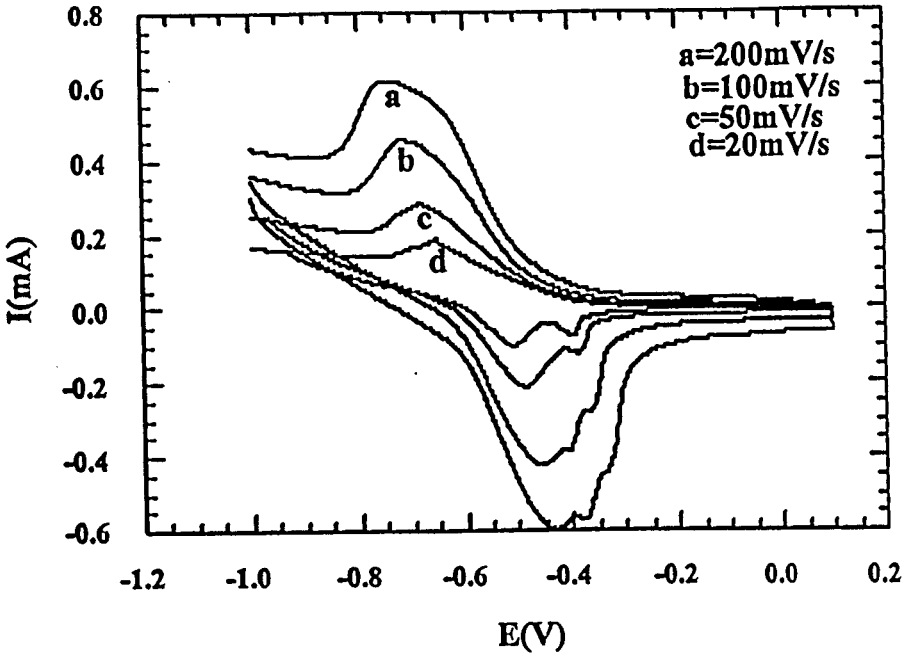

Figure II.6.6: Cyclic voltammograms for bis-(2,6-difluorobenzylimido)perylene SR4 at various scan rates.

The cyclic voltammogram of the bis-(2,6 difluorobenzylimido)perylene SR4 is shown in Figure II.6.6. Very reversible oxidation-reduction peaks are obtained. The peak separation for oxidation and reduction reactions is much smaller than the case for PTCDA and Thio-PTCDA. Therefore it can be concluded that the oxidation-reduction of the bis-(2,6 difluorobenzylimido)perylene SR4 is very facile and fast. The switching energy between the reduced form to oxidized form of this molecule is small. This may suggest that bis-(2,6 difluorobenzylimido)perylene SR4 compound is a suitable system for switching devices such as electrochromic displays.

A very reversible reduction – oxidation process also was observed for the bis-(3,4-dichlorobenzylimido)perylene SR6, Figure II.6.7. The peak separation between the reduction and oxidation reaction is only about 120 mV for the 20 mV/sec scan rate.

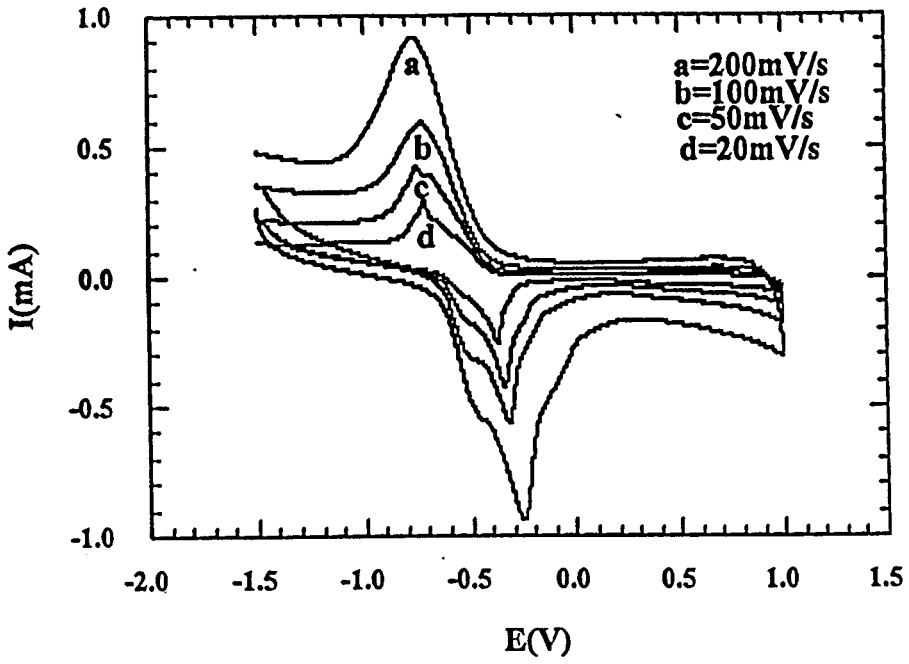

Figure II.6.7: Cyclic voltammograms for bis-(3,4- dichlorobenzylimido)perylene SR6 at various scan rates.

The cyclic voltammogram of bis-(3,5-dichlorobenzylimido)perylene SR7 is shown in Figure II.6.8. Similar to the other molecule in SR-series, a reversible peak with small peak separation is observed. A general conclusions can be made, that the SR-series are excellent switching molecules and they may find applications in devices that may require significant switching cycles during the life of the device, such as solar cells and display devices.

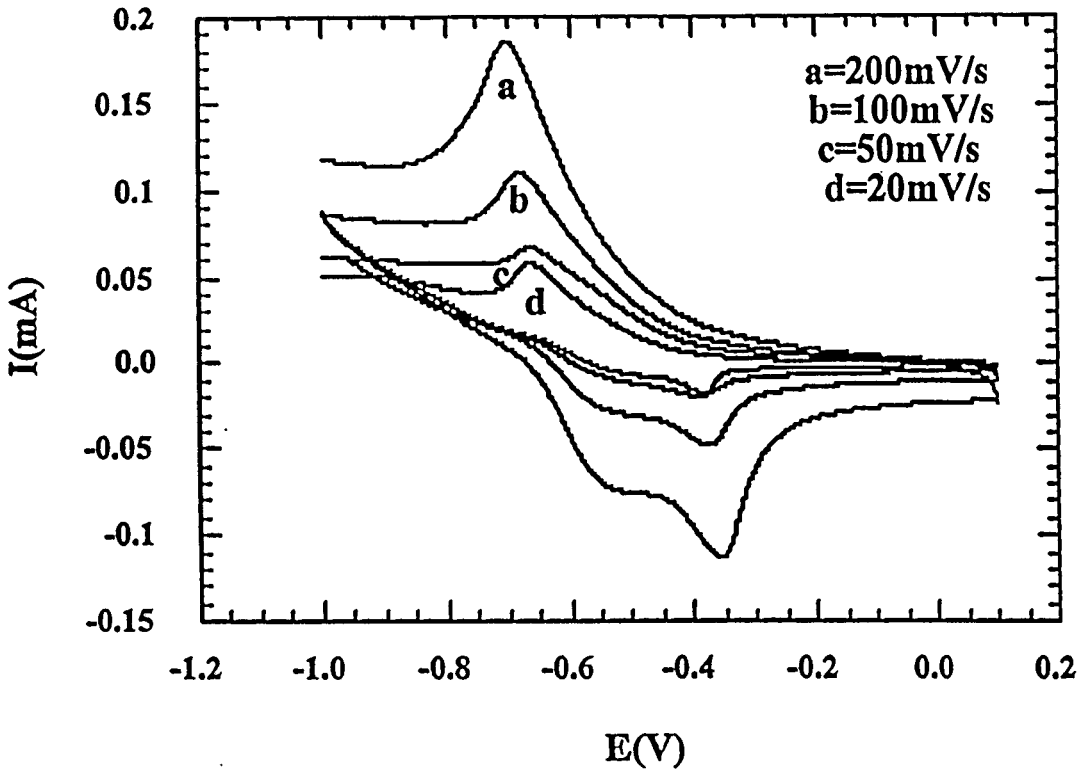

Figure II.6.8: Cyclic voltammograms for bis-(3,5-dichlorobenzylimido)perylene SR7 at various scan rates.

Cyclic voltammorgam of bis(phnethylimido)perylene is shown in Figure II.6.9. Below –0.1 V two peaks for oxidation and reduction are observed. The reactions are reversible and the intensity of the oxidation and reduction peaks are almost the same. The linear correlation of peak current versus the square root of scan rates indicates that the oxidation-reduction process is a diffusion-controlled process.

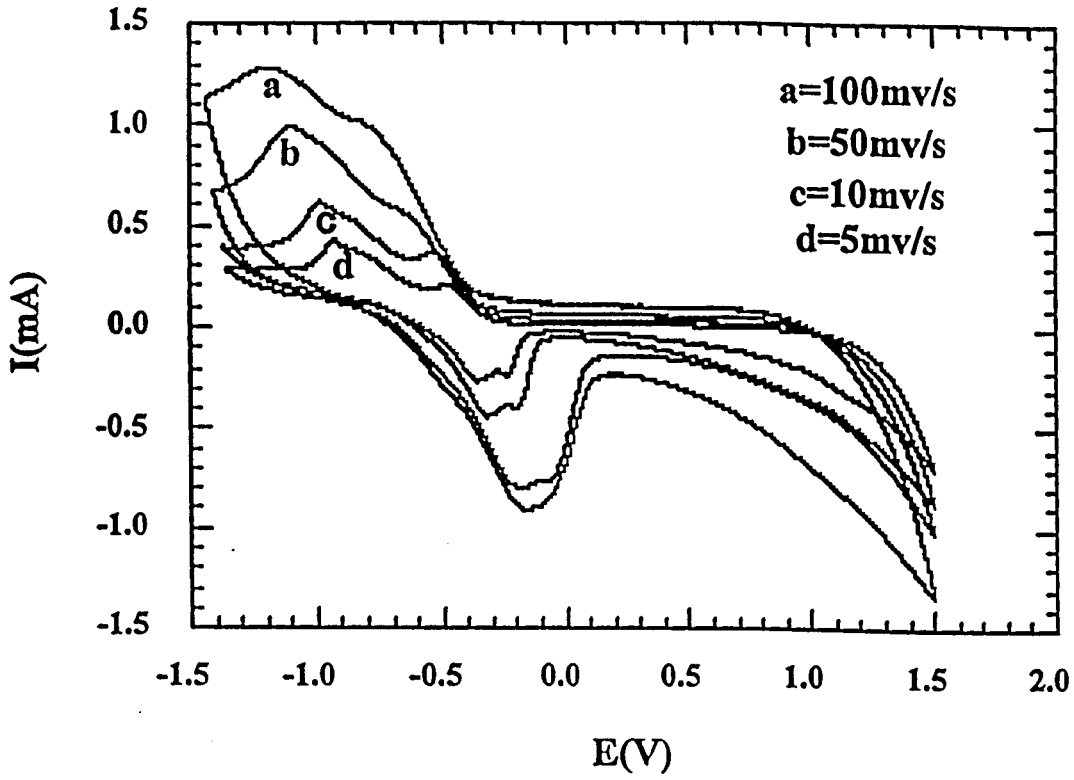

Figure II.6.9: Cyclic voltammogram of bis(phnethylimido)perylene.

The oxidation-reduction peaks for various PTCD derivatives for scan rate 100 mV/sec are listed in Table II.6.2. The first three compounds in Table II.6.2 have a molecular structure containing one perylenetetracarboxylic group. However, the second group of materials (contains three members of a new series of materials has two perylene tetracarboxylic (PTC) groups that are attached to the ends of a propane molecule.

Table II.6.2: Oxidation and reduction potentials of PTCD derivatives determined by cyclic voltammetry

Molecule	E^{ox} (V)	E^{red}(V)	Scan(mV/s)
PTCDA	-0.104	-1.39	100
Thio-PTCD	0.0	-1.1	100
Bis-(3-fluorobenzylimido)Perylene SR2	-0.130	-0.710	100
Bis-(2,6 difluorobenzylimido)Perylene SR4	-0.353	-0.697	100
Bis-(3,4 dichlorobenzylimido)Perylene SR6	-0.317	-0.715	100
Bis-(3,5dichlorobenzylimido)Perylene SR7	-0.353	-0.697	100

The electrochemical behaviour is, as can be seen in Table II.6.2, quite similar, indicating that the electrochemical properties of these materials are controlled by the chromophore (PTC) moiety. Similar correlations have been observed for the electronic spectra of these materials. However, there are some differences. In particular, the effect of the aromatic substitution in bis(phnethylimido)perylene is to bring the electrochemical behavior of this material closer to that of the series where there are two perylene tetracarboxylic (PTC) groups.

In summary, in this work we have shown for the first time the redox behavior of PTCDA derivatives containing one and two perylene moieties. The compounds with more than one perylene moiety and the SR-series have shown a more favorable switching between the reduced and oxidized states and with smaller peak separation between the reduction and the oxidation reactions. It is also shown that carbon paste micro-electrode

developed in this work is an appropriate experimental technique for studying the cyclic voltammetry of highly insoluble organic dyes and pigments in a nonaqueous electrolyte.

II.6.4. Thermal stability: differential scanning calorimetry (DSC) of polyaromatic compounds

Differential scanning calorimetry (DSC) was carried out using a PERKIN ELMER DSC-7 model. A hermetically sealed stainless steel pan was used for thermal analysis. DSC measurements were carried out under flow of Argon gas, and at a heating rate of 5°C/min from ambient temperature to 400°C. The analysis time was approximately 80 min, including 2 minutes of isothermal recording at the initial and final temperatures. Between analyses, 30 minutes were allowed for the surrounding enclosure to return to its original temperature distribution.

The DSC measurements were performed for the SR-series. Figure II.6.10 shows the high resolution DSC curve for the bis-(3- fluorobenzylimido)perylene, SR2. There is no thermal decomposition below 400°C. A similar trend was observed for the SR-4, SR-6, and SR-7 compounds. It can be concluded that the samples are thermally stable for devices that operate in the temperature range below 400°C. The DSC analysis for SR-4, SR-6, and SR-7 are shown in Figures II.6.11-13, respectively.

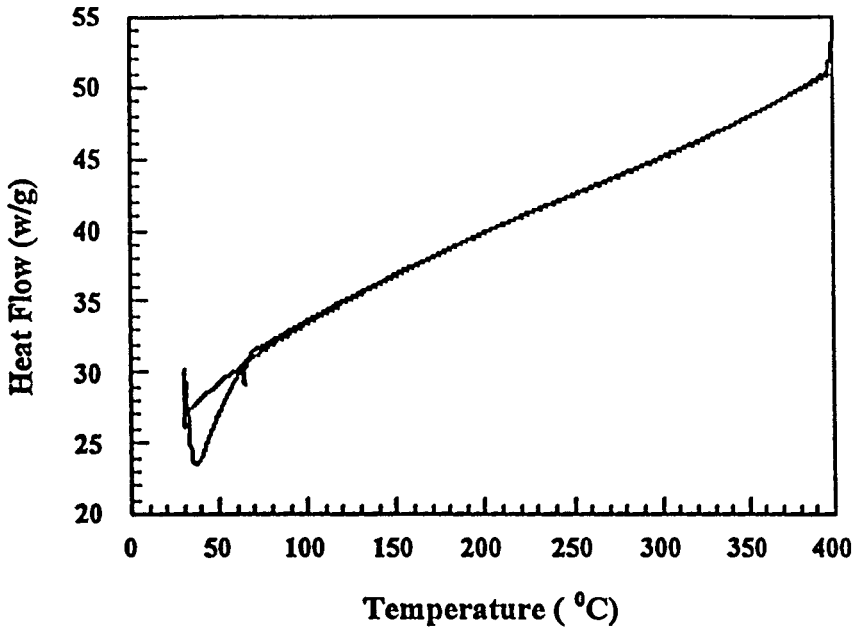

Figure II.6.10: DSC traces of bis-(3-fluorobenzylimido)perylene SR2.

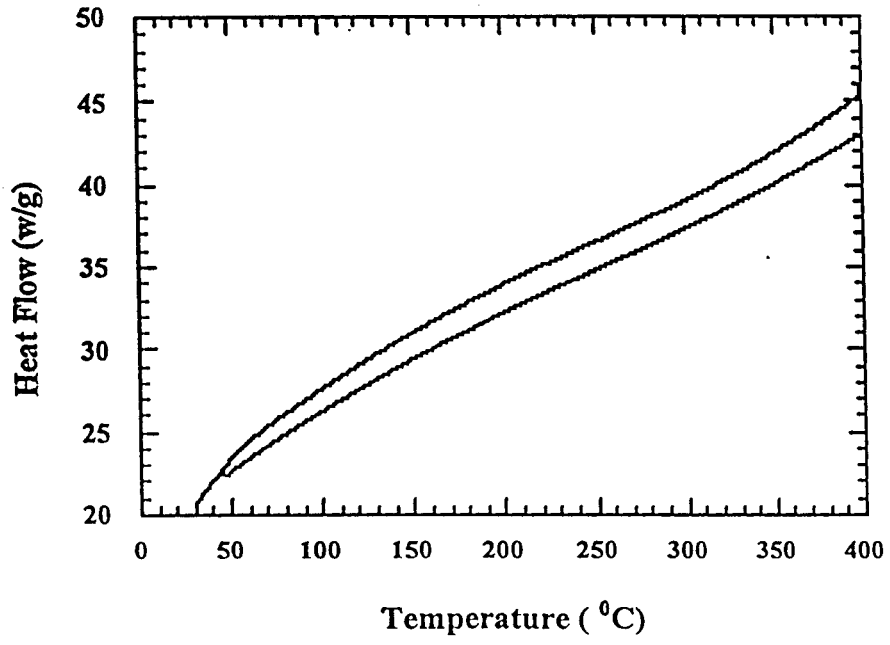

Figure II.6.11: DSC traces of bis-(2,6-difluorobenzylimido)perylene SR4.

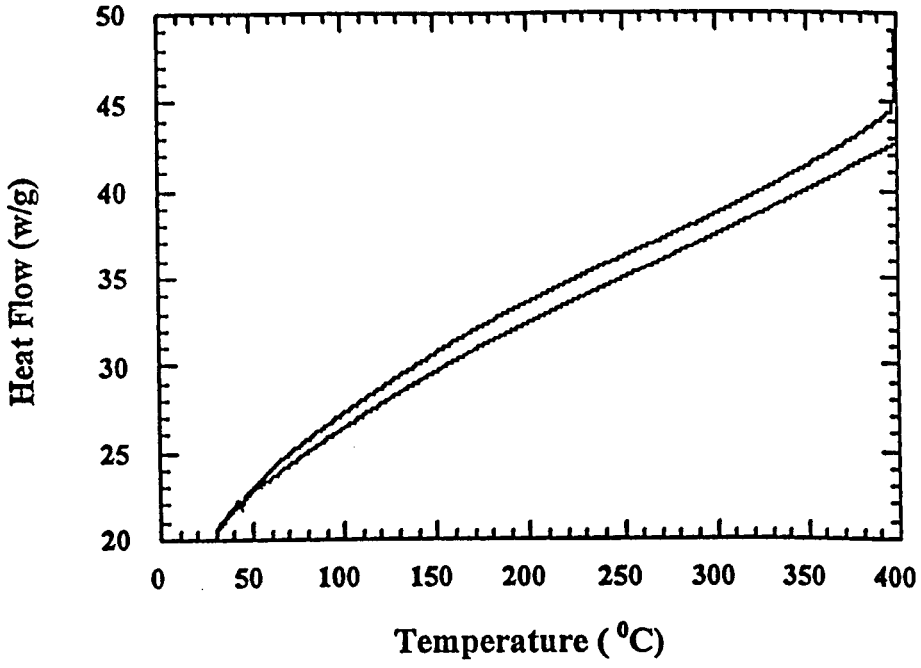

Figure II.6.12: DSC traces of bis-(3,4-dichlorobenzylimido)perylene SR6.

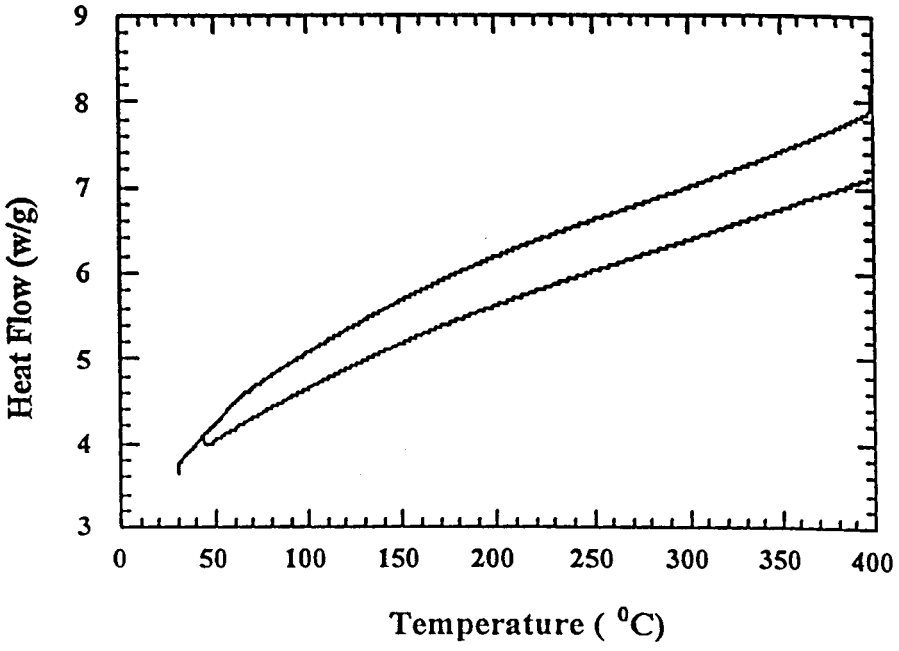

Figure II.6.13: DSC traces of bis-(3,5-dichlorobenzylimido)perylene SR7.

Chapter 7

X-RAY DIFFRACTION AND IR SPECTROSCOPY OF POLYAROMATIC COMPOUNDS

II.7.1. Structural analysis of polyaromatic compounds

II.7.1.1. Introduction

The epitaxial growth of polycyclic aromatics on inorganic and organic surfaces provides an interesting hybrid system that has shown quantum confinement effects when alternating layers are deposited [211,212].

Perylene-3,3,9,10-tetracarboxylic-3,4,9,10-dianhydride (PTCDA), has a flat conjugated structure that tends to organize in the face-on lying (102) plane. The crystal structure has two monoclinic polymorphs with different lattice parameter, but both crystallizes in the $P2_1/c$ space group. The lattice parameters of both polymorphs are given in Table II.7.1.

Table II.7.1: Lattice parameters of PTCDA polymer polymorphs [205]

Lattice parameters of PTCDA	**α- Phase**	**β-Phase**
a (Å)	3.74	3.78
b (Å)	11.96	19.30
c (Å)	17.34	10.77
β (degree)	98.8	83.6
Space Group	$P2_1/c$	$P2_1/c$
Unit cell volume $(Å)^3$	766.5	780.8
Area in unit mesh	238.12	240.3
d (102) (Å)	3.22	3.25

The chemical structure of PTCDA, is shown in Figure II.7.1. The length of a single molecule is gas phase is 14.1 Angstrom, and area of a unit mesh about 240 $(Å)^2$. X-ray diffraction and IR spectra of PTCDA and thio-PTCDA and a series of PTCDA derivatives have been studied. The molecular structure of PTCDA derivatives is listed in Table II.7.2.

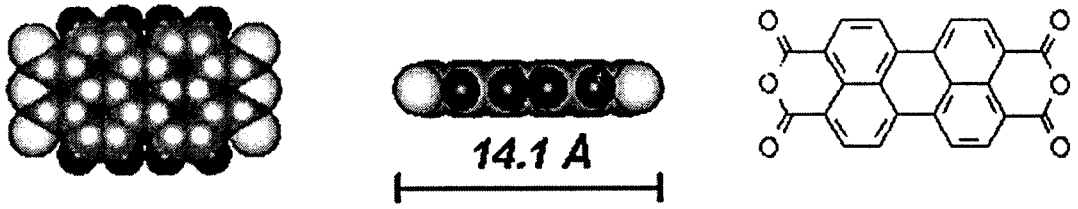

Figure II.7.1: Chemical structure and dimension of PTCDA [206].

II.7.2. X-ray diffraction of polyaromatics compounds

X-ray diffraction of PTCDA, thio-PTCDA, SR2, SR4, SR6 and SR7 were studied using a Siemens 5000 X-ray goniometer equipped with a Rigaku 18KW Rotating Cu anode. The diffraction data were collected at 0.02 degree scan between 10 to 90 2(θ). The X-ray diffraction data was collected from a pellet of material. The material was ground well with reference materials (graphite or silicon), and then palletized at $5ms/cm^2$. X-ray diffraction of pellets is collected for determination of lattice parameters.

A simulated x-ray diffraction pattern of α-phase PTCDA is shown in Figure II.7.2. The simulated PTCDA diffraction pattern, using the lattice parameters listed in Table II.7.2, has a strong (011) diffraction line at 9.01 Å, similar to that of the experimental diffraction pattern for PTCDA shown in Figure II.7.3.

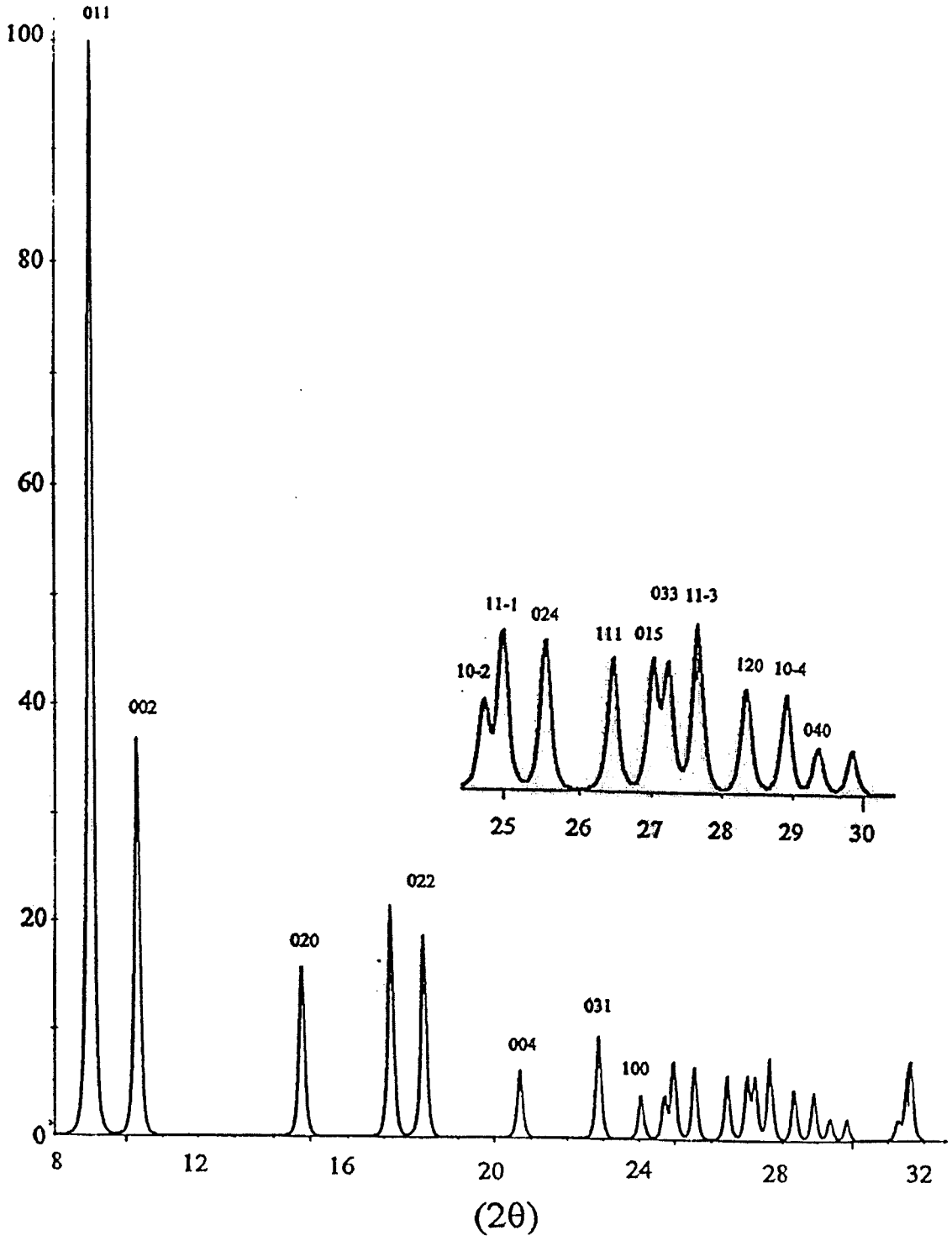

Fig. II.7.2. Simulated X-ray diffraction pattern of PTCDA for α-phase polymorph ($P2_1/c$).

The PTCDA molecules are arranged in monoclinic structure, where the molecules are lying flat along the plane of (102).

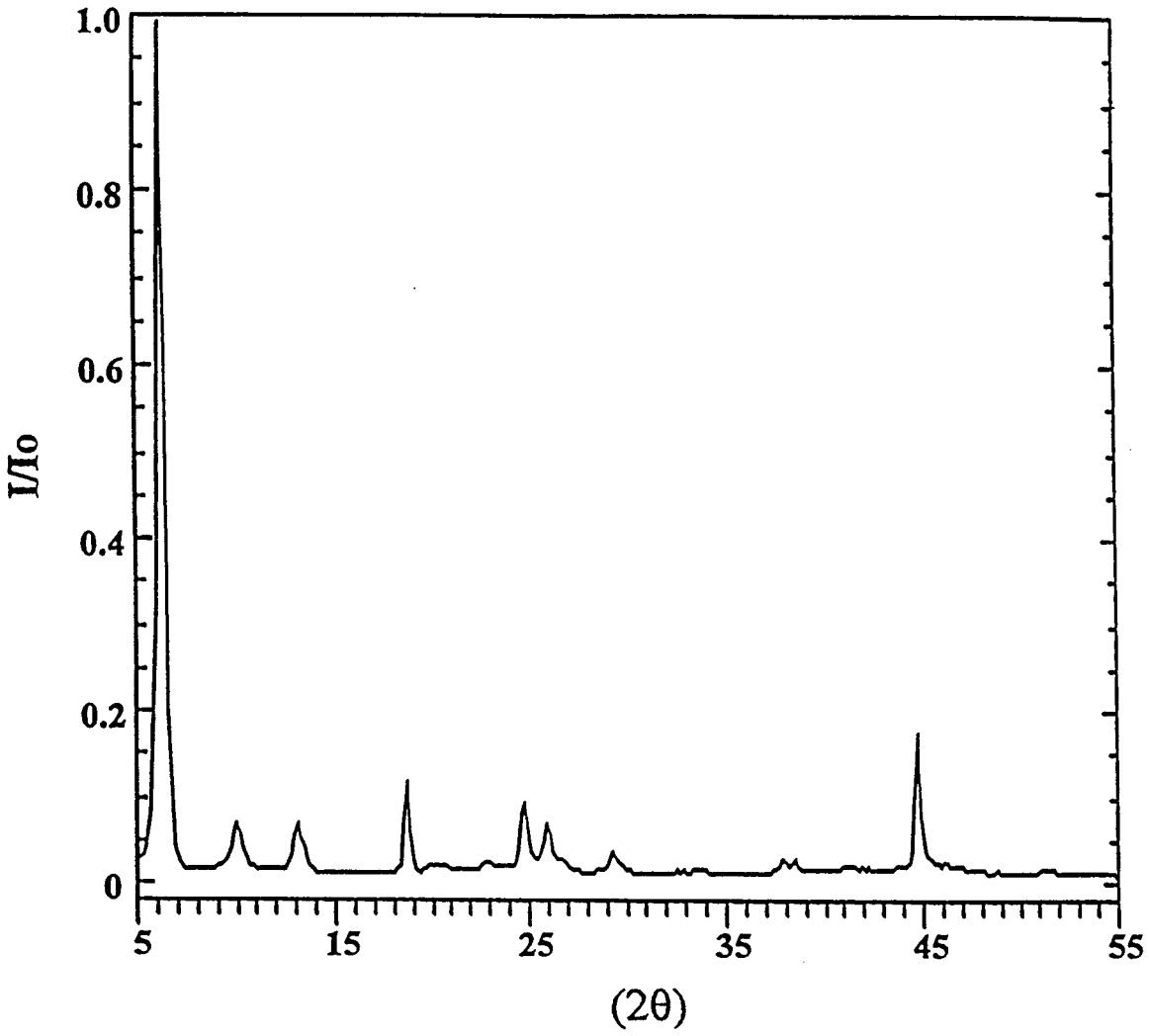

Figure II.7.3: X-ray diffraction of PTCDA with Cu (Kα) radiation.
The peak around 45° (2θ) is from substrate.

Table II.7. 2: (hkl) values for PTCDA with *P21/c* space group

(hkl)	2theta
(0 1 1)	9.01
(0 0 2)	10.32
(0 2 0)	14.80
(0 2 2)	18.07
(0 0 4)	20.72
(0 3 1)	22.88
(1 0 0)	24.06
(1 0 -2)	24.71
(1 1 -1)	24.97
(0 2 4)	25.56
(1 1 1)	26.48
(0 1 5)	27.04
(0 3 3)	27.26
(1 1 -3)	27.67
(1 0 2)	27.69
(1 2 0)	28.36
(1 2 -2)	28.93
(1 0 -4)	29.38
(0 4 0)	29.86

X-ray diffraction of PTCDA and the Thio-PTCDA are also shown in Figure II.7.4. The x-ray diffraction of thio-PTCDA, shown in Figure II.7.4, is different from the diffraction pattern of the PTCDA. This indicates a different crystal packing.

X-ray diffraction patterns of SR-series indicate different crystal packing than the packing of PTCDA and thio-PTCDA as shown in Figure II.7.4.The compounds have crystalline and amorphous phases as shown by very sharp X-ray lines, and a few broader X-ray diffraction lines. This type of mixture is usually produced from a precipitation mechanism or through solvent extraction techniques used during synthesis and purification of the materials.

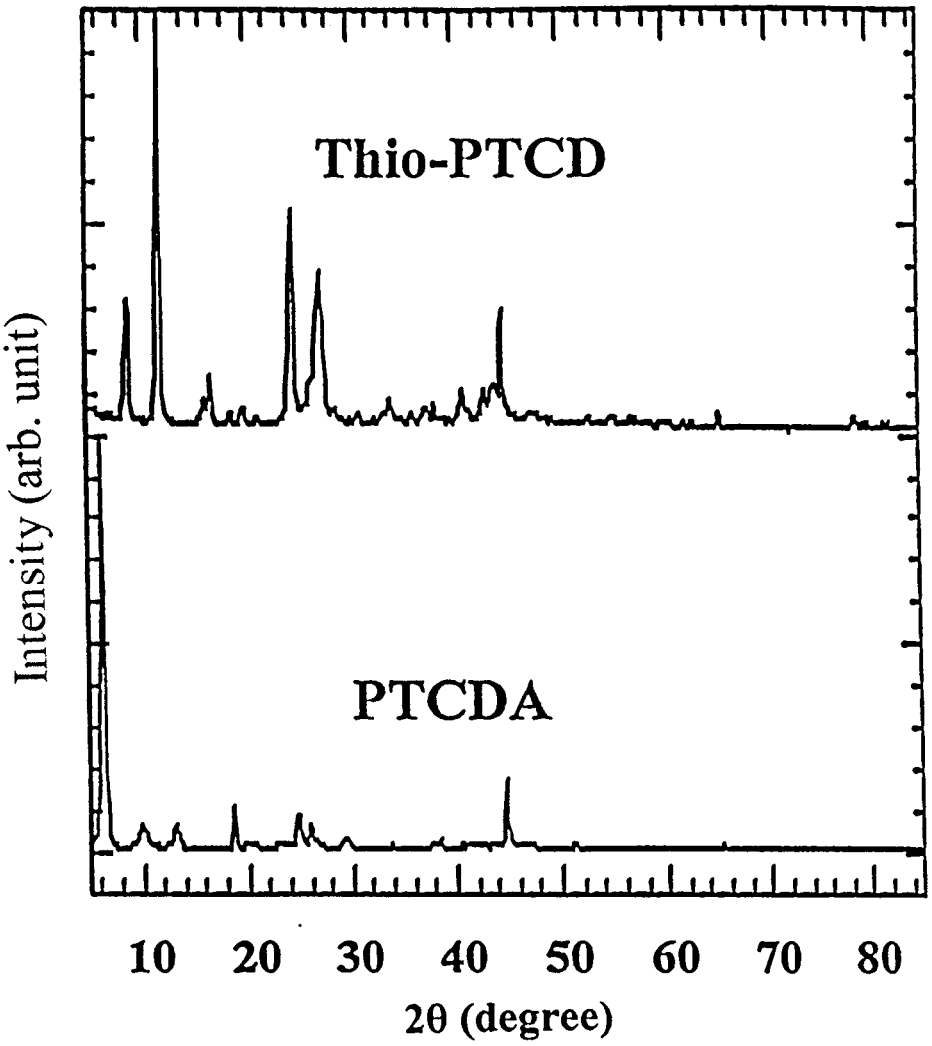

Figure II.7.4: X-ray diffraction of Thio-PTCDA and PTCDA.

However, the general trends in the X-ray diffraction patterns of SR-series indicate that they have similar crystal structures. The position of broader lines is also located at the similar 2-theta position indicating the degree of disorder is along the same planes for these series.

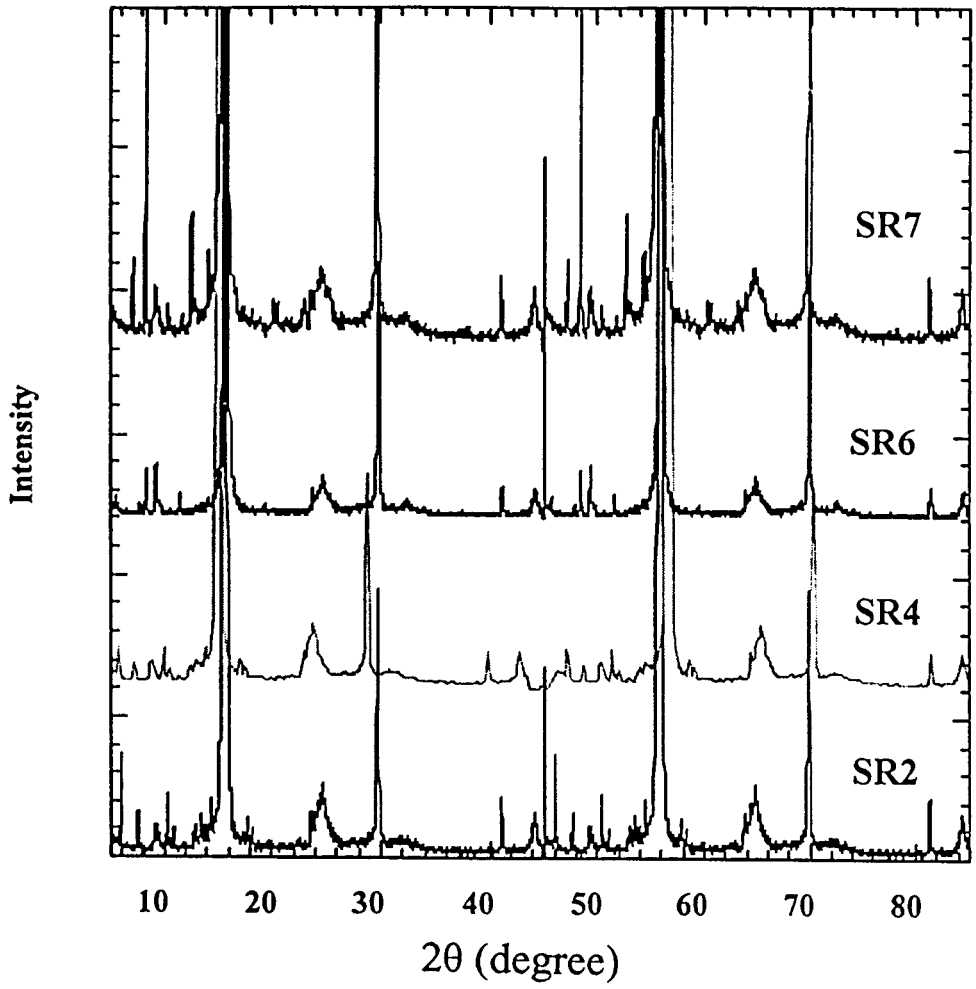

Figure II.7. 5: X-ray diffraction patterns of: SR2) Bis-(3-fluorobenzylimido)perylene, SR4) Bis-(2,6difluorobenzylimido)perylene, SR6) Bis-(3,4 dichlorobenzylimido)perylene, and SR8) Bis-(3,5 dichlorobenzylimido)perylene. .

The crystal structures are more aligned and organized in some of the crystallographic planes, and less ordered in other directions as evidenced by a series of sharp and broad diffraction lines. The existence of sharp and broad diffraction lines also

can be interpreted as arising from a mixture of amorphous phase along with the well-crystallized phases in this series of compounds.

II.7.3. IR spectroscopy of polyaromatics molecules

IR spectroscopy of PTCDA and thio-PTCDA in mid-IR range has been previously studied and reported [215-217]. However, not much attention has been given to the vibrational modes in the Far-IR region to study the low energy deformation modes and the lattice vibrations. In this work we studied the Far-IR spectra of both the PTCDA and the thio-PTCDA. The samples are ground to fine powder in methanol to make an ink-type slurry. A small drop of the slurry was spread on a (0.5 mm thick) polyethylene disc. The sample was dried under vacuum at 70ºC. The IR spectra were collected in transmission mode, under vacuum, using a DTGS Far-IR detector.

Table II.7.3: Molecular structures of SR2, SR4, SR6, and SR7.

Bis-(3-fluorobenzyl imido) perylene	$C_{38}H_{18}N_2O_4F_2$ (576.5662) SR2	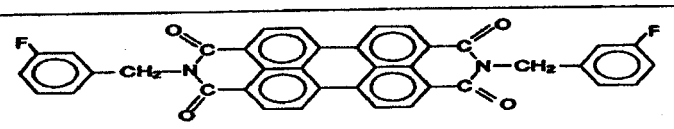
Bis-(2,6 difluorobenz ylimido) perylene	$C_{38}H_{14}N_2O_4F_4$ (616.5634) SR4	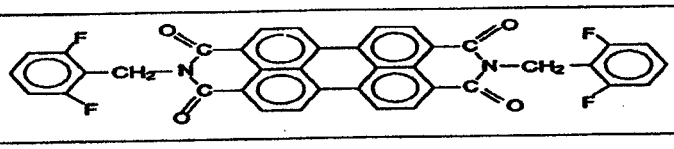
Bis-(3,4 dichlorobenz ylimido perylene	$C_{38}H_{14}N_2O_4Cl_4$ (682.3814) SR6	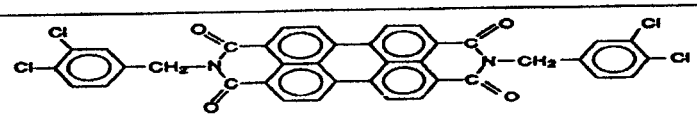
Bis-(3,5 dichlorobenz ylimido perylene	$C_{38}H_{14}N_2O_4Cl_4$ (682.3814) SR7	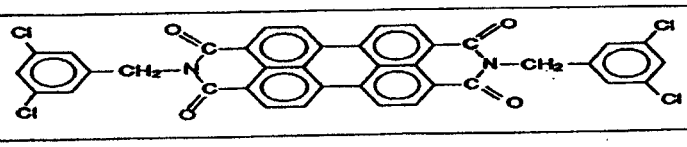

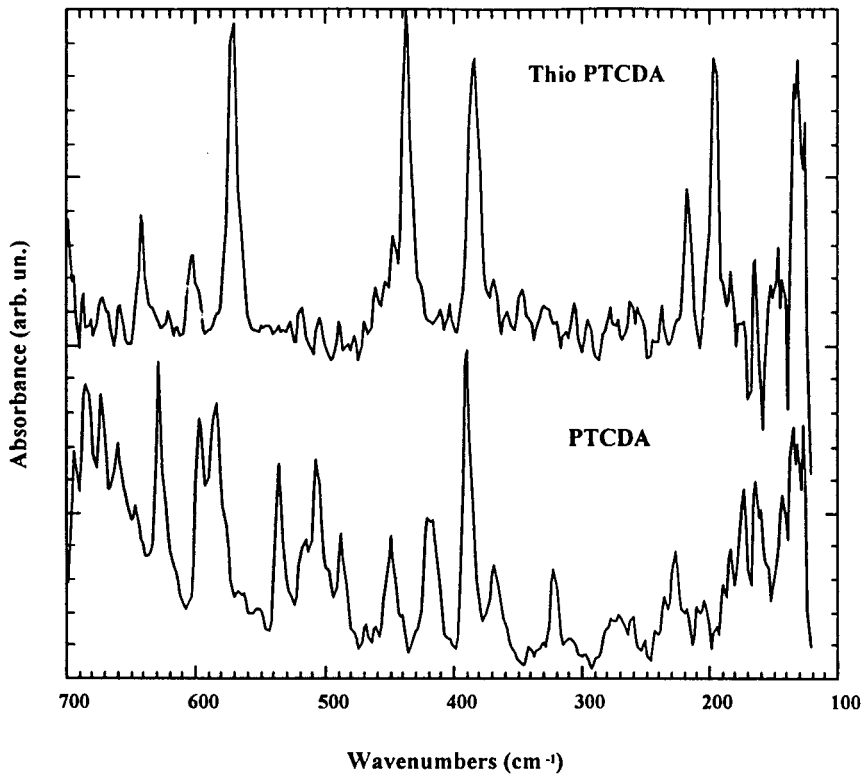

Figure II.7.6: Far-IR spectra of PTCDA and thio-PTCDA

Table II.7.4: Vibrational modes (cm^{-1}) for PTCDA and thio-PTCDA in Far-IR region

Vibrational-modes	PTCDA	Thio-PTCD
CC deformation	227.1 m	217.6 vs
CC deformation	320.2 m	304.4 w
CC torsion	389.6 vs	383.8 vs
CC Torsion	418.7 s	420 vw
CC torsion + CC bend	449.2 s	436 vs
CC torsion (biphenyl)	505.8 s	501 vw
CC torsion (biphenyl + naphthyl)	535.5 s	537 w
CC torsion	583.1 vs	571.1 vs
CC deformation + CC torsion	596.9 vs	602.3 s
CC torsion + CC deformation	627.8 vs	641.5 s
CC deformation	658.6 s	659.5 w
CC deformation	686.5 s	689.0 vs

The far-IR spectra of the PTCDA and thio-PTCDA are shown in Figure II.7.6. The vibrations below 700 cm^{-1} are related to ring deformation and other low energy lattice vibrations. The overlap of peak positions for PTCDA and the thio-PTCDA indicate that some characteristic modes of the PTCDA moiety or similar lattice vibration energies exist for both molecules. Clear differences in the far-IR spectra are caused by thio-substitutions which have changed the ring deformation and /or the lattice vibrations significantly. The far-IR wavenumbers for PTCDA and thio-PTCD are collected in Table II.7.4.

The recent HREEL spectrum of the PTCDA grown epitaxially on InAs has shown interesting energy-loss features [203]. The dominant loss features are at 724, 800, 855, 1015, and 1106 cm^{-1}, the C-N stretch at 1350, perylene ring stretching C=C, at 1590, and carbonyl stretching vibration at 1755 and 1855 cm^{-1}, as well as the C-H stretch at 3080 cm^{-1}. Pronounced changes occurred on C=O stretching vibration as a function of the coverage and thickness of the film.

The NEXAFS study of the PTCDA during deposition [218] on Si(111), Ni(111) and Ag(111) has identified bands in the C 1s spectrum due to π^* resonance at photon energies of 284.5, 286.0 and 288.5 eV. These values correspond to unoccupied states at 4.8, 3.4 and 1.0 eV below E_{vac}, but a typical core-hole stabilization energy of ~ 4 eV for the ground state molecule means that the first of these unoccupied states lies 0.8 eV below E_{vac}, whilst the other two are at 0.6 and 3.0 eV above E_{vac} The corresponding O 1s

NEXAFS data also showed a π^* resonance at ~ 3 eV above E_{vac} (assuming the same core hole stabilization [208]

II.7.4. IR spectroscopy of SR2, SR4, SR6, and SR7

The Mid-IR spectra of bis-(3-fluorobenzylimido)perylene (SR2), bis-(2,6-difluorobenzylimido)perylene (SR4), SR4) bis-(2,6-difluorobenzylimido)perylene, SR6) bis-(3,4-dichlorobenzylimido)perylene, SR7) bis-(3,5-dichlorobenzylimido)-perylene molecules were studied in the solid state. These molecules tend to form highly ordered structures and supramolecular assemblies. The vibrational modes in mid-IR is recorded and assigned to various fundamental modes of vibrations.

Experimentally, each sample, PTCDA, thio-PTCDA, SR2, SR4, SR6, SR7, were ground to fine powder and mixed with dry KBr to make a thin pellet. The sample pellet was sandwiched between two thin KBr pellets to prevent exposure to air. Mid- IR spectra were collected from 400–4000 cm^{-1}. Reference spectrum was collected from pure KBr pellet. The detector was a liquid nitrogen cooled MCT.

Vibrational frequencies for SR2, SR4, SR6, and SR7 molecules are listed in Table II.7.2. The C=O stretching vibrations are listed above 1650 cm^{-1}. The C-C torsional and deformational modes are below 800 cm^{-1}.

Table II.7.5: Wavenumbers and vibrational assignment for SR2, SR4, SR6, and SR7 in Mid-IR (the vibrational assignments are listed based on the wavenumbers for SR2)

Vibrational modes	SR2(cm^{-1})	SR4(cm^{-1})	SR6(cm^{-1})	SR7(cm^{-1})
Perylene deformation	630 w	633m	632w	630w
Perylene deformation	690 m	687w	688 w	698 m
C-H wagging	736 w	730 m	723 w	715 m
C-H wagging	743 w	751 m	756 s	751 s
Ring deformation	735 m	787 m		790
C-H wagging	742 s	811 ms	812 s	810 s
C-H wagging	756 vs	854 w	857 w	859 m
C-F streching	785 s	1026 s	1031 w	857
C-H bending	790 m	1174 m	1169 m	1169 m
C-H bending	812 w	1248 m	1244 m	1241 w
Ring st. + C-H bending	850 vw	1266 w		1254 m
Ring st. + C-H bending	856 w	1302 w		1302 w
C-N stretching	894 m	1338 s	1327 s	1327 s
Ring stretching	984 w	1379 m	1368 vs	1368 s
Ring stretching	997 w	1403 m	1403 m	1403 m
Ring stretching	1014 m	1435 m	1436 m	
Ring stretching	1126 vw	1454 vw		
Ring stretching	1241 m	1472 m	1469 m	1471 w
Ring stretching	1251 m	1508 w	1508 w	1508 w
Ring stretching	1311 vw	1518 vw		
Ring stretching	1330 w	1537 vw		
Ring stretching	1342 w	1557 w		
C=C stretching	1370 m	1579 m	1580 m	1572 s
C=C stretch	1590 vs	1593 vs	1592 vs	1592 vs
C=C stretch	1651 m	1627 m		1612 w
C=O anti-symmetric stretch	1655	1664	1657 vs	1660 vs
C=O symmetric stretch	1693 vs	1698 vs	1696 vs	1697 vs

The mid-IR spectra of SR2, SR4, SR6, and SR7 are shown in Figure II.7.7. The peak assignments are listed in Table II.7.5. The strong C=C in plane stretching mode around 1570-1600 cm^{-1} and C=O stretching modes around 1650 cm^{-1} for antisymmetric and around 1690 cm^{-1} for the symmetric can be used to study the orientation of molecules in this films. The C-N stretching vibration around 1350 cm^{-1} is also strong and can be used as a probe to further understand the stacking of the molecules, particularly in thin films.

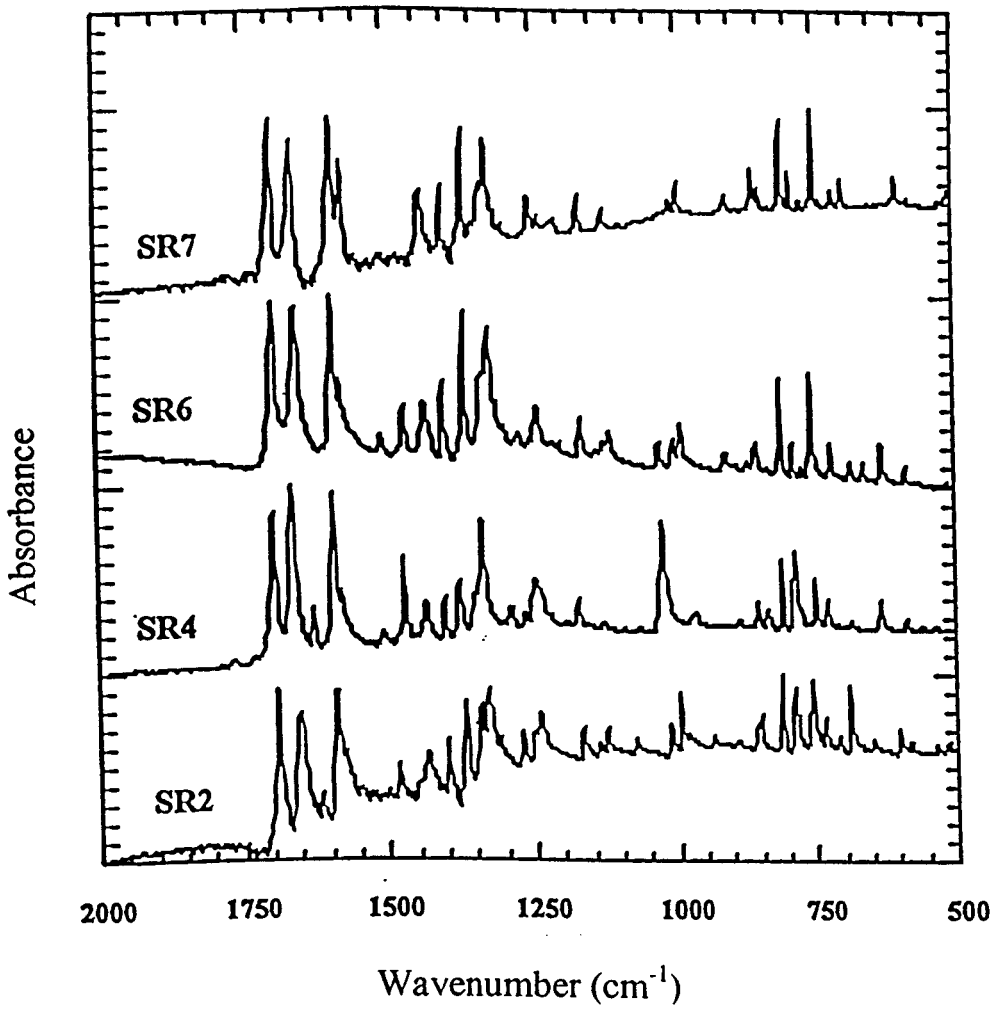

Figure II.7.7: FT-IR spectra of SR2, SR4, SR6, SR7.

Chapter 8

CONCLUSIONS

II.8.1. Conclusions

The work presented in this thesis claims major contributions in four technologically important areas;

1) Formulation of a novel multi-component electrolyte for advanced lithium batteries has been identified. This electrolyte, based on ternary solvent blend of organic carbonates, may solve the problem of low temperature performance of the batteries.
2) Safety issues of the lithium battery related to the electrolyte decomposition and formation of gaseous species have been studied. The chemical nature of the reaction by-products formed on the surface of electrode (SEI layer) and its influence on cell performance has been investigated. The thermal properties of the SEI layers in Li-ion batteries was studied, and based on data obtained in this work, it is claimed that the current lithium-ion battery is not safe when operate or exposed to temperatures above 150 ^{0}C.
3) A new diagnostic tool based on carbon-paste microelectrode techniques has been developed to study the electrochemical properties of non-conductive and insoluble organic solids. The formulation of carbon paste composites allows for the incorporation of organic and/or inorganic compounds in a conductive matrix of carbon for electrochemical studies. In addition, during the course of this study a simple accessory was designed for X-ray diffraction of air-sensitive materials. This accessory does not need the use of beryllium window and does not generate extra X-ray diffraction line.

4) The electrochemistry, vibrational spectroscopy, and X-ray diffraction of a series of novel polyaromatic compounds were studied. It is found that some of the perylene derivatives have fast switching characteristics between reduced and oxidized states. It is also found that most of the polyaromatics based on perylene derivatives are thermally stable up to 400°C, indicating their suitability for devices that may experience high temperature environment such as color copier and solid-state solar cells.

In the first part of this thesis work, dynamics of ion-solvent and solvent-solvent interactions, with focus on ion-association in multi-component nonaqueous organic electrolytes, have been reviewed. The mixture of cyclic and linear organic carbonates was identified as the most stable system electrochemically (up to 5 volt vs Li electrode), and with high ionic conductivity even at sub-ambient temperatures (down to –40°C). Blending linear carbonates and cyclic carbonates in presence of a low lattice energy lithium salt, $LiPF_6$, optimized the conductivity of the organic carbonate based electrolyte. The temperature-dependent conductivity of multi-component electrolytes was measured in a wide temperature range (-40 to 70 ^{0}C). It was discovered that the eutectic formed by mixing linear and cyclic carbonate solvents remains liquid in the required operating temperature range of the Li-cells. No phase separation of organic carbonate was observed when multi-blend of linear and cyclic carbonates are used.

It was shown that there is a strong selective solvation of lithium ion with cyclic carbonate solvents as compared to linear carbonate solvation. This is very important in

designing electrolyte for lithium batteries, as during the charging of the cell, the lithium ions may carry their solvation shells to the anode interface. Desolvation process before lithium intercalation concentrate the electrode interface with solvent that has more negative solvation Gibbs energy. Therefore, the film that may form due to electrolyte decomposition at the electrode-electrolyte interface may benefit from the protective film formed by the decomposition of preferred carbonates.

A novel ternary mixture of solvent was formulated based on combination of ethylene carbonate, propylene carbonate and dimethyl carbonate, that provides high conductivity in a wide temperature range and forms a stable film at the electrode-electrolyte interface with good lithium ion conductivity. It was also discovered that when ternary mixtures of organic carbonates are used in the make-up of the electrolyte, a lower salt concentration (0.6-0.8 Mol/liter) can be used as compared with the current technology that uses over 1M salt. The lower salt concentration may reduce the cost of the lithium battery technology.

Safe operation of advanced batteries is very important, particularly in large size system for stationary and transportation applications. During the course of this work, it was found that the major safety issue is related to the decomposition of electrolyte on the surface of the lithiated anode. In particular, the protective films that formed on the anode surface during initial lithiation may be destroyed if the temperature of the battery exceeds 150°C. Therefore, according to the results provided in this thesis work, operation of current lithium battery should be limited to temperatures below 150°C. Thermal analysis

has shown exothermic decomposition of electrolyte on the surface of lithiated anode above 150°C. In order to improve thermal property of lithium-ion battery a more stable surface film is required. Therefore, use of organic additives that may form SEI layer with enhanced thermal and ionic conductivity is recommended.

A simple yet very practical tool was designed for the X-ray diffraction analysis of air-sensitive materials. This design allows the air-sensitive samples to be mounted inside of a dry box filled with inert gas, and then transferred to the diffractometer for analysis. The advantage of this design is that doesn't need a beryllium window, and does not give any extra diffraction lines. The protective polymer window used to protect the sample is well above the focal plane of the X-ray beam and do not interfere with the X-ray diffraction lines. X-ray diffraction of several anode materials and polyaromatic compounds have been studied successfully using this accessory.

Further, a novel carbon-paste microelectrode is also designed for electrochemical study of non-conductive and insulating organic solids. This electrode conveniently allows one to obtain the redox potential of solid samples and the nature of charge transport in electrochemical system can be studied. In most polyaromatic compound studied in this work, using the microelectrode carbon paste, a diffusion-controlled process was observed, as indicated by the linear relationship of the redox peak potential versus the square root of potential sweep rates.

Electrochemical redox characteristics of a series of polyaromatic based on perylene derivatives were obtained. The fast redox-switching phenomenon was observed for some of the perylene derivatives. These compounds are suitable for electrochromic switching windows and solar cells, which require large cycle life. The carbon paste microelectrode is also a fast screening technique to evaluate electrochemical properties of a large number of organic and inorganic derivatives. X-ray diffraction of the perylene derivatives, particularly the PTCDA and thio-PTCDA indicate formation of a monoclinic crystal structure with preferred flat lying of the molecule in the (102) directions. The polyaromatics have the tendency for preferred orientation when made in thin-films due to the dispersion forces that exist in poly-conjugated compounds. High-resolution thermal analysis of perylene derivatives has shown thermal stability up to 400°C. These compounds are well suited for applications such as color copiers and solar cells that may reach high temperatures during their operation.

REFERENCES

[1] Buckingham, A. D.; Lippost, E.; Bratos, S., Organic Liquids, Structures, Dynamics, and Chemical Properties, Wiley-Interscience, London, 1978.

[2] Klassen, B.; Aroca, R.; Nazri, M.; Nazri, G. A., J. Phys. Chem. 1998, 102, 4795.

[3] Cattaneo, E.; Rasch, B.; Vielstich, W., J. Appl. Electrochem. 1991, 21, 885.

[4] Koch, V. R.; Dominey, L. A.; Nanjundiah, C.; Ondrechen, M. J., J. Electrochem. Soc. 1996, 143.

[5] Cook, M. J.; Mckeown, N. B.; Salmons, J. M.; Thomson, J.; Daniel, M. F.; Harrison, K. J.; Richardson, R. M.; Stephen, J., J. Mater. Chem. 1991, 1, 121.

[6] Griffiths, J.; Schofield, J.; Wainwright, M.; Brown, S. B.; Dyes and Pigments 1997, 33, 65.

[7] George, R. D.; Snow, A. W.; Shirk, J. S.; Barger, W. R., J. of Porphyrins and Phthalocyanines 1998, 2, 1.

[8] Graser, F.; Hadicke, E., Liebigs Ann. Chem. 1980, 1994.

[9] Day, P. N.; Wang, Z. R.; Pachter, R. J., J. of Molecular Structure 1998, 455, 33.

[10] Ogawa, T.; Kuwamoto, K.; Isoda, S.; Kobayashi, T.; Karl, N., Acta Cryst. 1999, B55, 123.

[11] Orti, E.; Bredas, J. L.; Clarisse, C., Route de Tregastel-BP 40, F-22301 Lannion, France 1989.

[12] Heutz, S.; Ferguson, A.J.; Rumbles, G.; Jones, T.S., Organic Electronics 2002, 3, 119.

[13] Fuchigami, H.; Tanimura, S.; Uehara, Y.; Kurata, T.; Tsunoda, S., Jpn. J. Appl. Phys. 1995, 7B, 3852.

[14] Wong, M. K.; Mckinney, W. J.; Pooy, A. I.; J. Phys. Chem. 1971, 56, 75.

[15] Schantz, S.; Torell, L. M.; Stevens, J. R., J. Appl. Phys. 1988, 64, 2038.

[16] Gejji, S. P.; Hermansson, K.; Tegenfeldt, J.; Lindgren, J., J. Phys. Chem. 1993, 97, 11402.

[17] Fukushima, K.; Nishiyama, T.; Unno, Y., J. of Molecular Structure 1992, 271, 279.

[18] Ladanyi, B. M.; Stratt, R. M., J. Phys. Chem. 1995, 99, 2502.

[19] Frech, R.; Manning, J. P., Electrochim. Acta 1992, 37, 1499.

[20] Nakamoto, K., Infrared and Raman Spectra of Inorganic and Coordination Compounds, Third Edition, John Wiley & Sons, New York 1978.

[21] IR/113 Service Manual, Bruker FTIR Spectrometr, Bruker Optics, 1983.

[22] The Complete Guide to FT-IR Accessories and Supplies, Spectratech, revision 1998, Spectratech Inc. Shelton, CT. USA.

[23] Harrick, N. J., Internal Reflection Spectroscopy, Inter-scince Publishers, NY, 1967, and Harric Scientific Corporation, Catalog HSC-831, 1998.

[24] Ohta K.; Iwamoto, R., Appl. Spectroscopy 1985, 39, 418.

[25] Inshino, Y., Ishida, H., Appl. Spectroscopy 1988, 42, 1296.

[26] Service Manual, Vacuum Atmosphere Inc. 1997.

[27] Magat, M., J. Phys. Chem. 1932, A162, 432.

[28] Sheppard, S. E., Chem. Abstr. 1943, 37, 1654.

[29] Scheibe, G.; Felger, E.; RoBler, G., Ber. Dtsch. Chem. Ges. 1927, 60, 1406.

[30] Hildebrand, J.H.; Prausnitz, J. M.; Scott, R. L., Regular and Related Solutions, VanNorstranf-Reinhold, Princeton, 1970.

[31] Bottcher, C. J. F., Theory of Electric Polarization, Vol. I, Second Edition, Elsevier Scientific Publishing Co., New York 1973.

[32] Weast, R. C.; Astle, M. J., CRC Handbook of Data on Organic Compounds, Vol I and II, CRC Press, Florida, 1985.

[33] Weast, R. C.; (ed.), Handbook of Chemistry and Physics, 66th Edition, CRC Press, Florida 1986.

[34] McClellan, A. L., Table of Experimental Dipole Moments, Freeman Co., San Francisco, 1963.

[35] March, N. H.; Tosi, M. P., Coulomb Liquids, Academic Press, New York 1984.

[36] Amev, R. L., J. Phys. Chem. 1968, 72, 3358.

[37] Rabinowiz, M.; Pines, A., J. Am. Chem. Soc. 1969, 91, 1585.

[38] Keesom, W. H., Z. Physik 22 1922, 23, 225.

[39] Debye, P., Z. Physik 21 1921, 22, 302.

[40] Mahanty, J.H.; Ninham, B.W., Dispersion Forces, Academic Press, New York

1977.

[41] Yoder, C. H., J. Chem. Educ.1977, 54, 402.

[42] Hill, N.E.; Vaughan, W.E.; Price, A.H.; Davice, M., Dielectric Properties and Molecular Behaviour, Van Norstrand Reinhold Co., London 1969.

[43] Thomas, K.E.; Darling, R.M.; Newman, J., Mathematical Modeling of Lithium Batteries, in Advaces in Lithium-ion Batteries, (eds. Schalkwijk, W.A., Scrosati, B.), Kluwer Academic / Plenum Publishers, Boston 2002.

[44] Paetzold, R., Z. Chem. 1975, 15, 377.

[45] Drago, R. S.; Parr, L.B., Chamberlain, C.S., J. Am. Chem. Soc. 1977, 99, 3203.

[46] Gutmann, V., Coordination Chemistry in Non-Aqeous Solvents, Springer, Wien, NY 1968.

[47] Gutmann, V., Coord. Chem. Rev. 1967, 2, 239.

[48] Mayer, U., Pure Appl. Chem. 1975, 41, 291.

[49] Gutmann, V., Pure Appl. Chem. 1973, 15, 141.

[50] Mayer, U., Pure Appl. Chem. 1979, 51, 1697.

[51] Schmid, R., Sapunov, V. A., Verlag Chemie 1982.

[52] Bender, C.J., Chem. Soc. Rev. 1986, 201.

[53] Mayer, U.; Gutmann, V.; Gerger, W., Pure Appl. Chem. 1979, 51, 1697.

[54] Schmid, R., J. Sol. Chem. 1983, 12, 135.

[55] Mayer, U., Pure Appl. Chem.1979, 51, 1697.

[56] Criss, C. M.; Salomon, M., Thermodynamic Measurements - Interpretation of Thermodynamic Data, in Covington, A. K.; Dikinson, T., (eds): Physical Chemistry of Organic Solvent Systems, Plenum Press, London, NY 1973, 253.

[57] Gordon, J. E., The Organic Chemistry of Electrolyte Solutions., Wiley, New York 1975.

[58] Jackson, J. A.; Lemons, J. F.; Taube, H.; Alei, M.; Jackson, J. A., J. Chem. Phys. 1964, 41, 3402.

[59] Amis, E. S.; Hinton, J. F., Solvent Effects on Chemical Phenomena, Vol.1, Academic Press, New York 1973.

[60] Amis, E. S., Solvation of Ions, in Solutions and Solubilities, Vol. III, Part 1, of the series Techniques of Chemistry, Dack, M. R. J. (ed.), Wiley-Interscience, New

York 1975.

[61] Hinton, J. F.; Amis, E. S., Chem. Rev. 1971, 71, 627.

[62] Strehlow, H.; Schneider, H.; Knoche, W., Ber Bunsenges. Phys. Chem. 1973, 77, 760. and Pure Appl. Chem. 1971, 25, 327.

[63] Strehlow, H.; Koepp, H.; Schneider, H., Z. Phys. Chem. 1966, 44, 49.

[64] Blomgren, G. E., J. Power Sources 1985, 14, 39.

[65] Zaghib, K., The prospects for Lithium-Ion Batteries in Japan: workshop for Li-ion Batteries and Supercapacitors, Reno, NV, USA 1995.

[66] Rahner, D.; Machell, S.; Ludwing, G., J. Power Sources 1995, 54, 378.

[67] Battisti, D.; Klassen, B.; Nazri, G. A.; Aroca, R.; J. Phys. Chem. 1993, 97, 5826.

[68] Abraham, K.; M. Alamgir, M. J., J. Electrochem. Soc. 1990, 137, 1657.

[69] Klessen, B.; Aroca, R.; Nazri, G. A.; J. Phys. Chem. 1996, 100, 9334.

[70] Bloomgren, G. E., in Lithium Batteries, (ed): Gabano, J., Academic Press, New York 1983, p13.

[71] Gores, H. J.; Barthal, J., J. Solution Chem. 1980, 9, 939.

[72] Matsuda, Y., J. Power Sources 1987, 19, 20.

[73] Dudley, J. T.; Wilkinson, D. P.; Thomas, G.; LeVae, R.; Woo, S.; Blom, H.; Horvath, C.; Juzkow, M. W.; Denis, B.; Juric, P.; Aghakinan, P.; Dahn, J. R., J. Power Sources 1991, 35, 59.

[74] Watanabae, H.; Nohma, T.; Nakane, I.; Yoshimura, S.; Nishio, K.; Saito, T., J. Power Sources 1993, 217, 43.

[75] Prabhu, P. V. S. S.; Kumar, T. P.; Namboodiri, P. N. N.; Gangadharan, R. J., Appl. Electrochem. 1993, 23, 151.

[76] Aurbach, D.; Daroux; M.; Faguy, P.; Yeager, E. B., J. Electroanal. Chem. 1991, 225, 297.

[77] Lee, S. K.; Zu, Y.; Hermann, A.; Geerts, Y.; Mullen, K.; Bard, A. J., J. Am Chem.Soc. 1999, 121, 3513.

[78] Oesten, R.; Heider, U.; Schmidt, M., Solid State Ionics 2002, 148, 391.

[79] Yamaki, J-I., Liquid Electrolytes, in Adavances in Lithium-ion Batteries, (eds. van Schalwijk, Scrosati, B.), Kluwer Academic / Plenum Publishers, Boston 2002.

[80] Skoog, D.A.; Leary, J. J., Principles of Instrumental Analysis, Fourth Edition, Saunders College Publishing, New York 1992.

[81] Griffiths, P. R.; de Haseth, J. A., Fourier Transform Infrared Spectroscopy, Wiley, New York 1986.

[82] McClure G. L., Computerized Quantitative Infrared Analysis, ASTM Special Technical Publication, American Society for Testing and Materials, Philadelphia PA, 1987.

[83] Beer, R., Chem. Anal. 1992, 120.

[84] Koenig, J. L., Spectroscopy of Polymers, ACS, Washington. DC 1992.

[85] Aurbach, D.; Daroux, M. L.; Faguy, P. W.; Yeager, E. J. Electrochem. Soc. 1987, 134, 1611.

[86] Nazri, G. A.; MacArthur, D. M.; O,Gara, J. F.; Aroca, R., in Nazri, G.A., Shriver, D. F., Huggins, R.A., Balkanski, M., (eds), Materials Research Society Proceedings, Pittsburgh 1990, 210, 163.

[87] Croce, F., Panero, S., Scrosati, B., in Nazri, G. A., Shriver, D. F., Huggins, R. A., Balkanski, M., (eds), Materials Research Society Proceedings 1990, 210, 179.

[88] Maztragostino, M., in Nazri, G. A., Shriver, D. F., Huggins, R. A., Balkkanski, M., (eds): Materials Research Society Proceedings 1990, 210, 191.

[89] Nazri, G. A.; Shriver, D. F.; Huggins, R. A.; Balkanski, M., (eds), Materials Research Society Proceedings 1990, 210, 179.

[90] Chen, K.; Doan, K.; Ganapathiappan, S.; Ratner, M.; Shriver, D. F., in Nazri, G. A., Shriver, D. F., Huggins, R. A., Balkanski, M., (eds), Materials Research Society Proceedings 1990, 210, 211.

[91] Kalikihana, M.; Sandahi, J.; Schantz, S.; Torell, L. M., in Second International Symposium on Polymer Electrolytes, Scrosati, B., (ed.), London, NY 1990, 1.

[92] Irish, D. E.; Ozeki, T., in Chemical Analysis Series, Grasselli, J. G., Bulkin, B., (eds), John Wiley & Sons. New York 1991, 114, 59.

[93] McLin, M. G.; Angell, C. A., J. Phys. Chem. 1991, 95, 9464.

[94] Janz, G. J.; Ambrose, J.; Coutts, J. W.; Downey, J. R., Spectrochim.Acta 1979, 35A, 175.

[95] Arai, J.; Nishimura, K.; Muranaka, Y.; Ito, Y., J. Power Sources 1997, 68,

304.

[96] Torell, L. M.; Schantz, S.; Jacobson, P., in Materials Research Society Proceddings, in Nazri, G. A.; Shriver, D. F.; Huggins, R. A.; Balkanski, M., (eds), 1990, 210, 221.

[97] Aurbanch, D.; Gamolsky, K.; Markovsky, B.; Salitra, G.; Gofer, Y.; J. Electrochem. Soc. 2000, 147, 1322.

[98] Fong, R.; Sacken, U. V.; Dahn, J. R., J. Electrochem. Soc. 1990, 137, 2009.

[99] Wilkinson, D. P.; Dahn, J. R., 1992, U.S. Patent 5,130,211.

[100] Xu, K.; Ding, S. P.; Jow, T. R., J. Electrochem. Soc. 1999, 146, 4172.

[101] Hayashi, K.; Nemoto, Y.; Tobishima, S. Y., Denki Kagaku, 1999, 66, 1307.

[102] Demsler, J. P.; Planet, W. S., J. Chem, Phys. 1956, 24, 920.

[103] Matsuda, Y.; Sekiya, M., J. Power Sources 1999, 795, 81.

[104] Matsuda, Y.; Takemitsu, T.; Tanigawa, T.; Fukushima, T., J. Power Sources 2001, 589, 97.

[105] Wrodnigg, G. H.; Winter, M.; Besenhard, J. O., J. Electrochem. Soc. 1999, 146, 470.

[106] Wrodnigg, G. H.; Wrodnigg, T. M.; Besenhard, J. O., Winter, M., Electrochem. Commun. 1999, 148.

[107] Wrodnigg, G. H.; Reisinger, C.; Besenhard, J. O.; Winter, M., ITE Battery Lett. 1999, 110.

[108] Wrodnigg, G. H.; Besenhard, L. O.; Winter, M., J. Power Sources 2001, 592, 97.

[109] Abraham, K. M.; Willstaedt, D. M.; Pasquariello, E. B., J. Electrochem. Soc. 1990, 137, 1856.

[110] Narayama, S. R.; Surampudi, S.; Attia, A. I.; Bankston, C. P., J. Electrochem. Soc 1991, 138, 2224.

[111] Peled, E., J. Electrochem. Soc. 1979, 126, 2047.

[112] Peled, E., in Lithium Battery, (ed.) Gabano, J. P., Academic Press, New York 1983, 43.

[113] Scrosati, B., J. Electrochem. Soc. 1992, 139, 2776.

[114] Aurbach, D.; Ein-Eli, Y., J. Electrochem. Soc. 1995, 142, 1746.

[115] Tatsumi, K.; Iwashita, N.; Sakaebe, H.; Shioyama, H.; Higuchi, N., J.

Electrochem. Soc. 1995, 142, 716.

[116] Ohzuku, T.; Iwakoshi, Y.; Sawai, K., J. Electrochem. Soc. 1993, 140, 2490.

[117] Yazami, R.; Touzain, P., J. Power Sources 1983, 9, 365.

[118] Takami, N.; Satoh, A.; Hara, M.; Ohsaki, T., J. Electrochem. Soc.1995, 142, 371.

[119] Jiang, Z.; Alamgir, M.; Abraham, K. M., J. Electrochem. Soc. 1995, 142, 333.

[120] Morita, M.; Hayashida, H.; Matsuda, Y., J. Electrochem. Soc. 1987, 134, 2107.

[121] Shu, Z. X.; McMillan, R. S.; Murray, J., J. Electrochem, Soc.1993, 140, 922.

[122] Goren, E.; Chusid, O.; Aurbanch, D., J. Electrochem. Soc. 1991, 138.

[123] Farcy, J.; Messina, R.; Perichon, J., J. Electrochem. Soc. 1990, 137, 1337.

[124] Kumagai, N.; Matsuura, Y.; Tanno, K., J. Electrochem. Soc. 1992, 139, 3553.

[125] Kummagai, N.; Fukiwara, T.; Tanno, K.; J. Electrochem. Soc. 1993, 140, 3194.

[126] Kanehori, K.; Kirino, F.; Kudo, T.; Miyauchi, K., J. Electrochem. Soc. 1991, 138.

[127] Guyomard, D.; Tarascon, J. M., J. Electrochem. Soc. 1992, 139, 937.

[128] Baranski, A. S.; Fawcett, W. R., J. Electrochem. Soc. 1982, 129, 901.

[129] Yang, J.; Winter, M.; Besenhard, J. O., Solid Sate Ionics. 1996, 90, 281.

[130] Besenhard, J. O.; Muller-Warmuth, W.; Scholhorn, R., Kluwer Academic Publishers, Dordrecht 1994, p.457.

[131] Huggins, R. A., Solid Sate Ionics. 1998, 57, 113.

[132] Goward, G. R.; Taylor, N. J.; Souza, D. C. S.; Nazar, L. F., J. Alloy Compd. 2001, 82, 329.

[133] Thackeray, M. M.; Vaughey, J. T.; Kahaian, A. J.; Kepler, K. D.; Benedek, R., Electrochem. Commu. 1999, 1, 111.

[134] Akimoto, J.; Gotoh, Y.; Oosawa, Y.; Akimoto, J.; Gotoh, Y.; Osawa, Y., J. Solid State Chemistry. 1997, 7, 129.

[135] Kartha, J. P.; Tunstall, D. P.; Irvine, J. T. S., J. Solid State Chemistry. 2000, 152, 397.

[136] Arroyo de Dompablo, M. E.; Varez, A.; Garcia-Alvarado, F., J. Solid State Chemistry 2000, 153, 132.

[137] van de Krol, R.; Thesis, 2000, Universal Press, Veeneddaal, Netherland.

[138] Sodergren, S.; Siegbahn, H.; Rensmo, H.; Lindstrom, H.; Hagfeldt, A.; Lindquist, S. E., J. Phys. Chem. 1997, B 101, 3087.

[139] Murphy, D. W.; Cava, R. J.; Zahurak, S. M.; Santoro, A., Solid Sate Ionics. 1983, 413, 9.

[140] Chiang, Y.-M.; Birnie III, D.; Kingery, D. W., Physical Ceramics, MIT Series in Materials Science & Engineering, Wiley, New York 1997.

[141] Boschloo, G. K.; Goossens, A.; Schoonman, J., J. Electrochem. Soc. 1997, 144, 1311.

[142] Feist, T. P.; Davies, P. K., J. Solid State Chem. 1992, 101, 275.

[143] Nuspl, G.; Yoshizawa, K.; Yamabe, T., J. Mater. Chem. 1997, 7, 2529.

[144] Ohzuku, T.; Ueda, A.; Yamamoto, N., J. Electrochem. Soc. 1995, 142, 1431.

[145] Nishijima, M.; Takeda, Y.; Imanishi, N.; Yamamoto, O., J. Electrochem. Soc. 1994, 141, 2966.

[146] Shodai, T.; Okada, S.; Tobishima, S.; Yamaki, J., Solid State Ionics. 1996, 785, 86.

[147] Suzuki, S.; Shodai, T., Solid State Ionics. 1999, 1, 116.

[148] Rowsell, J. L. C.; Pralong, V.; Nazar, L. F., J. Am. Chem. Soc. 2001, 123, 8598.

[149] Pereira, N.; Klein, L. C.; Amatucci, G. G., J. Electrochem. Soc. 2002, A262, 149.

[150] Souza, D.; Pralong, V.; Jacobson, A. J.; Nazar, L. F., Science. 2002, 296, 2012.

[151] Pralong, V.; Souza, D. C.; Nazar, L. F., Electrochem. Com. 2002, 4, 516.

[152] Nagaura, T.; Tozawa, K., Prog. Battery and Solar Cells. 1990, 9, 209.

[153] Holmes, C. F.; Landgrebe, A. R., The Electrochemical Society Proceedings. 1997, 97, 18.

[154] Ohzuku, T.; Ueda, A., J. Electrochem. Soc. 1997, 144, 2780.

[155] Novack, P.; Miiller, K.; Santhanam, K. S. V.; Heas, O., Chem. Rev. 1997, 97, 207.

[156] Bicke, P.; Chu, W. F.; Weppner, W., Solid State Ionics. 1997, 93.

[157] Arakawa, M.; Yamaki, J., J. Power Sources 1995, 54, 250.

[158] Safran, S. A., Solid State Physics. 1987, 40, 183.

[159] Ulloa, S. E.; Kirczenow, G., Comments Cond. Mat. Phys. 1986, 12, 181.

[160] Dahn, J. R.; Sleigh, A. K., Shi; H., Reimer, J. N.; Zhong, Q.; Way, B. M., Electrochim. Acta 1993, 38, 1179.

[161] Cotton, F. A.; Wilkinson, G.; Murillo, C. A.; Bochmann, M., Advanced Inorganic

Chemistry, John Wiley & Sons. Inc. NY 1999.

[162] Richard, M. N.; Dahn, J. R., J. Electrochem. Soc. 1999, 146, 2068.

[163] Horowitz, G.; Kouki, F.; Spearman, P.; Fichou, D.; Nogues, C.; Pan, X.; Garnier, F., Avd. Mater. 1996, 8, 242.

[164] Adachi, M., Murata, Y., Nakamura, S., J. Phys. Chem. 1995, 99, 14240.

[165] Mercadante, R.; Trsic, M.; Duff, J.; Aroca, R., J. Mol. Structure. 1997, 215, 394.

[166] Ludwig, C.; Gompf, B.; Glatz, W.; Petersen, J.; Eisenmenger, W.; Mobus, M.; Zimmermann, U.; Karl, N., Z. Phys. 1992, 86, 397.

[167] Ludwig, C.; Gompf, B.; Glatz, W.; Petersen, J.; Eisenmenger, W., Z. Phys.1994, 93, 365.

[168] Schmitz-Hubsch, T.; Fritz, T.; Sellam, F.; Staub, R., Phys. Rev. 1997, 55, 7972.

[169] Fisher, C. M.; Burghard, M.; Roth, S.; Klitzing, K. V., Europhys. Lett. 1994, 28, 129.

[170] Schlettwein, D.; Back, A.; Scilling, B.; Fritz, T.; Armstrong, N. R., Chem. Mater. 1998, 10, 601.

[171] Bohringer, M.; Schneider, W. D.; Berndt, R.; Glockler, K.; Sokolowski, M.; Umbach, E., Phys. Rev. 1998, 57, 4081.

[172] Lamoen, D.; Ballone, P.; Piranello, M., Phys. Rev. 1966, 54, 5097.

[173] Silinsh, E. A., Organic Molecular Crystals, Berlin, Springer 1980.

[174] Tieke, B.; Wegner, G.; Naegele, D.; Ringsdorf, H., Chem. Int. 1976, 15, 764.

[175] Lieser, G.; Wegner, G.; Muller, W.; Enkelmann, V.; Meyer, W. H., Makromol. Chem. Rap. Comm. 1, 1980, 1, 627.

[176] Kajzar, F. M.; J. Chem. Phys. 1981, 63, 123.

[177] Day, D.; Hub, H. H.; Ringsdorf, H., J. Phys. Chem. 1979, 18, 325.

[178] Bader, H.; Ringsdorf, H.; Skura, J., Chem. Int.1981, 20, 91.

[179] Akimoto, A.; Dorn, K.; Gros, L.; Ringsdorf, H.; Schupp, H., Angew Chem. Int. 1981, 20, 90.

[180] Lopez, E.; O'Brien, D. F.; Whitesides, T. H., J. Am. Chem. Soc. 1982, 104, 305.

[181] Kiji, J., Chem. Int. 1978, 179, 833.

[182] Snow, A. W., Nature, 1981, 40, 292.

[183] Patel, G. A.; Walsh, E. K., J. Polym. Sci. Polym. Lett. Ed. 1979, 17, 203.

[184] Levanon, H.; Galili, T.; Regev, A.; Wiederrecht, G. P.; Svec, W. A.; Wasielewski, M. R., J. Am.Chem. Soc. 1998, 120, 6366.

[185] Angadi, M. A.; Gosztola, D.; Wasielewski, M. R., J. Appl. Phys. 1998, 83, 6187.

[186] Degreczeny, M. P.; Svec, W. A.; Marsh, E. M.; Wasielewski, M. R., J. Am. Chem. Soc. 1996, 118, 8174.

[187] Toshima, N.; Tominaga, T. T.; Kawamura, S. I., Jpn. Bull. Chem. Soc. 1996, 69, 245.

[188] Angadi, M. A.; Gosztola, D.; Wasielewski, M. R., Mater. Sci. Eng. 1999, B63, 191.

[189] Forrest, S. R.; Kaplan, M. L.; Schmidt, P.; Venkatesan, T.; Lovinger, A., Appl. Phys. Lett. 1982, 41, 708.

[190] Swalen, J. D., J. Mol. Electron. 1986, 2, 155.

[191] Tang, C. W., Appl, Phys, Lett. 1986, 48, 183.

[192] Tang, C. W.; Vanslyke, S. A., Appl. Phys, Lett. 1987, 51, 913.

[193] Toda, Y.; Yanagi, H., Appl. Phys. Lett. 1996, 69, 2315.

[194] Ranke, P.; Blevl, I.; Simmerer, J.; Haarer, D.; Bacher, A.; Schmidt, H. W., Appl. Phys. Lett. 1997, 71, 1332.

[195] Kojima, H.; Ozawa, A.; Takahashi, T.; Nagaoka, M.; Homma, T.; Nagatomo, T.; Omoto, O., J. Electrochem. Soc. 1997, 144, 3628.

[196] Rodríguez-Liorente, S.; Aroca, R.; Duff, J., J. Mat. Chem. 1998, 8, 629.

[197] Madec, C.; Courtot-Coupez, J., J. Electroanal. Chem. 1977, 84, 169.

[198] Rodriguez-Mendez, M. L.; Aroca, R.; DeSaja, J., J. Am. Chem. Soc. 1992, 4, 1017.

[199] Urbaniczky, C.; Lundstrom, K., J. Electroanal. Chem. 1984, 176, 169.

[200] Olson, C.; Adams, R. N., Anal. Chem. Acta 1960, 22, 582.

[201] Linquist, J., J. Electroanal. Chem. 1974, 37, 52.

[202] Pungor, E.; Szepesvary, E., Anal. Chim. Acta 1968, 43, 289.

[203] Rice, M. E.; Galus, Z.; Adams, R. N., J. Electroanal. Chem. 1983, 89, 143.

[204] Breant, M. G., J. Chimica Acta 1977, 90, 111.

[205] Rodríguez-Llorente, S.; Aroca, R.; Duff, J., Spectrochim. Acta 1999, A55, 969.

[206] Miller, L.; Gd, N.; Ea, M., J. Org. Chem. 1972, 6, 916.

[207] Cornil, J.; Vanderdonckt, S.; Lazzaroni, R.; dos-Santos D.A.; Thys, G.; Geise, H.J., Chem. Mater. 1999, 11, 2436.

[208] Loutfy, R.O.; Cheng, Y.C., J. Chem. Phys. 1980, 73, 2902.

[209] Slattery, D. K.; Linkous, C. A.; Gruhn, N. E.; Baum, J. C., Dyes & Pigments, 2001, 21, 49.

[210] Bard, A. J.; Faulkner, L. R., Electrochemical Methods: Fundamentals and Applications, John Wiley & Sons. Inc., New York 1980.

[211] Unwin, P. J.; Mulcahy, C. P. A.; Jones, T. S., Surface Science 2001, 1222.

[212] Schreiber, F., Prog. in Surf. Sci. 2000, 65, 151.

[213] Mobus, M.; Kark, N.; Kobayashi, T., J. Cryst. Growth, 1992, 116, 495.

[214] Mullen, K.; Kubel, C.,Website MPI for Polymer for Schung Germany 2003.

[215] Aroca, R.; Rodriguez-Liorente, S., J. Molecular Structure, 1997, 17, 408.

[216] Shklover, V.; Tautz, F. S.; Scholz, R.; Sloboshanin, S.; Sokodowski, M.; Schaefer, J. A.; Umbloch, E., Surf. Sci. 2000, 60, 454.

[217] Schreiber, M.; Vragovic, I.; Scolz, R.; Tautz, F. S.; Eremtchenko, E.; Schaefer, J. A.; Sokolowski, M.; Glockler, K.; Shklouer, V.; Umbach, E., Surf. Sci. 2002, 176, 502.

[218] Taborski, J.; Vaterlein, P.; Dietz, H.; Zimmerman, U.; Umbach, E., J. Electron Spect. 1995, 75, 75.

LIST OF PUBLICATIONS

1998

1. B. Klassen, R. Aroca, **M. Nazri**, G.A. Nazri, Raman Spectroscopy and Transport Properties of Lithium in Ethylene Carbonate Based Binary Solvent Systems for Lithium Batteries; J. Phys. Chem. 1998, 102, 4795-4801.

2. G.A. Nazri, B. Yebka, **M. Nazri**, M.D. Curits, K. Kinoshita, D. Derwin Safety and Reactivity of Carbonaceous Anodes in Lithium Batteries; . . Electrochem. Soc. Meeting. Ext. Abs. 46, Spring, May 3-8, 1998, San Diego Meeting.

3. **M. Nazri**, M.D. Curtis, B, Yebka, G. A. Nazri, C. Julien, Far-IR and X-ray diffraction of layered oxide cathode for lithium batteries; Electrochem. Soc. Meeting. Ext. Abs. 46, Spring May 3-8, 1998, San Diego Meeting.

1999

4. **M. Nazri**, G.A. Nazri, R. Aroca, Spectroscopic and Transport Properties of Lithium Perchlorate in Ethylene Carbonate Based Binary Solvents for Lithium Batteries; Mat. Res. Soc. Symp. Proc. Vol. 548, 1999 Materials Research Society.

5. G.A. Nazri, B. Yebka, **M. Nazri**, D. Curtis, Reactivity of Carbonaceous Anodes Used in Lithium-ion Batteries, Part I: Correlation of Structural Parameters and Reactivity; Materials Research society, Symposium Proceedings, 1999. Vol. 548, P. 27-36, 1999

6. R. Aroca, **M. Nazri**, G.A. Nazri, Raman and Infrared Spectra of Layered Oxide Cathode Materials; (October 17-22,1999) Electrochem.; Soc. Hawaii Meeting.

7. **M. Nazri**, Performance and Optimization of Layered Oxide Cathodes for Application in High-Energy and High-Power Batteries; (October 17-22, 1999) Electrochem. Soc., Hawaii Meeting.

8. E. Clavijo, **M. Nazri**, R. Aroca, J.R. menendez, G.a. Carriedo, F.J. Garcia-Alonso Vibrational Spectra of Cyclic Phosphazenes, , Journal of Raman spectroscopy,1999, 30, 1121-1125.

9. **M. Nazri**, G.A. Nazri, R. Aroca, Spectroscopic and Transport Properties of Lithium Salts in Ethylene Carbonate Based Mixed Solvents For Lithium Batteries, , Mat. Res. Soc. Symp. Proc. Vol. 548,1999, pp.389-393, , Material Research Society.

2000

10. **M. Nazri**, R. Aroca, G.A. Nazri, Structural and spectroscopic investigation of $LiPF_6$ for lithium battery, Submitted to the Journal of Raman Spectroscopy, 2000.

11. **M. Nazri**, R. Aroca, G.A. Nazri, Spectroscopy of Non- aqueous electrolyte for application in advanced lithium batteries;
J. Solution Chemistry, Vol 29, (10), (2000),1063-1076.

12. G.A. Nazri, **M. Nazri**, B. Yebka,Thermal properties of Lithium-Ion Battery Materials. International Union for Pure and Applied Chemistry August 2000, Halifax,Canada.

13. **M. Nazri**, R. Aroca, J.R. menendez, G.a.Carriedo, F.J. Garcia-Alonso, E. Clavijo, Vibrational Spectra and Ion-Pair Properties of Lithium Hexafluorophosphate in Ethylene Carbonate Based Mixed-Solvent Systems for Lithium Batteries; Journal of Solution Chemistry. 2000, Vol. 29, No. 10.

14. R. Aroca, **M. Nazri**, T. Lemma, A. Rougier, G.A. Nazri, Raman Spectra of Anode and Cathode. Materials, Materials for Lithium-Ion Batteries, C.Julien and Z. Stoynov (eds) Kluwer Academic Publishers, Printed in the Netherlands.2000, 327-339.

2002

15. **M. Nazri**, R. Aroca, G.A. Nazri, Solid electrolyte Interface formation on lithium battery electrode; , Electrochemical Society Proceedings Volume, Vol 000, Page 000, 2002 (submitted and accepted).

16. G.A. Nazri, **M. Nazri**, Global Status of Advanced Lithium Batteries: Materials Aspects; 43rd International Battery Meeting, October 10-14, 2002. (Presentation and publication).

IN PREPARATION and to be SUBMITTED

1. Electrochemistry of poly-nuclear aromatic compounds in nonaqueous electrolytes. (submitted).

2. Ion-association in multi-blend electrolyte for lithium batteries. In preparation

3. Preferential solvation of lithium-ion in multi-blend non-aqueous electrolytes. (In preparation)

4. IR spectroscopy of electrolyte decomposition on the surface of lithiated graphite. (In preparation).

5. Vibrational Spectroscopy and X-ray diffraction studies of Calcium Gallium Silicon Melilite. (In preparation).

6. Hydrogen storage in ABH_4 compounds, (A=alkali metal, B= B, Al, and Ga). Submitted for the MRS Fall Meeting, 2003.

VITA AUCTORIS

Maryam Nazri was born in Malayer, Iran. She finished her, Primary School, High School, and Bachelor of Science in Iran before moving to the USA. She received her Master's degree in Chemistry at the Oakland University, Rochester, Michigan, USA, in 1995. Then she worked under supervision of Professor David Curtis at the University of Michigan, Department of Chemistry as a researcher on materials aspects of lithium batteries. She joined Professor Ricardo Aroca's group in the University of Windsor, Department of Chemistry and Biochemistry in 1998. She has been working on materials synthesis, characterization, and evaluation for energy conversion devices. She has also involved in science and technology of fuel cells and solid-sate hydrogen storage materials. She hopes to develop environmental friendly energy storage and generation systems.